7

THE INFLUENCE OF NITROGEN ON THE DEFORMATION BEHAVIOUR OF A MODIFIED AISI TYPE 200 SERIES ALLOY.

BY TARYN BIGGS

A Thesis submitted to the Faculty of Engineering, University of Cape Town in fulfilment of the degree of Master of Science in Applied Science.

Dept of Materials Engineering
UCT
July 1993

ABSTRACT

This thesis investigates the influence of nitrogen concentration on the deformation behaviour of a modified AISI 200 type alloy. The Fe-18Cr-4Ni-7Mn base alloys contained a range of nitrogen contents from 0 to 0.27 wt%. The tensile behaviour was characterised by uniaxial tensile testing. The room temperature yield strength was shown to decrease with increasing nitrogen content for nitrogen contents less than 0.1 wt%. This decrease was attributed to the presence of secondary phases in the annealed state. An increase in yield strength was observed with further additions of nitrogen and this is probably due to solid solution strengthening and a Cottrell interaction. The variation of room temperature ultimate tensile strength showed no dependence on nitrogen content. Elevated temperature tensile tests (120°C) showed an increase in ultimate tensile strength and yield strength with nitrogen content suggesting that solid solution strengthening and a Cottrell interaction are occurring in this alloy range. Room temperature deformation was shown to induce a transformation from austenite to martensite throughout this alloy range, the degree of transformation decreasing with increasing nitrogen content. This transformation was shown to provide considerable strengthening and work hardening to the alloy. The low stacking fault energy (SFE) of this alloy range ensured that cross-slip was significantly inhibited during room temperature deformation and the deformation mode was observed to be planar glide. Nitrogen was shown to increase the SFE of this alloy range thus causing a decrease in the inhibition of cross-slip with increasing nitrogen content. Increasing the nitrogen content thus causes a decrease in strength if the contributions of a deformation-induced transformation, SFE variation and secondary phases are considered but causes an increased strengthening contribution due to solid solution strengthening and a Cottrell interaction. Hence as the nitrogen content increases different strengthening mechanisms are activated and no overall trend of room temperature ultimate tensile strength with nitrogen content is observed. The ductility and formability of the steels did not appear to show any distinct trends with changes in nitrogen content.

ACKNOWLEDGEMENTS

I wish to express my appreciation to all those who assisted me during the course of this project:

My supervisors;
Dr R.D.Knutsen and Prof M.P.Shaw

and ;
Dr D.P.van Heerden
Dr C.I.Lang
Dr M.B.Cortie
Mr C.Fletcher
Mr O.E.Schmidt
Mr J.Robinson
Mr B.Greeves
Mr J.Peterson
Mrs A.C.Ball
Mr C.van der Riet
Mr M.Suckling
Mr V.R.Ming
Mr R.L.Howard
Mrs T.Tintinger
Mr G.Newins
Mrs J.Sharland
Mr N.Dreze
Mr D.Dean
Dr P.Wedepohl

Finally the FRD and Mintek are greatly acknowledged for the provision of financial support.

CONTENTS

Page

CHAPTER 1

INTRODUCTION

1.1 BACKGROUND

Austenitic stainless steels account for about 75% of the total production of stainless steel [1,2]. Metastable austenitic alloys are used in the fabrication of an extensive selection of components for architectural, automotive, industrial and domestic applications. Metastable austenitic stainless steel components are usually drawn from the AISI 300 series steels, which are extensively produced owing to their excellent combination of strength, elongation, toughness and corrosion resistance. These steels, however, usually contain high amounts of nickel (8%). Nickel is a metal with limited and unpredictable availability [3] and the price of nickel has a very significant contribution to the end price of stainless steel. The inability of nickel producers to continue to supply nickel at a sufficiently competitive price could have adverse effects on the growth of the stainless steel industry. Cheaper materials such as plastics and aluminium will become more viable options and tend to replace stainless steels. Much research has been directed towards the need for partial or total replacement of nickel, especially after nickel shortages were experienced in Europe before the Second World War and in America during the Korean War. Nickel is a strong austenite-forming and -stabilising element and it must be replaced by elements of similar potential. Carbon and nitrogen are the most potent austenite-formers and -stabilisers, but, since the additions of carbon can be more detrimental in terms of impaired corrosion resistance and decreased weldability, nitrogen was selected as a potential replacement for nickel. Manganese is often added in conjunction with nitrogen, since, in addition to being an austenite-stabiliser, it also enhances the solubility of nitrogen in the steel. The additions of manganese and nitrogen to partially or completely replace nickel, led to the development of the AISI 200 series steels, which are being produced in the USA and India among others. These steels have found useful application because of their high strengths, work hardening rates, improved wear resistance and low costs. The initial production costs have been reduced and the steels can now be manufactured by the AOD (Argon Oxygen Decarburisation) process. Although there is no single general purpose steel that can function under a wide variety of corrosive conditions, in some corrosive environments, eg. where pitting resistance is required [1,3], they can perform better than an AISI 300 series steel.

Austenite stability is influenced predominantly by temperature and composition. Nitrogen, in particular, is a strong austenite-forming and -stabilising element and additions of nitrogen thus increase the potential to retain the austenite structure. If the nitrogen additions are inadequate, the austenite is insufficiently stabilised and this can promote the formation of δ-ferrite and martensite, the latter upon cooling or deformation. The formation of these secondary phases modifies the overall deformation behaviour of the alloys. Increases in nitrogen content and deformation temperature also influence the solid solution strengthening potential and stacking fault energy (SFE) of the alloy. Alterations in the solid solution strengthening potential and SFE significantly influence the deformation behaviour.

1.2 OBJECTIVE OF THE THESIS

The aim of this research is to investigate the mechanical properties of a modified AISI 200 series composition, as a function of austenite stability. The austenite stability has been altered by changes in nitrogen content (0 to 0.27 wt%) and tensile testing temperature (20°C and 120°C). The tensile properties, hardness and formability of the alloys were assessed. The evolution of microstructure with deformation, was studied in an attempt to correlate these changes to the observed macroscopic properties. The objectives were to observe the effects of nitrogen on the microstructure and to gain an understanding of the role that nitrogen plays in the strengthening processes of this alloy range.

CHAPTER 2

LITERATURE REVIEW

2.1 PHASE EQUILIBRIA IN IRON AND STEEL

Pure iron (Fe) exists in two crystal forms, a body-centred (bcc) α-iron, (ferrite) which remains stable from the low temperature regions up to 910°C, where it transforms to a face-centred cubic (fcc) (γ)-iron (austenite) [4]. The γ-iron is stable until 1390°C, when it reverts to a bcc structure (now δ-ferrite), which remains stable up to the melting point of 1536°C [4]. The stability of the phases can be altered by changes in temperature and the addition of alloying elements [4]. The presence of even a small amount of carbon and nitrogen (eg. 0.1 wt%) can have an appreciable strengthening effect on iron. The additions of up to 2 wt% of carbon to Fe constitute a steel. The atomic sizes of carbon and nitrogen are sufficiently small to enable them to enter the α- and γ-iron as interstitial solute atoms. The various allotropic forms of Fe have different capacities for dissolving carbon and nitrogen [5]. Thus, while γ-iron can contain up to 2 wt% carbon, α-iron can contain a maximum of 0.008 wt% carbon at room temperature [5]. A transformation from austenite (γ-phase,fcc) to ferrite (α-phase,bcc) thus involves the diffusion of interstitial atoms. If cooling is rapid there is insufficient time for diffusion to occur, and the iron atoms are locked into a highly stressed, body centred tetragonal (bct) or bcc crystal structure, namely martensite (Fig 1). The temperature at which martensite starts to form during cooling is defined as the M_S temperature, whereas M_f is the temperature at which the transformation is terminated. In addition to austenite, ferrite and martensite, microstructures such as pearlite and bainite can be obtained at higher carbon contents and after a variety of cooling rates.

Stainless steels are those steels which contain more than 12 wt% Cr and exhibit good corrosion resistance. They can be broadly classified on the basis of crystal structures into ferritic (bcc), martensitic (bct) and austenitic stainless steels [6]. More recent developments include duplex stainless steels (ferritic-austenitic) and precipitation-hardened steels.

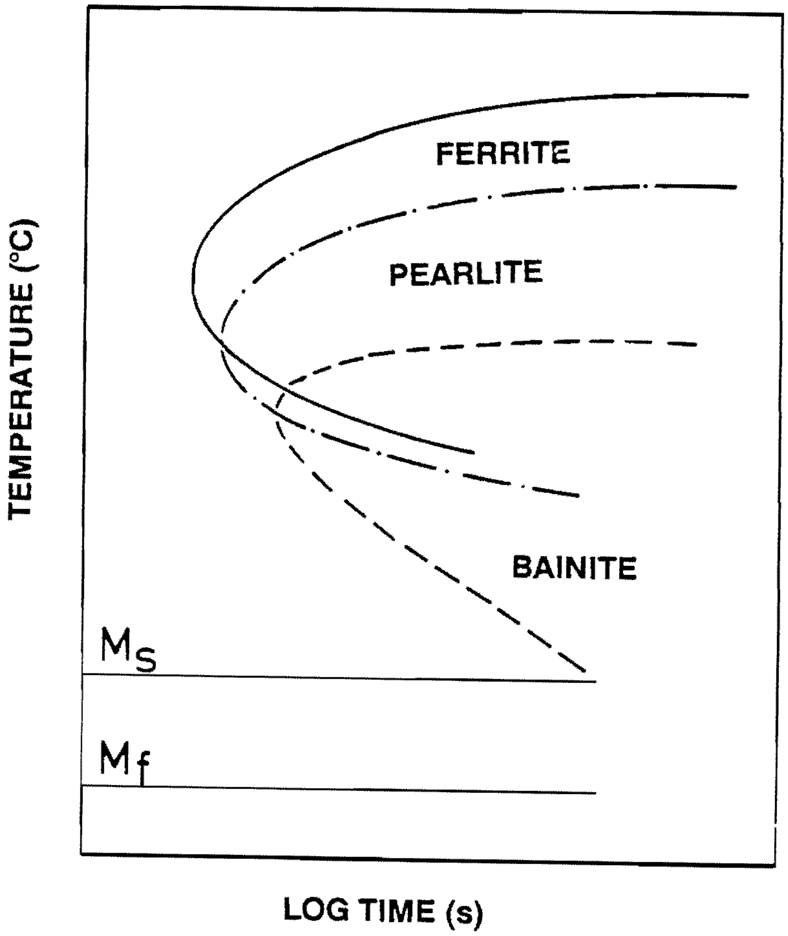

Fig 1: A schematic of a Temperature Time Transformation diagram [After Ref 7]

2.1.1 The Fe-Cr System

Chromium (Cr) and iron are mutually soluble in all proportions at temperatures above 850°C [8]. The α and δ allotropes of iron unite at over 12 weight percent chromium to form a continuous bcc solid solution α–δ-Fe, stable at all temperatures up to the solidus [Fig 2]. This α–δ ferrite phase is retained on cooling to room temperature. For Cr contents less than 12 wt%, a bcc δ-ferrite phase is formed below the liquidus. On cooling, a temperature is reached, depending on Cr content, where a transformation from δ-ferrite (bcc) to austenite (fcc) occurs. On further cooling the austenite phase converts to a α-ferrite (bcc) phase, which is maintained at room temperature.

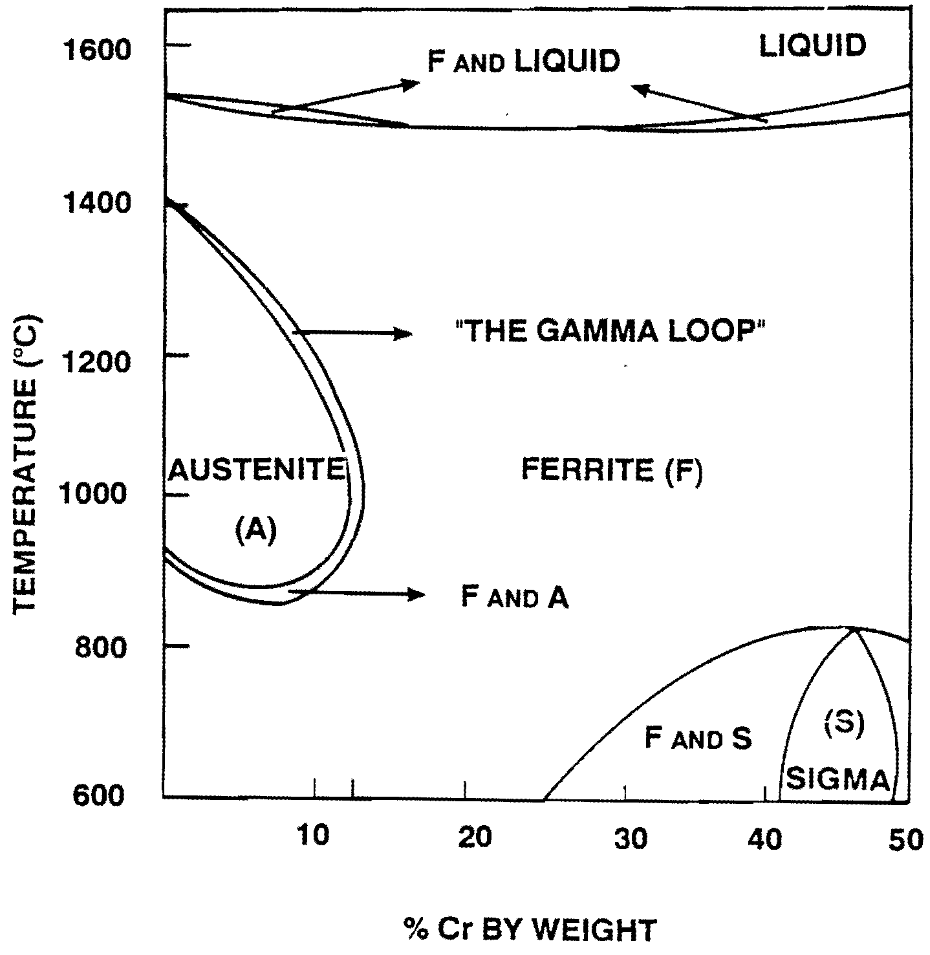

Fig 2: A section of the Iron-Chromium Equilibrium Diagram [After Ref 9]

2.1.2 The Role of Additional Elements in Phase Equilibria

In the Fe-Cr equilibrium diagram shown in Fig 2 the range of the fcc (γ) phase is restricted. This is a consequence of the addition of chromium which enhances the formation of ferrite. Other ferrite-forming elements are titanium, silicon, niobium, molybdenum and aluminium.

Alloying elements which lower the chemical free energy of the austenite phase with respect to the ferrite phase, are known as austenite-forming elements. The addition of austenite forming-elements to the Fe-Cr system results in the austenite field being expanded as shown in Fig 3. Elements such as nickel, carbon, nitrogen and manganese are austenite formers.

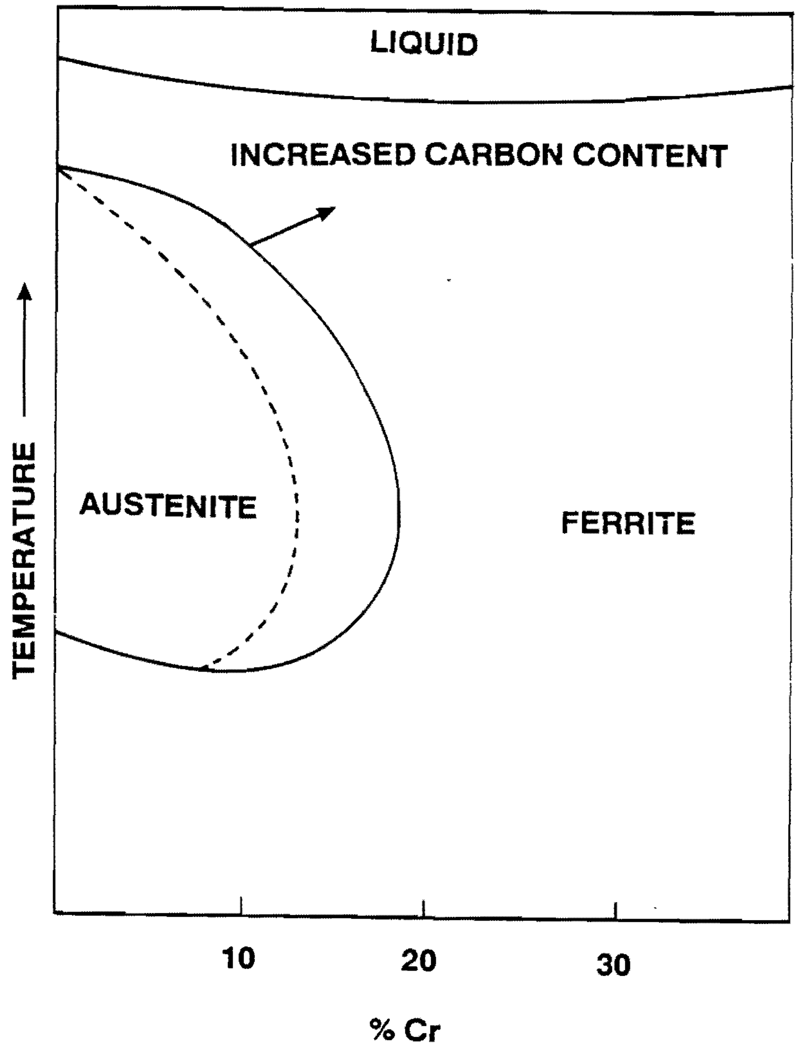

Fig 3: Schematic illustrating the effect of carbon, in enlarging the austenite phase field [After Ref 9]

If the austenite is not sufficiently stabilised, a transformation from austenite to martensite can occur on cooling or deformation. Alloying elements, which promote the retention of the austenite phase on cooling or deformation, are known as austenite-stabilisers. The addition of these elements expands the austenite phase field into the ferritic regions down to lower temperatures.

The effect of adding nickel, which is both an austenite-former and -stabiliser, is shown in Fig 4.

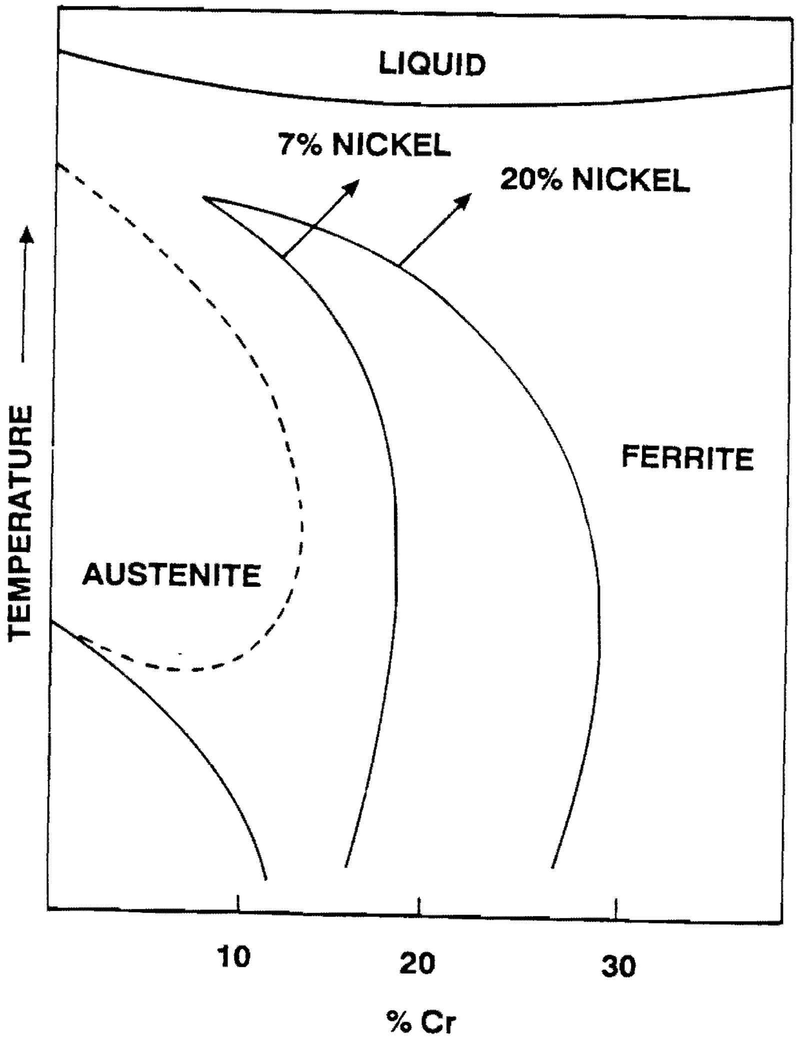

Fig 4: Schematic Diagram illustrating the effect of Nickel in both enlarging and stabilising the austenite phase field down to low temperatures. [After Ref 9]

The relative effects of alloying elements, on the formation of austenite and ferrite respectively, is often expressed in terms of a nickel equivalent and a chromium equivalent. A recent version of these equations is shown below. The coefficients in each case reflect the potency of the element.

Nickel Equivalent = Ni + Co + 0.87 Mn + 30 C + 0.33 Cu + (N - 0.045) x Y

where Y=30 when N= 0 to 0.20 wt%

Y=22 when N= 0.21 to 0.25 wt%

Y=20 when N= 0.26 to 0.35 wt% [After Ref 10] eqn 3.1

Chromium Equivalent = Cr + 2 Si +1.5 Mo + 5 V + 5.5 Al + 1.75 Nb + 1.5 Ti + 0.75 W [After Ref 10] eqn 3.2

A Schaeffler Diagram consisting of a plot of the nickel equivalent versus chromium equivalent is shown in Fig 17, page 43. It represents a prediction of the phases likely to be present at room temperature after rapid cooling from the solution treated condition.

2.1.3 The Martensitic Transformation

a) The Athermal Martensitic Transformation

During rapid cooling a phase transformation from austenite (fcc) to martensite (bct) can transpire. This transformation is a diffusionless shear transformation which is known as a military transformation. An invariant plane strain occurs and the transformation is athermal.

Several orientation relationships exist between the austenite and martensite phases, and the orientation relationship which is observed depends upon the alloy chemistry. For example the Kurdjumov-Sachs (K-S) relationship is the dominant orientation relationship between austenite and α'-martensite in Fe-Cr-C steels but the addition of nickel or manganese changes it to the Nishiyama-Wasserman (N-W) relationship [11].

Some of the orientation relationships predicted by the K-S orientation relationship are:

$(111)_{fcc}//(011)_{bcc}$

$(10\bar{1})_{fcc}//(11\bar{1})_{bcc}$

$(\bar{1}2\bar{1})_{fcc}//(\bar{2}1\bar{1})_{bcc}$ **[After Ref 12]**

Some of the orientation relationships predicted by the N-W orientation relationship are:

$(0\bar{1}1)_{fcc}//(001)_{bcc}$

$(\bar{1}11)_{fcc}//(\bar{1}10)_{bcc}$

$(211)_{fcc}//(110)_{bcc}$ **[After Ref 12]**

The orientation relationship usually observed between austenite and ε-martensite is:

$(1\bar{1}0)_{fcc}//(1\bar{2}10)_{hcp}$ **[After Ref 13]**

$[111]_{fcc}//[0001]_{hcp}$

An understanding of the austenite to martensite transformation can be obtained from the accompanying free energy changes. At temperatures below T_0 (Fig 5), the free energy of martensite is lower than austenite and a transformation from austenite to martensite is energetically favourable.

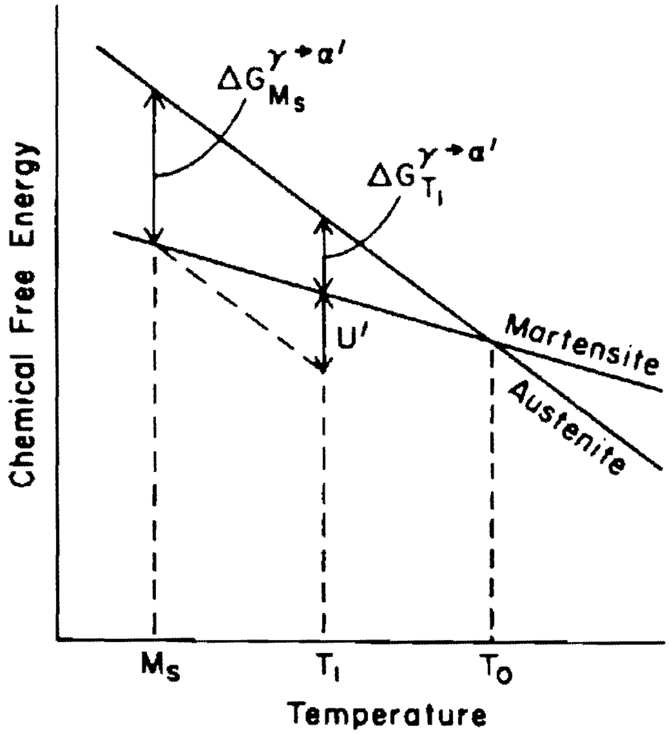

Fig 5: Schematic Diagram showing the Gibbs Free Energy Changes for a Martensite Transformation [After Ref 4]

However, an additional driving force is required for the transformation as phase boundaries and volume changes are produced [4]. This is provided by undercooling so that the transformation proceeds spontaneously at a temperature M_S, less than T_O (Fig 5). The driving force (the free energy difference between austenite and martensite) at M_S is sufficient to overcome the activation barrier. Empirical M_S temperatures based on composition have been formulated for a variety of steels and are shown below. Equation 2.4 was derived for austenitic steels, equation 2.5 for austenitic stainless steels and equation 2.6 for a Fe-Cr-Mn alloy containing 8-12 wt% Cr, 0-10 wt% Mn and 0-0.60 wt% N. These equations illustrate how the austenite stability is radically altered by changes in chemical composition.

$$M_S\ (^\circ C) = 1305 - 1667\,(C + N) - 27.8\,Si - 33.3\,Mn - 41.7\,Cr - 61.1\,Ni$$ **[After Ref 14]**

eqn 2.4

M_s (°C) = 502 - 810 C - 1230 N -13 Mn -12 Cr - 30 Ni - 6 Mo -54 Cu [After Ref 15]
eqn 2.5

M_s (°C) = 555 - 450 N -40 Mn - 9 (Cr - 8) [After Ref 16]
eqn 2.6

The Empirical M_s values differ widely and are only applicable for the composition ranges from which they were derived.

b) The Deformation-induced Martensitic Transformation

If room temperature lies between T_0 and M_s, eg. at T_1 in Fig 5, plastic deformation of austenite may induce a transformation from austenite to martensite and the austenite is termed metastable. At T_1, the free energy difference is insufficient to overcome the activation energy barrier for spontaneous martensite formation, but the additional energy required for the transformation may be supplied in the form of mechanical energy (U') (Fig 5). There exists a temperature M_d between T_0 and M_s, below which the transformation to martensite can occur as a consequence of plastic deformation [17]. Above this temperature, the chemical driving force is too small and nucleation of martensite cannot be mechanically induced [4]. The M_d temperature is difficult to determine experimentally and a M_{d30} temperature has therefore been defined as the temperature at which 50 vol% martensite is formed after 30% true strain [18]. Some empirical M_{d30} temperatures are shown below.

M_{d30} (°C) = 413 - 462 (C + N) -9.2 Si - 8.1 Mn -13.7 Cr - 9.5 Ni -18.5 Mo
[After Ref 8] eqn 2.7

M_{d30} (°C) = 497 - 462 (C + N) -9.2 Si - 8.1 Mn -13.7 Cr - 20 Ni -18.5 Mo
[After Ref 19] eqn 2.8

In order to understand the influence of applied stress on the formation of martensite in a metastable austenitic steel, the relationships shown in Fig 6 need to be considered. The critical stress for martensite formation increases linearly between the M_S and M_S^{σ} temperatures [4,20]. When the austenite is deformed below M_S^{σ} stress-assisted martensite forms before yielding occurs. Deformation above M_S^{σ} produces strain-induced martensite. At T_2, the austenite deforms plastically at a stress σ_a, and is strain-hardened up to a stress σ_b. At this stress the austenite starts undergoing a transformation to martensite. This stress (σ_b) is considerably lower than the stress (σ_c) deduced on the basis of free energy differences. Wayman [4] cites Ondura et al [21] as suggesting that the reason for this is because the stress is locally concentrated at obstacles and thus is equivalent to σ_c. Another idea proposed [4] is that it is a consequence of defects and the intersections of microscopic shear bands providing nucleation sites [22].

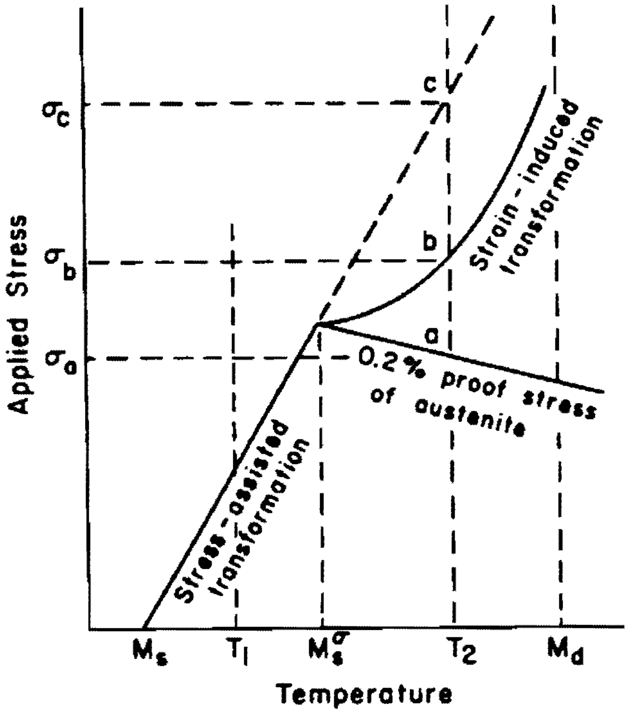

Fig 6: Schematic Diagram showing the critical stress needed to initiate the formation of martensite as a function of stress [After Ref 4]

During deformation, the martensite that forms can be α-martensite, ϵ-martensite or a mixture of the two. ϵ-martensite is a hexagonal close packed (hcp) phase which forms predominantly in materials with a low stacking fault energy (SFE) [23,24,25]. Dash and

Otte [26] believe that ϵ-martensite only forms because of the large shape deformation required during the transformation of austenite to α-martensite.

c) The nucleation of martensite in steels

Olson and Cohen [27] have proposed a martensite nucleation mechanism which takes the transformation kinetics into account. It considers the nucleation process as a sequence of steps which takes the particle from maximum to minimum coherency and leads to the hypothesis that the first step in the martensite transformation is faulting on the close packed planes. It was successfully shown that a hcp crystal, consistent with the known orientation relationships can be created from a fcc lattice merely by the passage of a Schockley partial dislocation on every second close packed plane. It was subsequently shown [28] that a transformation from a fcc to bcc structure can be achieved by an analogous process which is illustrated in Fig 7. Fig 7a, represents an $\mathbf{a_{fcc}/2\ [1\bar{1}0]}$ screw dislocation lying normal to the plane of the diagram. By dissociating on the (111) plane and spreading over three planes, this dissociation can produce three $\mathbf{a_{fcc}/18\ [1\bar{2}1]}$ and three $\mathbf{a_{fcc}/18\ [2\bar{1}\bar{1}]}$ partial dislocations as shown in Fig 7b. Thicker faults can be produced by the simultaneous dissociation of an $\mathbf{a_{fcc}/2\ [1\bar{1}0]}$ dislocation every three planes. From this structure atoms can readily move to bcc positions by a modified shear mechanism on $(11\bar{1})_{fcc}$ planes (which are equivalent to the $(011)_{bcc}$ planes), and will produce an interfacial structure (Fig 7c) consisting of seven $\mathbf{a_{bcc}/8\ [01\bar{1}]}$ partial dislocations followed every eighth plane by a $\mathbf{a_{bcc}/8\ [0\bar{1}1]}$ partial dislocation and a $\mathbf{a_{fcc}/6\ [112]}$ Schockley partial. These dislocations lines will lie along $[110]_{fcc}$. In this way, a semicoherent bcc martensitic embryo is produced in the Kurdjumov-Sachs orientation. The stacking fault energy will decrease with increasing fault thickness. The fault structure depicted in Fig 7c is close to bcc, but still represents a highly coherent form. The additional displacements, which maintain an unrotated fault plane by cancelling the edge components of the $\mathbf{a_{bcc}/8\ [01\bar{1}]}$ dislocation displacement, allow a partial relaxation toward the equilibrium bcc structure, but the remaining portion of the screw component will still have a long range strain field which is not accommodated by the matrix. The long range strain field can be cancelled by the formation of an additional array of lattice screw dislocations oppositely directed to the screw component of the $\mathbf{a_{bcc}/8\ [01\bar{1}]}$ displacements.

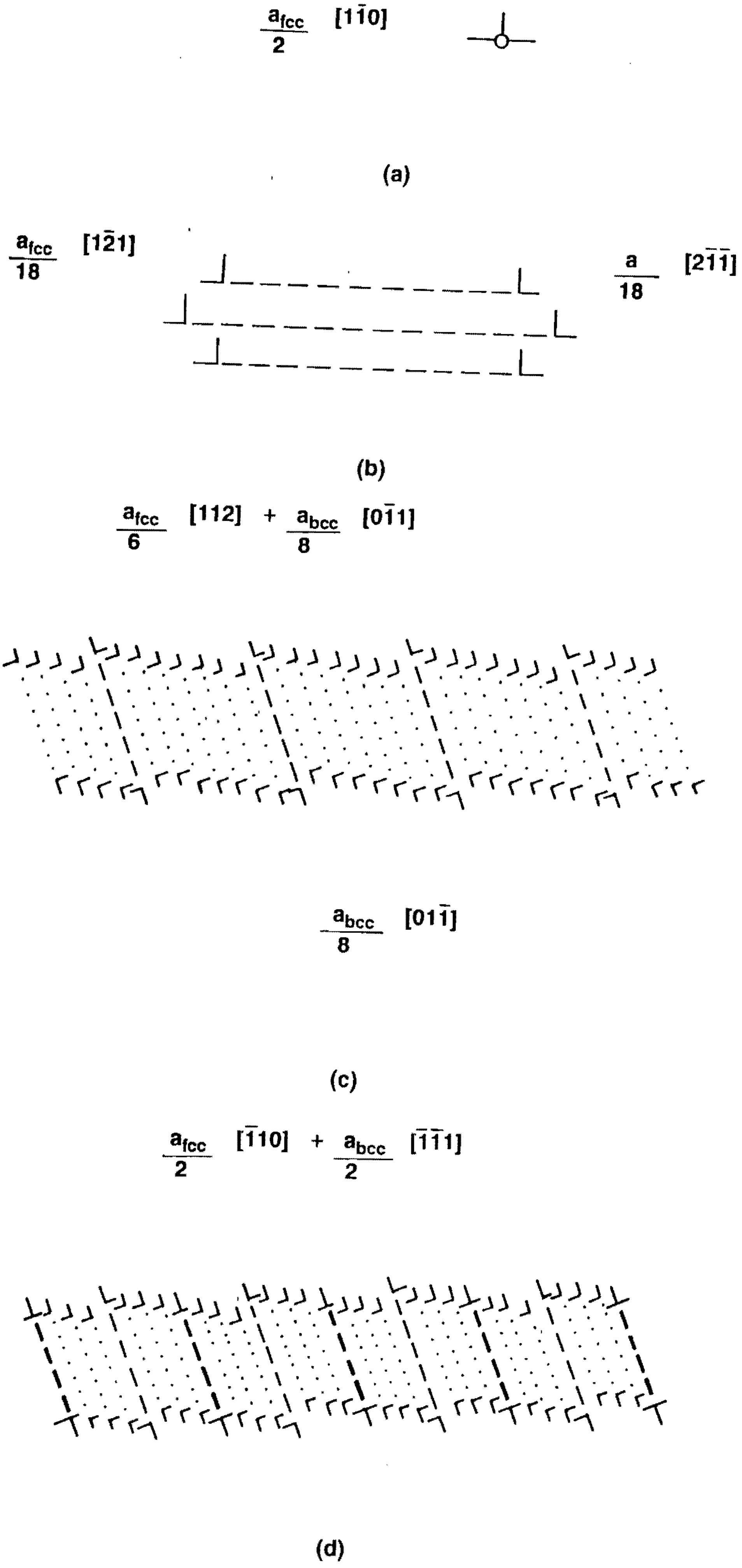

Fig 7: The formation of a bcc region from the passage of partial dislocations in a fcc matrix [After Ref 28]

These dislocations will have a Burgers vector of $\mathbf{a_{bcc}/2\ [\bar{1}\bar{1}1]}$ and spaced every eighth $(011)_{bcc}$ plane. Fig 7d, in which the Kurdjumov-Sachs orientation is still maintained but the coherency strain energy is substantially reduced, is obtained by superimposing such an interfacial dislocation array on that of Fig 7c. Stacking fault energy thus has an appreciable contribution to the nucleation process.

Crystal defects which contain the required dislocation arrays for martensite nucleation are grain boundaries, incoherent twin boundaries [29] and inclusion particle surfaces. Microscopic shear bands are also considered to be effective sites. Operative shear bands are ε-martensite [30,32], deformation twins and stacking fault bundles [31].

ε-Martensite has been shown to form directly from the austenite phase and to be an intermediate transformation product in the transformation of austenite to α'-martensite [32]. The austenite to α'-martensite transformation can however proceed without the formation of ε-martensite [33]. In systems in which both martensites are observed, as the strain increases, there is a rapid transformation from austenite (γ) to ε-martensite while the amount of α'-martensite grows gradually, as is shown in Fig 8. At larger strains, in region III, α'-martensite is formed with greater intensity, the amount of ε-martensite present reaches a peak, while the intensity of the austenite transformation diminishes. At extreme strains, in region IV, the austenite volume fraction is unchanged while the α'-martensite grows at the expense of the ε-martensite.

The transformation is autocatalytic and at sufficiently large strains α'-martensite appears to grow into polyhedral shapes [31]. Dislocation cells, grain boundaries and mechanical twins could inhibit the growth of martensite. As the amount of deformation increases, the density of substructures increases and the growth of martensite becomes hindered [34]; and the amount of martensite approaches saturation [13].

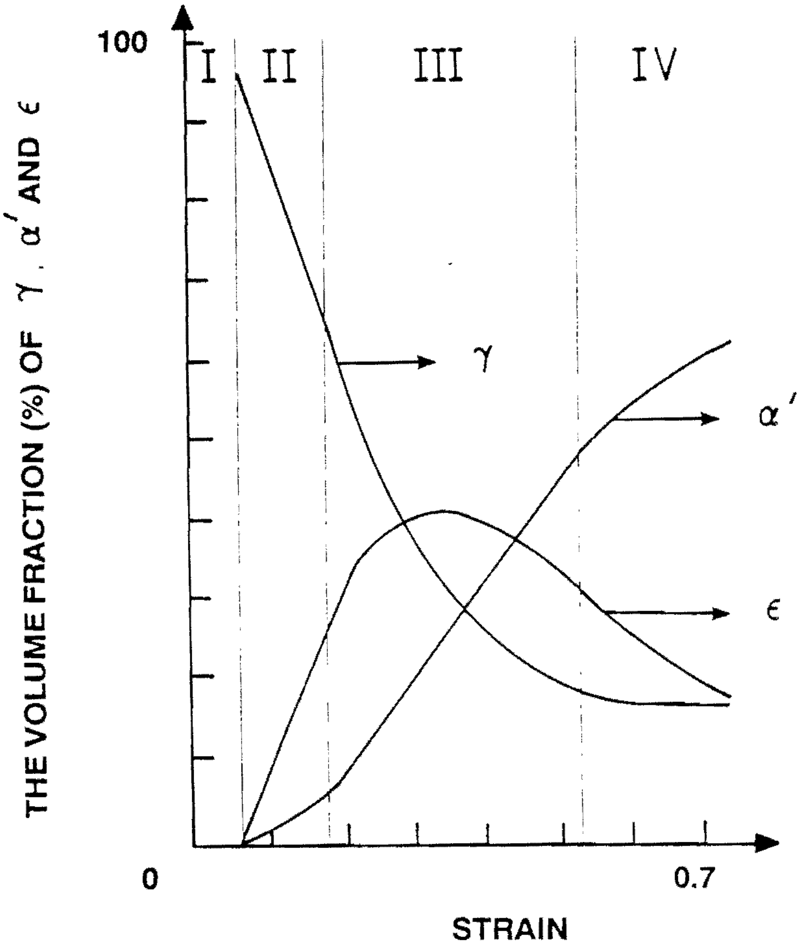

Fig 8: The amount of martensite as a function of strain [After Ref 30]

2.2 STRENGTHENING MECHANISMS OPERATING IN AUSTENITIC STAINLESS STEELS

To gain an appreciation of the strength of various austenitic stainless steels, the strengthening mechanisms operating, and their effect on other properties, such as ductility, must be considered.

2.2.1 Dislocations

The flow stress increases as the dislocation density increases and the work hardening of the steel is dependent upon the way in which dislocations are distributed and interact with one another [19]. Any resistance to dislocation motion, during plastic deformation, will produce strengthening. It is generally accepted that work-hardening effects result from the tangled forest of dislocations that form as a result of deformation [5]. This tangled structure makes further plastic deformation more difficult and higher stresses need to be applied.

2.2.1 Solid Solution Strengthening

It appears that the biggest contribution to the flow stress of solid solutions arises not from the locking of dislocations but from their resistance to movement, ie. a frictional force, the magnitude of which is sensitive both to atomic size differences and differences in elastic properties between solute and solvent [7]. Elements can go into solid solutions substitutionally or interstitially. Interstitial solid solutions, such as carbon and nitrogen, have far greater strengthening effects than substitutional solid solutions, such as manganese and nickel [24]. This increased strengthening is further augmented by the very strong interaction that occurs between interstitials and dislocations, which is known as the Cottrell interaction. Increases in yield strength [35] and UTS [36] occur as the solute concentration increases.

2.2.2 Stacking Fault Energy (SFE)

SFE has an important contribution to the strengthening of alloys. A low SFE invokes the ready dissociation of dislocations into pairs of partial dislocations, which cannot undergo cross-slip. The inhibition of cross-slip results in high strengths and work hardening. A low SFE also promotes the nucleation of martensite from austenite. SFE promotes an increase in UTS but does not contribute significantly to the yield strength and proof stress.

2.2.3 Grain Size Hardening

A major disadvantage of austenitic steels, is their low potential to undergo grain size hardening [7]. Grain size can however have a contribution to strength, even though it may be tenuous. A smaller grain size causes an increased yield strength. The relationship between yield strength and grain size can be represented by a Hall-Petch equation. The potential for grain size refining is increased with increasing nitrogen content [37]. The effect of grain size on yield strength can be explained by assuming that a dislocation source operates within a crystal causing dislocations to move and eventually pile-up at a grain boundary. The pile-up of dislocations generates a stress in an adjacent grain, which eventually operates a new dislocation source, hence propagating the yielding process from grain to grain [7]. If the deformation mode consists of a planar array of dislocations, the yield strength will be dependent on grain size, however as the dislocation array becomes more cellular, and the slip distance becomes shorter than the grain diameter, the yield stress is less likely to be influenced by grain size [37]. The UTS does not show much grain size dependence, as stacking fault energy (SFE) contributions to strengthening overshadow this effect.

2.2.4 The Presence of Second Phases Prior to Straining

In austenitic stainless steel both martensite and δ-ferrite can be present prior to straining. Increasing the δ-ferrite content causes strengthening by fibre strengthening, partitioning of interstitials from the ferrite to austenite phase and the generation of dislocations in the austenite phase near the ferrite interface [36]. A further effect of raising the δ-ferrite content is to invoke grain refinement of the austenite, providing additional strengthening [24]. The strengthening by δ-ferrite is reported to be more pronounced on the proof stress and yield strength than UTS [36]. The presence of martensite prior to straining elicits an increase in strength due to composite hardening. However Irvine et al [36] report that the presence of up to 35 vol% martensite prior to straining did not produce any significant effect on proof stress and there is evidence that the proof stress tended to decrease with increasing martensite content up to 20 vol%. The UTS increases with prior martensite content but a decrease in ductility is observed [24,36].

2.2.5 Deformation-Induced Martensite

Martensite that forms during plastic deformation produces increased strengthening due to composite hardening [38]. If during straining, martensite forms in regions of incipient necking, necking can be prevented and enhanced elongation is observed [39]. This enhanced elongation is known as Transformation Induced Plasticity (TRIP). This results in elevated strength and high ductility and is in contrast to the other strengthening mechanisms where increased strength precipitates a decrease in ductility [40]. Investigators [41] have shown that it is not the amount of martensite forming that is critical but the strain at which it forms. The transformation should be gradual and selective to obtain an optimum contribution to strength and ductility [42]. If the transformation proceeds too slowly, necking is not sufficiently suppressed [43], however, if the transformation rate is too high, deformation of a brittle martensite phase essentially occurs [23]. The formation of ϵ-martensite during straining can increase the strain hardening rate and UTS [34]. Substantial formation of ϵ-martensite however will initiate a brittle fracture. The kinetics of the formation of ϵ-martensite are not suitable for the TRIP phenomenon as the maximum rate of transformation occurs at strains which are too low [34].

In the absence of the formation of strain-induced martensite the work hardening rate (WHR) continuously decreases with increasing strain Fig 9. For metastable austenitic stainless steels, where deformation induces a transformation to martensite, the WHR initially decreases as deformation of the austenite occurs and this is illustrated in Fig 9. At low strains the WHR subsequently reaches a minimum, lower than the WHR experienced by a more stable steel, increasing to a maximum at intermediate strains [17,38]. The minimum in WHR is associated with the formation of martensite [17,44] and it has been shown that martensite starts to form just prior to the minimum in WHR [17]. This minimum in WHR is attributed to a dynamic "transformation softening" which is due to the operation of the transformation plasticity as a deformation mechanism [45,46,47,63]. The minimum is observed because the volume fraction of a martensite crystal is larger than an austenite crystal and the shape change contributes to the overall strain, increasing the strain at a lower stress level. At strains beyond those which produce a minimum in WHR, the transformation rate and correspondingly, the volume fraction of martensite, increase, producing a rise in strength by virtue of composite strengthening or "static hardening" [46]. A continual refinement of the martensite and austenite mixture occurs and the stronger martensite phase produces a hardening effect

[17]. This results in a rise in WHR with increasing strain. Thus the formation of martensite causes both dynamic "transformation softening" and "static hardening", the softening dominating at low strains and the hardening at high strains.

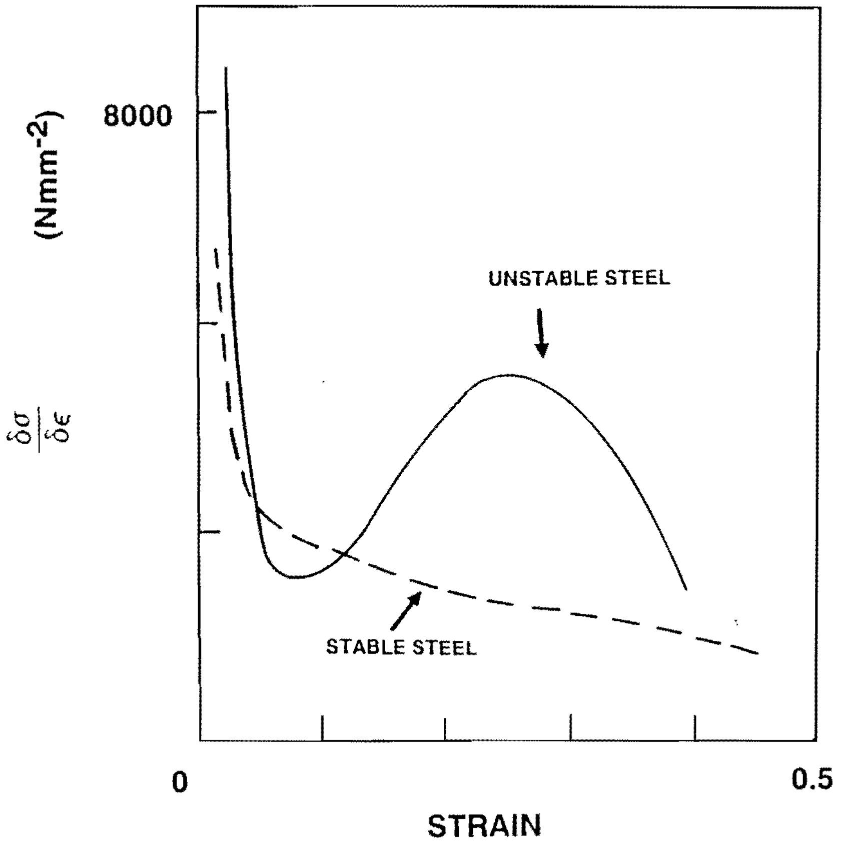

Fig 9: The Work Hardening Rate (WHR) Behaviour of a Stable and Unstable Steel [17]

The hardening effect is observed in the stress / strain curves of metastable austenitic stainless steels which exhibit upward curvatures when a transformation is induced [46]. As the volume fraction of martensite reaches a saturation, deformation of a predominantly martensite matrix results in a decrease in WHR with increasing strain.

The stress state and crystallographic orientation have direct influences on the kinetics of the strain-induced transformation [48,49,50,51]. Less martensite forms in compression than tension [50,51], whereas biaxial tension is more effective than uniaxial tension at producing martensite [31,52].

2.3 DEFORMATION BEHAVIOUR AS A FUNCTION OF AUSTENITE STABILITY

It has already been stated that the most important factors affecting austenite stability are chemical composition and temperature. A variation in nitrogen content and deformation temperature will thus modify the austenite stability across an alloy range. Austenite of a given composition can also be stabilised by thermomechanical treatments since large amounts of deformation, above M_d, inhibit the nucleation and growth of martensite at less stable temperatures.

2.3.1 The Effect of increasing the austenite stability on the strengthening mechanisms

The austenite stability within this study has been enhanced by increasing both the nitrogen content and deformation temperature. The effect of increasing nitrogen content and deformation temperature, both result in a suppression of the deformation induced transformation of austenite to martensite. There exists an optimum austenite stability to obtain the best combination of strength and ductility from the strain-induced transformation to martensite. If the austenite stability is too low the transformation rate is too high whereas if the austenite stability is too high, necking is not sufficiently suppressed during deformation. Thus at constant deformation temperature there exists an optimum nitrogen content for the best combination of strength and ductility, and at constant nitrogen content there exists an optimum deformation temperature. As temperature is altered, the SFE changes [27] and this effect is illustrated in Fig 10. For temperatures greater than 150 K, an increase in SFE is observed with increasing temperature. Fujikura et al [53] established that stacking fault probabilities vary as a function of nitrogen content. Since SFE is the inverse of stacking fault probability, it is inferred that SFE will increase with nitrogen content in regions of low austenite stability, and decrease with increasing nitrogen content in regions of high austenite stability. This variation of SFE with nitrogen content is shown in Fig 11. Some workers [54,55] have nonetheless reported that nitrogen does not change SFE, while others [56,57] have reported that nitrogen causes a decrease in SFE. The decrease in SFE was observed for high nitrogen contents and although Fawley et al [54] observed no change in SFE they did observe a change in planar to cellular dislocation structure with nitrogen content. The many diverse opinions on the effect of nitrogen content on SFE are a consequence of the variation in austenite stability with composition.

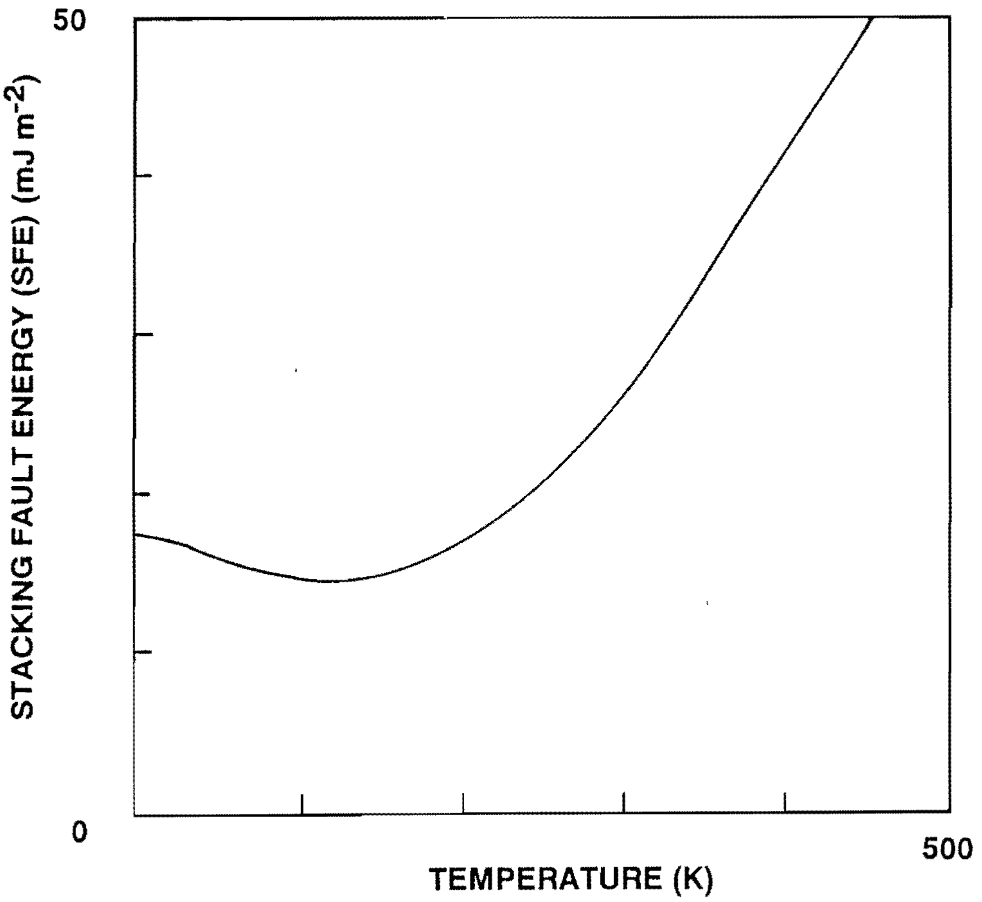

Fig 10: The Variation of SFE with Temperature [After Ref 27]

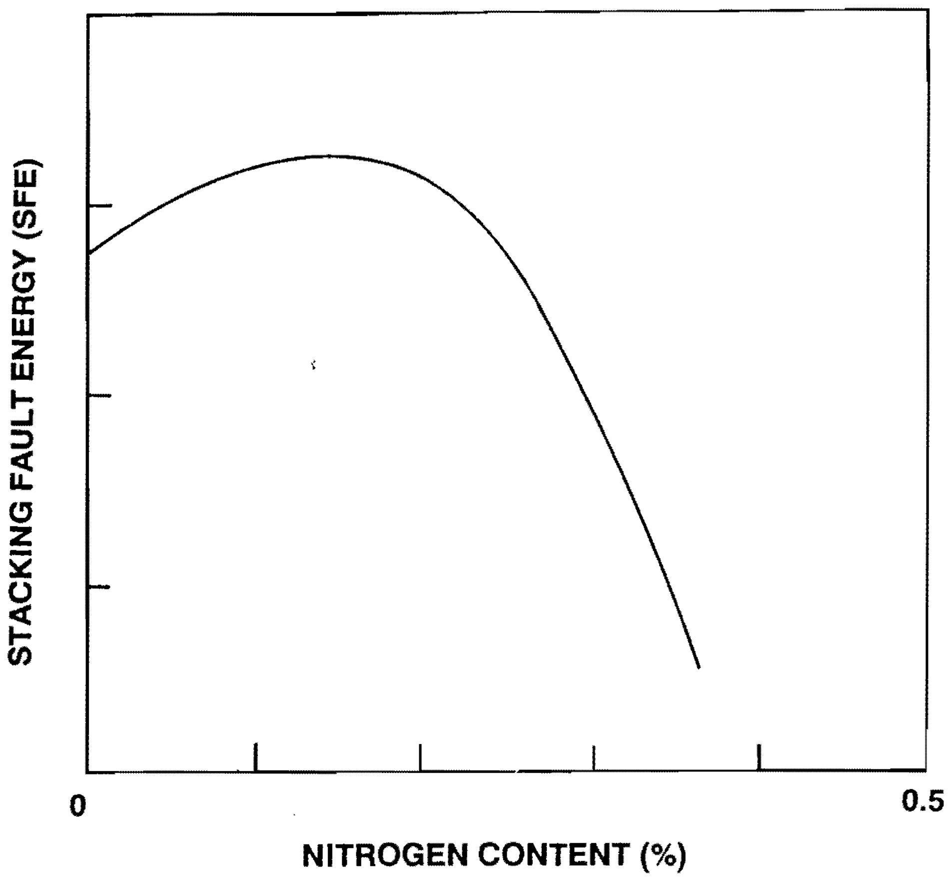

Fig 11: The Variation of SFE with Nitrogen Content [After Ref 53]

Increasing the nitrogen content and temperature not only raises the austenite stability, but can affect the other strengthening mechanisms in a completely distinct manner. The degree of solid solution strengthening is proportional to the square root of the solute concentration and this relationship is schematically illustrated in Fig 12. As the temperature is raised, the effects of solid solution strengthening diminish and this is illustrated in Fig 13. At higher temperatures, lower strengths are anticipated as there is a increase in thermally activated flow and an increase in thermal vibrations.

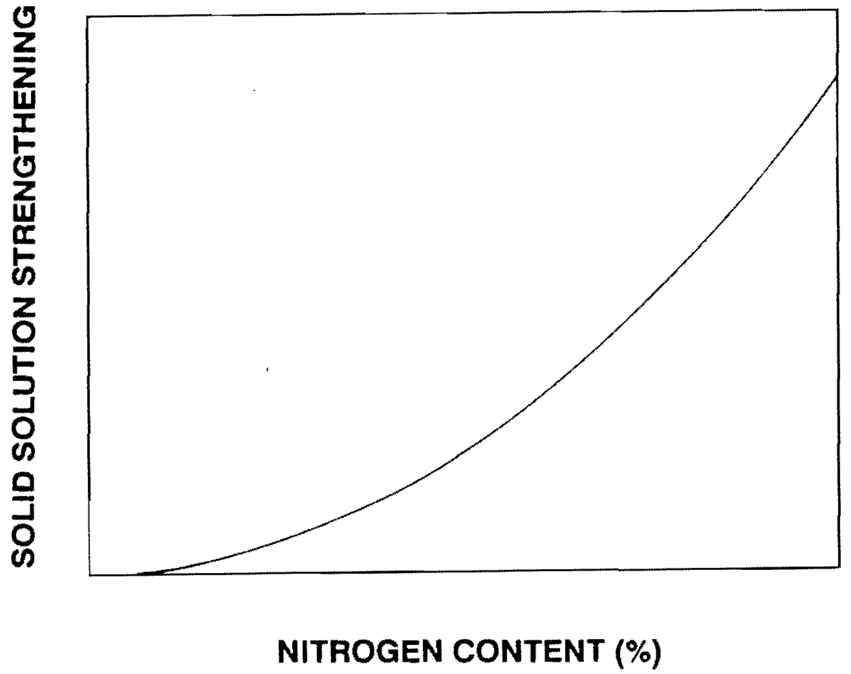

Fig 12: Schematic Diagram illustrating the Variation of Solid Solution Strengthening with Nitrogen Content [After Ref 37]

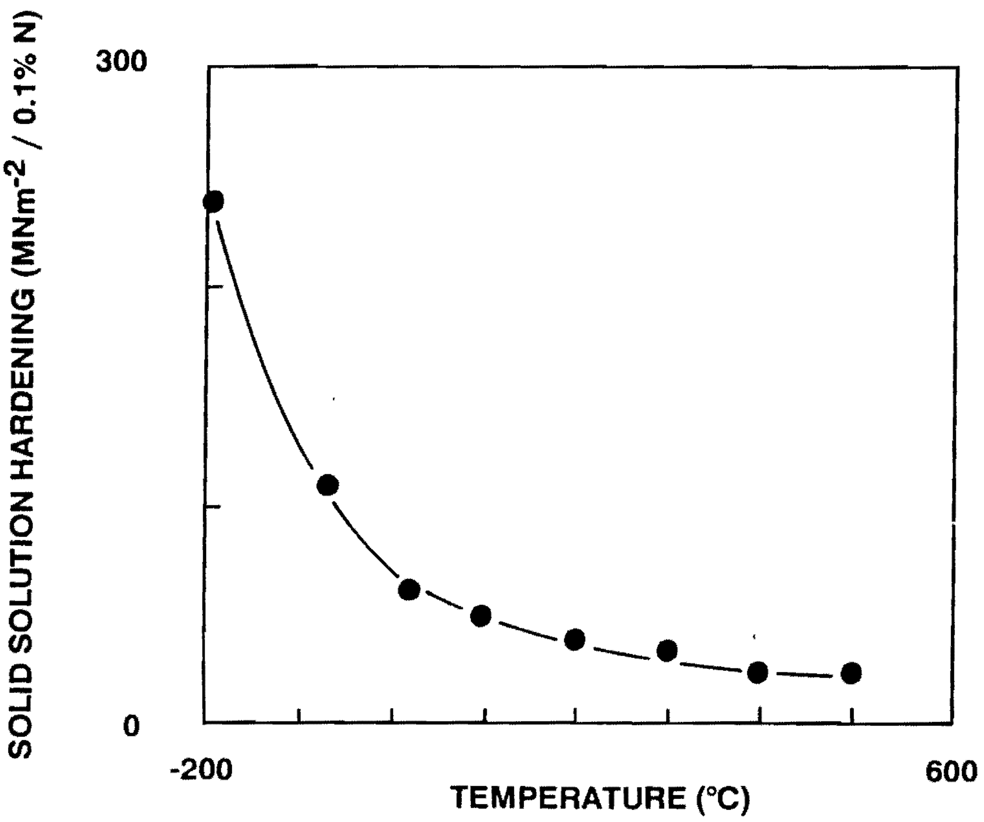

Fig 13: The Variation of Solid Solution Strengthening with Temperature [After Ref 37]

The likelihood of the existence of second phases (martensite and ferrite) in the undeformed state, and the corresponding strengthening contribution diminishes with increasing nitrogen content. Increasing the nitrogen content, by virtue of the fact that it decreases the probability of δ-ferrite being present, results in an increase in grain size. Nitrogen has no pronounced effect on grain size in the absence of δ-ferrite. As the temperature increases, the contribution of grain size hardening is diminished.

2.3.2 The Effect of the Austenite Stability on UTS, Yield Strength and Ductility

It has been widely reported that increasing nitrogen content (and thus austenite stability) increases the UTS and yield strength [35,36,53,58,59,60]. These increases in UTS are generally for a stable austenitic stainless steel and due to contributions from solid solution strengthening and stacking fault energy (SFE) changes. In stable austenitic stainless steels the strengthening contribution from SFE, increases with increasing nitrogen content. In a metastable austenitic stainless steel Ludwigson et al [61] report that the reduction in propensity to transform as the composition is enriched by carbon, overshadows any strengthening of martensite that could accrue from the enrichment. Despite this, at low carbon values they observed that solid solution strengthening outweighs the stabilising effect with the result that increases in carbon causes increases in UTS. At high carbon values the stabilising effect predominates and a decrease in UTS is observed with increasing carbon. The variation of nitrogen in a metastable stainless steel, would be expected have an analogous effect, the strength decreasing as the nitrogen content increases, since the same strengthening mechanisms are operating, namely a decrease in the propensity to undergo a deformation-induced martensitic transformation, as the nitrogen content increases. The strengthening contribution from SFE also diminishes with increasing nitrogen content, at very low austenite stability ie. low nitrogen contents in a metastable austenitic stainless steel [53]. At very low nitrogen contents there is a possibility that, like carbon [61], nitrogen may cause solid solution strengthening of the martensite phase. As the addition of nitrogen stabilises the austenite phase, there exists a nitrogen content, above which the steel is stable and an increase in strength should be observed with further increases in nitrogen content. It is not expected that the deformation-induced transformation would be initiated at the low strains at which the yield strength are measured, and thus an increase in yield strength with nitrogen content is still expected, even in regions of low austenite stability, as solid solution strengthening should play a major strengthening role during plastic deformation. Fujikura et al [53] report that the austenite stability and SFE affect the strength more predominantly than the extent of martensite and solid solution contributions.

As the temperature increases the UTS and yield strength are observed to decrease [45,62,63,64]. Sakuma et al [43] however observed for Si-Mn (1.2-1.6 wt%) steels and Ni (4 wt%) steels, that yield strength, increased or remained constant with increasing temperature although UTS decreased. They explain the variation of yield strength with temperature, as a consequence of the increases in strain contributed by the expansion associated with martensite formation, which is promoted at lower temperatures.

In the absence of a deformation induced transformation, increases in strength imply that a decrease in ductility should be observed. The effect of temperature and nitrogen content on ductility, in unstable austenitic alloys is analogous as they exert the same effects on austenite stability. A peak in ductility is observed as the austenite stability is altered. The peak in elongation is usually observed between M_s and M_d [64]. Chanani et al [63] and Rosen et al [42] report a sharp drop above the M_d where the austenite is stable and the elongation approaches that of the cold worked austenite. Below the peak, a more moderate decline in elongation is observed where deformation of martensite is occurring.

2.4 THE EVOLUTION OF MICROSTRUCTURE WITH DEFORMATION AS A CONSEQUENCE OF AUSTENITE STABILITY

Deformation of austenitic stainless steels can occur by six modes; dislocation motion in the austenite (slip); dislocation tangles, cell formation and the formation of stacking faults; deformation twinning in the austenite; martensite formation; dislocation motion in the martensite; and deformation twinning in the martensite [65]. As the strain increases the deformation mode progresses in the above order. The morphology of the martensite that forms in metastable stainless steels is composition dependent, and can be either plate martensite which usually contains a high density of transformation twins or lath martensite which usually contains a high density of dislocations [66]. Deformation-induced martensite may have the same morphology as thermally-induced martensite depending upon the steel composition [23,29,31,45,67].

In a stable steel, it has been observed [68] that increasing the austenite stability, by virtue of raising the nitrogen content, generates a decrease in SFE and increase in internal friction. Plastic deformation was observed to consist of a combination of planar glide at low strains and predominantly deformation twinning at high strains. Secondary twinning was observed at very high strains. As the nitrogen content (and hence austenite stability) increased, the planarity of glide became sharper, the structures became finer and the onset of twinning as a deformation mode, shifted to lower strains and greater stresses. These changes lead to additional hardening effects since more dislocations have to be activated, more dislocation barriers are formed; and the efficiency of barriers is enhanced. It has been proposed that the increase in planarity as nitrogen content is raised, could be attributed to a form of short-range ordering as nitrogen has a strong affinity for chromium [69]. Observations in a metastable steel [25] revealed however that as the nitrogen content (austenite stability) increased, a decrease in planarity was observed as the microstructures evolved from a planar to cell structure. This is in contrast to the changes occurring in a stable steel as a function of austenite stability, but can be readily explained when the variation of SFE with austenite stability is considered. In stable steels, SFE decreases with increasing nitrogen content (austenite stability) whereas in unstable steels SFE increases with increasing nitrogen content (austenite stability). As the SFE increases a change from planar arrays to cellular structures is usually observed, ie. planarity decreases. It has been reported by Singh [70] that alloying elements which reduce the SFE, favour the nucleation of twins at lower stresses. Thus depending on the degree of austenite stability experienced, changes in microstructure with increasing austenite stability can be different.

2.5 THE EFFECT OF AUSTENITE STABILITY ON HARDNESS

Hardness measurements indicate work hardening phenomena [13]. A relationship between hardness and UTS usually exists, though Krivobok et al [71] report that for alloys of high chromium content the relationship is not apparent. They state however that hardness and UTS become interrelated after heavy reduction by cold work. Singh [70] reports that stable and unstable austenitic stainless steels show similar hardness values although the hardening products are different. The unstable steel achieves the hardening through martensite and deformation bands whereas the stable steel achieves hardening only by deformation or twin bands. The variation of hardness with deformation has been shown to be independent of the deformation mode (compression or tension) although more martensite forms under tension [51]. The high work hardening in the Hadfield steel has been attributed to extensive deformation twinning [46]. It has however been reported by Leslie et al [72,73], that there is little correlation between work hardening ability and twinning frequency in a high manganese, austenitic stainless steel. Leslie et al [72,73] suggest that hardening, in this high manganese, austenitic stainless steel, is caused by pinning of dislocations by C-Mn couples. Thus, work hardening is not primarily related to the formation of martensite or deformation twinning but a combination of mechanisms [74]. As the austenite stability is altered the changes in hardness appear to be subtle as different strengthening mechanisms operate.

2.6 THE EFFECT OF AUSTENITE STABILITY ON FORMABILITY

Many applications of austenitic stainless steels involve cold working by both deep drawing and stretch forming [24]. The strain-induced transformation of austenite to martensite is reported to manifest itself in an unusual work hardening behaviour which can provide improved combinations of strength and ductility. Metastable austenitic stainless steels exhibit better stretch forming capabilities than stable austenitic alloys, in operations which involve a substantial stretching component [75]. The formability changes with temperature and at a constant temperature an optimum austenite stability exists to obtain the best formability. The deformation-induced transformation of austenite to martensite is reported to be detrimental to deep drawing operations [24]. In the AISI 200 series stainless steels, the additions of high amounts of nitrogen, markedly increases the flow stress and work-hardening rate, resulting in less general formablility than the AISI 300 series austenitic stainless steels [24].

CHAPTER 3

EXPERIMENTAL TECHNIQUES

3.1 EXPERIMENTAL MATERIALS

Seven novel stainless steel compositions based on the AISI 200 series steels (Fe-17-Cr-7Mn-4Ni), were prepared by Mintek.* Six of these consist of a range of nitrogen content from 0 to 0.27% weight percent (wt%), while the seventh contained 0.1 wt% nitrogen and a higher carbon content than the others. The castings were rolled to a thickness of 1mm, annealed at 1050 °C for 45 minutes and finally quenched in water. The exact chemical composition and alloy designations are given in Table 1.

ALLOY	%Cr	%Mn	%Ni	%Mo	%Cu	%C	%N
VF 689	17.0	7.08	4.21	0.04	0.51	0.036	0.000
VF 690	17.1	7.24	4.06	0.04	0.51	0.035	0.047
VF 688	17.5	7.20	4.20	0.04	0.52	0.035	0.100
VF 703	17.5	7.12	4.12	0.01	0.53	0.033	0.130
VF 692	17.3	7.28	4.02	0.04	0.50	0.038	0.190
VF 693	17.5	7.05	4.10	0.05	0.51	0.034	0.270
VF 679	17.8	6.87	4.32	0.05	0.59	0.080	0.100

Table 1: Chemical composition of experimental alloys (wt%)

3.2 METALLOGRAPHY

The microstructures of the various materials were characterised using both light and transmission electron microscopy.

3.2.1 Light Microscopy

Light microscopy was conducted in both conventional bright field mode and by employing Nomarski interference contrast. The specimens were prepared using either an oxalic acid solution (10 V for one minute) or a solution of chromic acid, acetic acid

---

* Council for Mineral Technology, Randburg, South Africa

and distilled water, the conditions of which are described in greater detail in section 3.4.2.

3.2.2 Transmission Electron Microscopy (TEM)

a) Specimen Preparation

Samples of approximately 1mm initial thickness were chemically thinned in a solution of nitric acid (160 ml), acetic acid (200 ml), hydrochloric acid (40 ml) and phosphoric acid (40 ml) at 70 to 80°C to a thickness of less than 500μm. The time required varied from 30 minutes to five hours. Discs of 3mm diameter were punched out of the thinned material, and were subsequently jet polished in a Struers Tenupol to perforation at -10°C, 57V and a moderate flow rate, in a solution of methanol containing 5% perchloric acid and 20% glycerol. The specimens containing martensite were more difficult to prepare, usually chemically thinning faster but producing a poorer surface finish. A comparison of the thin regions of spark-eroded and punched specimens revealed that punching did not induce any additional martensite.

b) Techniques

Transmission electron microscopy was conducted utilising a JEOL 200CX microscope which was operated at an accelerating voltage of 200KV. A double tilt specimen holder was used to obtain a variety of imaging conditions. Bright field and dark field imaging techniques were employed in an assessment of stacking faults, twins, dislocations and secondary phases. Stacking faults and dislocations were imaged just off the two-beam diffraction condition, whereas twins and phase boundaries were usually imaged on zone axes to enable positive identification of the observed morphology. Orientation relationships between the different phases within a stainless steel, as well as the positions of additional reflections in the selected area zone axis diffraction patterns due to twins, have been extensively published [76,77].

c) Stacking Fault Energy (SFE) Measurements

Stacking fault energy (SFE) can be quantitatively assessed by the measurement of extended dislocation nodes (using TEM) or analysing X-ray diffraction profiles using Fourier analysis [57]. The resolution of the electron microscope can restrict the former method and one has to make assumptions for the elastic stiffness coefficients and unit cell dimensions in the latter method, as very little data exists in the literature. There is an inverse relationship between stacking fault probability and stacking fault energy, thus observations of a high stacking fault probability suggest a low stacking fault energy. In this investigation, assessing the relationship between nitrogen content and SFE was of more significance than the actual SFE values. Hence, a qualitative assessment of the variation in SFE as a function of nitrogen content was determined by observing the change in stacking fault densities with nitrogen content. Stacking fault width is inversely related to SFE [78] and the variation of stacking fault widths with nitrogen content was investigated.

d) Problems experienced during TEM analysis

As a result of the use of very thin specimens in electron microscopy, reciprocal lattice points are elongated in the direction normal to the specimen surface [79] and low index zones which are several degrees apart may be visible simultaneously in diffraction patterns. Sandvik et al [80] suggest that there is an inaccuracy associated with the measurement of orientation relationships using orientations other than $[111]_{fcc}//[011]_{bcc}$. Although efforts were made to examine as many zone axes as possible, unfortunately it was often physically impossible to tilt into all the desired zones on a particular selected area. The possibility that the observed orientation relationships may arise from low angle zones appearing parallel cannot be ignored, especially in the cases of the $[\bar{1}01]_{fcc}$ // $[\bar{1}\bar{1}1]_{bcc}$ (Kurdjumov-Sachs) and $[\bar{1}10]_{fcc}$ // $[\bar{1}00]_{bcc}$ (Nishiyama-Wasserman) relationships, which are frequently observed in steels. The low nitrogen specimens which had been highly deformed were strongly magnetic due to the presence of martensite. This presented difficulties in the alignment of the microscope as well as in tilting and it was sometimes impossible to perform controlled tilts.

3.3 TENSILE TESTS

Tensile tests were performed, both at room temperature and at 120°C. Room temperature tests to fracture were repeated at least three times to ensure a reasonable level of reproducibility. The high temperature tests to fracture were in some cases performed only once due to limited specimen availability. In addition, individual specimens from each alloy composition were strained to a maximum level of 0.07, 0.20 and 0.30 true strain respectively, followed by immediate unloading. These specimens were used to study the evolved microstructures at the various strain levels.

3.3.1 Test Apparatus

Tensile tests were performed on a computer-interfaced Zwick 1484 universal testing machine. Specimens were subjected to an initial strain rate of 0.0012 s^{-1} (test speed of 3.6 mm min^{-1}) with a pre-load of 50 N. Tensile tests at room temperature were performed in air and the extension was measured with an extensometer. The high temperature (120°C) testing apparatus, shown in Fig 14, consisted of an oil bath (1), which was heated by a helical coil (2). The temperature was regulated by an Eurotherm temperature controller to within 2°C. The temperature controller was connected to a chromel-alumel thermocouple (3); the tip of which was positioned in close proximity to the specimen gauge length. The extension at 120°C was measured using the cross-head, because the constraints of the high temperature apparatus prohibited the use of the extensometer.

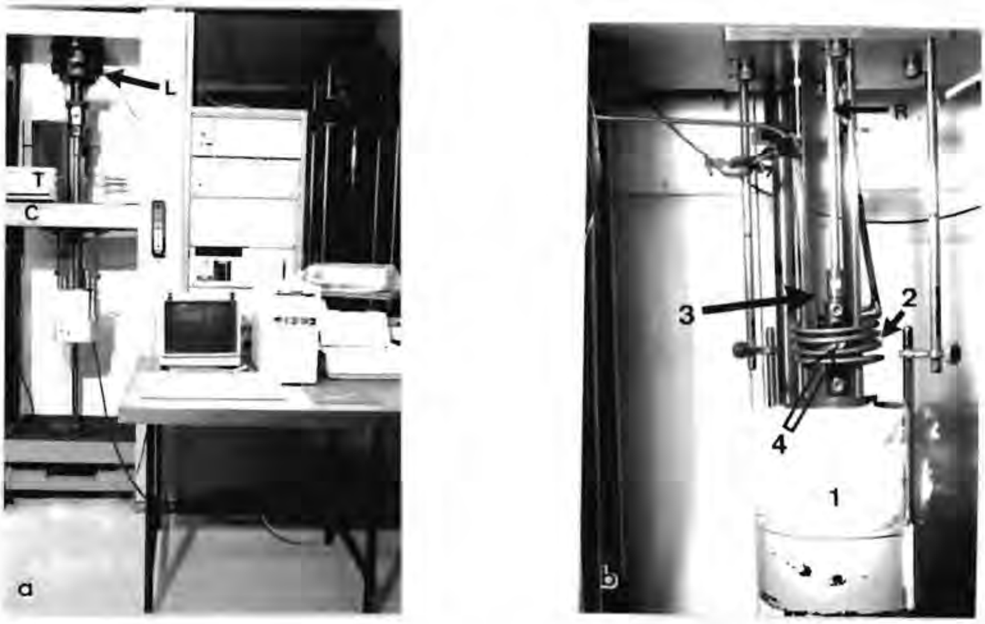

Fig 14 (a) Computer-interfaced Zwick 1484 materials tester, with test rig mounted beneath the cross-head (C), showing the 200kN load cell (L) and temperature controller (T).

(b) Test-rig showing the temperature bath (1) (lowered), heating coil (2), thermocouple (3) and specimen (4).

3.3.2 Specimen Geometry

Room temperature test specimens were punched from 1mm thick sheet with dimensions according to the ASTM E8M standard for rectangular tension test specimens (Fig 15).

deformation was concentrated within the gauge length.

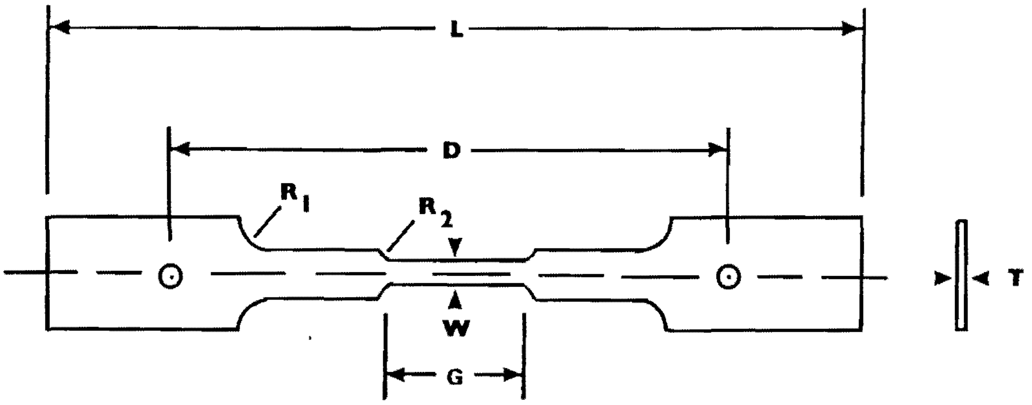

G-	Gauge Length	25.00 mm
W-	Width	5 mm
T-	Thickness	1.00 mm
R1-	Radius of fillet	12.5 mm
R2-	Radius of fillet	6 mm
L-	Overall Length	150 mm
D-	Length of reduced section	100 mm
H-	Diameter of hole	5 mm

Fig 16: Specimen geometry for high temperature tensile testing (based on the ASTM E8M standard for pin-loaded specimens)

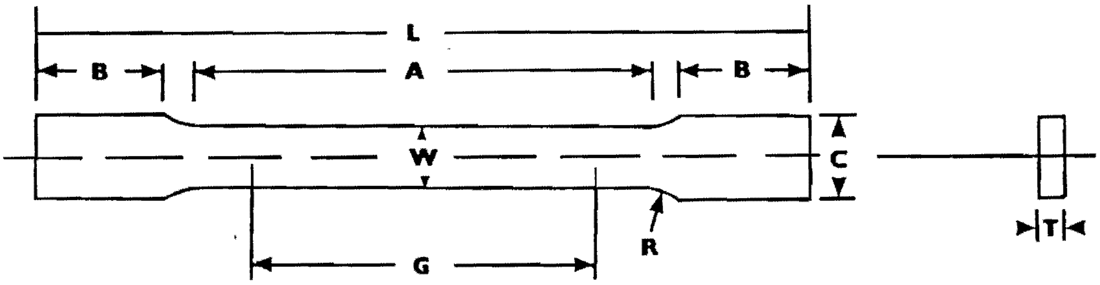

G-	Gauge Length	50.00 mm
W-	Width	12.50 mm
T-	Thickness	1.00 mm
R-	Radius of fillet	12.5 mm
L-	Overall Length	200 mm
A-	Length of reduced section	57 mm
B-	Length of grip section	58 mm
C-	Width of grip section	20 mm

Fig 15: ASTM E8M standard for rectangular tensile specimens used for room temperature tensile tests.

The high temperature tensile testing apparatus prohibited the use of the wedge grips; instead a self-aligning clamping type grip was used in the oil bath. This precipitated an alternative specimen geometry as holes were required at the two ends of the specimen for gripping. Existing flat specimens (Fig 15) were modified to the dimensions shown in Fig 16, which are based on similar ratios to the ASTM E8M standard for pin-loaded tensile test specimens. This specimen geometry was found to be successful and

3.3.3 Data Analysis

The true stress-true strain curve was derived, with the aid of a computer spreadsheet package, by using the equations:

$$\varepsilon_t = \ln (1+\varepsilon_n) \qquad \sigma_t = \sigma_n (1+\varepsilon_n) \qquad \text{eqn (3.1)}$$

In equation 3.1 σ_n and ε_n are the engineering stress and strain respectively and σ_t and ε_t are the true stress and true strain respectively. The work-hardening rate curve was obtained by plotting the slope of the true stress-true strain curve against true strain. The slope of the true stress-true strain curve was obtained from a linear regression analysis over various strain intervals. An error of less than one in a thousand was achieved in the regression.

3.4 X-RAY DIFFRACTION (XRD)

Martensite plates occurring in sheaves or elongated clusters of laths are too small to be resolved individually, using light microscopy. As a consequence of the morphology of martensite, light microscopy indicates greater amounts of strain-induced martensite than actually exist [81]. X-ray diffraction is potentially the most accurate method for quantitative detection of martensite.

3.4.1 Instrument settings

Data was collected using a computer-interfaced Phillips XRD machine. A Molybdenum (Mo) tube was selected in preference for a Copper (Cu) tube as it has a greater depth of penetration. Divergence and scatter slits of 1mm width were inserted. A β-filter (zirconium filter) was inserted between the tube and the specimen to ensure that only Kα radiation bombarded the specimen. The filter was found to be vital in reducing backscatter. A graphite monochromator was used in conjunction with the β-filter, since, the filter alone does not adequately separate the Kα doublet. A voltage of 44kV and current of 34 mA were the settings for the present set-up. An investigation into the count time and degree interval found a 10s count time and 0.1° interval to be adequate. Samples were scanned over a range of 2θ from 18° to 48°. A calibration specimen was irradiated after every tube change and the calculated volume fraction of martensite was found to be accurate to within ±0.1 vol%.

3.4.2 Specimen Preparation

Specimens were cut from the rolled and annealed 1mm sheet to obtain undeformed specimens. Deformed specimens were sliced from tensile specimens which had been strained to 0.07, 0.20 and 0.30 true strain. Due to the non-homogeneous distribution of plastic strain and the variation in temperature along the gauge length [82,83], the volume fraction of martensite is different near the end of the gauge length, compared to the centre of the specimen. For this reason specimens were always cut from the centre of the gauge length. The specimens were 20 mm wide and 10 mm long, as it was found that a specimen area of less than 10 x 10 mm resulted in a reduced peak to background ratio during XRD. Cut specimens were mounted in a transoptic powder mould of approximately 5mm wide to eliminate the usage of a specimen holder during XRD. An XRD trace of the transoptic powder mould was run to observe the contribution, if any, of exposed plastic. XRD traces showed no interference from the plastic mould.

Mounted specimens were mechanically polished to a 3μm finish. Mechanical polishing of the alloy surfaces can induce metastable austenite to transform to martensite, however the deformed layer can be removed by means of an electrochemical polishing process. The mechanically polished specimens were subsequently chemically polished in a solution of chromic acid (100g), glacial acetic acid (532 ml) and distilled water (28 ml) at 20 V for 10 minutes, in an ice-bath of temperature 10-15°C. XRD analysis revealed that this treatment removed the surface martensite. This chromic acid solution was gently stirred to eliminate local heating and bubbles forming at the specimen surface thus improving the quality of the polish.

3.4.3 Calculation of volume fraction of martensite

The X-ray intensity diffracted from each crystal phase is proportional to the volume fraction of that phase present. Austenite (fcc), α'-martensite (bcc), ε-martensite (hcp) and δ-ferrite (bcc) are likely crystal phases to be encountered in stainless steel studies.

X-ray diffraction results in a trace of reflected intensity against 2θ (where θ is the Bragg angle). The Bragg angle is related to the interplanar spacing by Bragg's Law:

$$\mathbf{n\lambda = 2d \sin \theta} \qquad \textbf{eqn 3.2}$$

where
$n = 1,2,3....$
λ = X-ray wavelength
d = the interplanar spacing
θ = the angle between the atomic plane and X-ray beam

The integrated intensity of a particular (hkl) reflection of a phase can be expressed as:

$$\mathbf{I_{hkl} = [I_o.e^4.m^{-2}.c^{-4}].[\lambda^3.A.(32.\pi.r)^{-1}].[v^{-2}].[FF.p.LP].[e^{-2M}.(2.\mu)].V} \qquad \textbf{eqn 3.3}$$

[After Refs 85,89]

where
I_o = intensity of the incident beam
e,m = charge and mass of an electron respectively
r = diffractometer radius
c = velocity of light
A = cross-sectional area of incident beam
v = unit cell volume of particular phase
FF = the product of the structure factor and its complex conjugate
p = multiplicity factor of the (hkl) reflection
LP = Lorentz Polarisation factor
e^{-2M} = Debye-Waller or temperature factor
μ= linear absorption coefficient
λ = X-ray wavelength
V = volume fraction of a particular phase

This equation can be simplified as follows:

$$\mathbf{I_{hkl} = K.R_{hkl}.V].[(2.\mu)^{-1}]} \qquad \textbf{eqn 3.4}$$

where $K= [I_O.e^4.m^{-2}.c^{-4}].[\lambda^3.A.(32.\pi.r)^{-1}]$

$R_{hkl}= V^{-2}.[FF.p.LP].[e^{-2M}].$

K is independent of the nature of the specimen, while R_{hkl} depends on the specimen crystal structure, the reflecting set of planes and θ. Table contains Bragg angles and corresponding R values for various phases present in steels.

The ratio of the volume fraction of austenite (V_γ) to martensite ($V_{\alpha'}$) can now be written as:

$$\mathbf{V_\gamma/V_{\alpha'} = I_\gamma^{hkl}.(R_\gamma^{hkl})^{-1}.(I_{\alpha'}^{hkl})^{-1}.R_{\alpha'}^{hkl} = S} \qquad \textbf{eqn 3.5}$$

Provided that no third phases exist then:

$$\mathbf{V_\gamma = S.[1+S]^{-1}} \qquad \textbf{eqn 3.6}$$

$$\mathbf{V_{\alpha'} = [1+S]^{-1}} \qquad \textbf{eqn 3.7}$$

Diffraction line broadening usually occurs and the intensity of an x-ray at a particular Bragg angle follows a Gaussian distribution. The volume fraction of a phase is consequently proportional to the peak area; as opposed to the peak height. Peak areas were calculated to give the integrated intensity (I) for each reflection. I for each (hkl) line was substituted into equation 3.6, to obtain the volume fraction of austenite present.

Reflections	*Bragg Angle (θ)*	*R_{hkl}*
200 γ (fcc)	*11.39*	*481*
220 γ (fcc)	*16.32*	*298*
311 γ (fcc)	*19.21*	*314*
200 α' (bct)	*14.35*	*224*
211 α' (bct)	*17.73*	*413*
310 α' (bct)	*22.98*	*132*
$10\bar{1}1$ ε (hcp)	*10.65*	
$10\bar{1}2$ ε (hcp)	*13.65*	

Table 2: Bragg angles and R factors for various phases using MoKα radiation.

When two or more phases comprising of the same crystal structure (such as δ-ferrite and α'-martensite) existed simultaneously, then the volume fraction of the most distinguishable phase (δ-ferrite) was estimated optically (point counting), and subtracted from the total volume fraction of that crystal structure which was measured via XRD, to obtain volume fractions for both phases.

3.4.4 Texture Effects

Equation 3.3 is strictly true only for a specimen of infinite thickness and containing a completely random arrangement of crystals [84,85]. When a high degree of preferred orientation is present, integrated intensities should be measured for as large a number of (hkl) lines as possible [85], to eliminate errors. Dickson [85] advocated the use of more than four reflections per phase to eliminate the effects of preferred orientation for heavily cold rolled metastable stainless steel. Livitsanos et al [81] concluded that the use of the three lowest-order reflections of each phase led to a consistent determination of the amount of austenite and strain-induced martensite and was sufficient to include the significant components of texture. Difficulty was experienced in resolving the peak overlap between the 310 α' and 400 γ reflections and so only the 200 α' and 211 α' peaks were used for the contribution of the α'-martensite phase while the 200 γ, 220 γ and 311 γ peaks were used for the austenite phase contribution. The use of more than these five peaks was not found to increase the accuracy of the phase distribution significantly. The spectrum obtained when the specimen was placed orthogonal to its previous position resulted in different austenite peak heights. Using only one peak from each phase would lead to considerable error due to this texture effect. However when the above mentioned three austenite and two martensite peaks were used in the volume fraction analysis, the increase in one peak of a phase is compensated by a corresponding decrease in another peak of the same phase, and the volume fraction of the phase remained constant.

3.5 MICROHARDNESS AND HARDNESS MEASUREMENTS

Bulk hardness measurements were made using a Vickers diamond pyramid indentor with a load of 20kgf on chemically polished surfaces. Each value is quoted for at least five indentations.

Microhardness measurements were performed on a SHIMADZU microhardness tester. A Vickers diamond pyramid was used with a load of 1kgf, for a period of five seconds, and each value quoted is an average of a minimum of fifteen indentations.

3.6 THE EFFECT OF COLD WORKING ON MICROHARDNESS

The alloys containing 0.04 wt% carbon were cold rolled to obtain varying degrees of cold work between 0 and 60%. Cold rolling was performed on a DINKEL laboratory rolling apparatus. The small load capacity of the apparatus limited the specimen size which could be rolled, hence specimens of 40mm length and 14 mm wide were machined from 1mm thick sheet. These specimens were subsequently chemically thinned (as in TEM preparation) to remove the surface scale. Reductions of approximately 0.2mm were obtained for each roll separation setting. Two passes were made per roll gap setting, thereby ensuring that a constant rate of cold work was experienced.

3.7 FORMABILITY

Erichsen tests were conducted to gauge an estimate of the formability of the alloys as a function of nitrogen content. The depth of indentation was measured and the tests were conducted according to the British Standard (B.S. 3855 1965). Polyethylene (gladwrap) was used as a lubricant and a 10kN clamp was applied.

CHAPTER 4

RESULTS

4.1 MICROSTRUCTURAL CHARACTERISATION

4.1.1 Consideration of Schaeffler Diagram

The Nickel and Chromium Equivalents for this alloy range have been calculated using equations (1,2), page 42 and are shown in Table 3. A Nickel Equivalent versus Chromium Equivalent graph illustrates the relationship between austenite and ferrite forming elements [86]. This graph (Fig 17), which is known as a Schaeffler diagram, illustrates the expected phase fields at room temperature for each alloy, after rapid cooling from the solution treated condition.

ALLOY	VF 689	VF 690	VF 688	VF 703	VF 692	VF 693	VF 679
wt% NITROGEN	0.000	0.047	0.100	0.130	0.190	0.270	0.100
Ni Equivalent	10.27	11.64	13.34	14.16	16.01	15.92	14.54
Cr Equivalent	17.04	17.14	17.54	17.51	17.34	17.55	17.85

Table 3: Computated Nickel and Chromium Equivalents of the alloy range

Fig 17 suggests that the alloys containing at least 0.1 wt% nitrogen should have a fully austenitic microstructure after quenching to room temperature. It is anticipated from a consideration of the Schaeffler Diagram (Fig 17) that the 0.047 wt% nitrogen steel will be predominantly austenitic, with the possibility of traces of martensite being present. The 0 wt% nitrogen steel should consist predominantly of an austenitic matrix, with some δ-ferrite and martensite present as well.

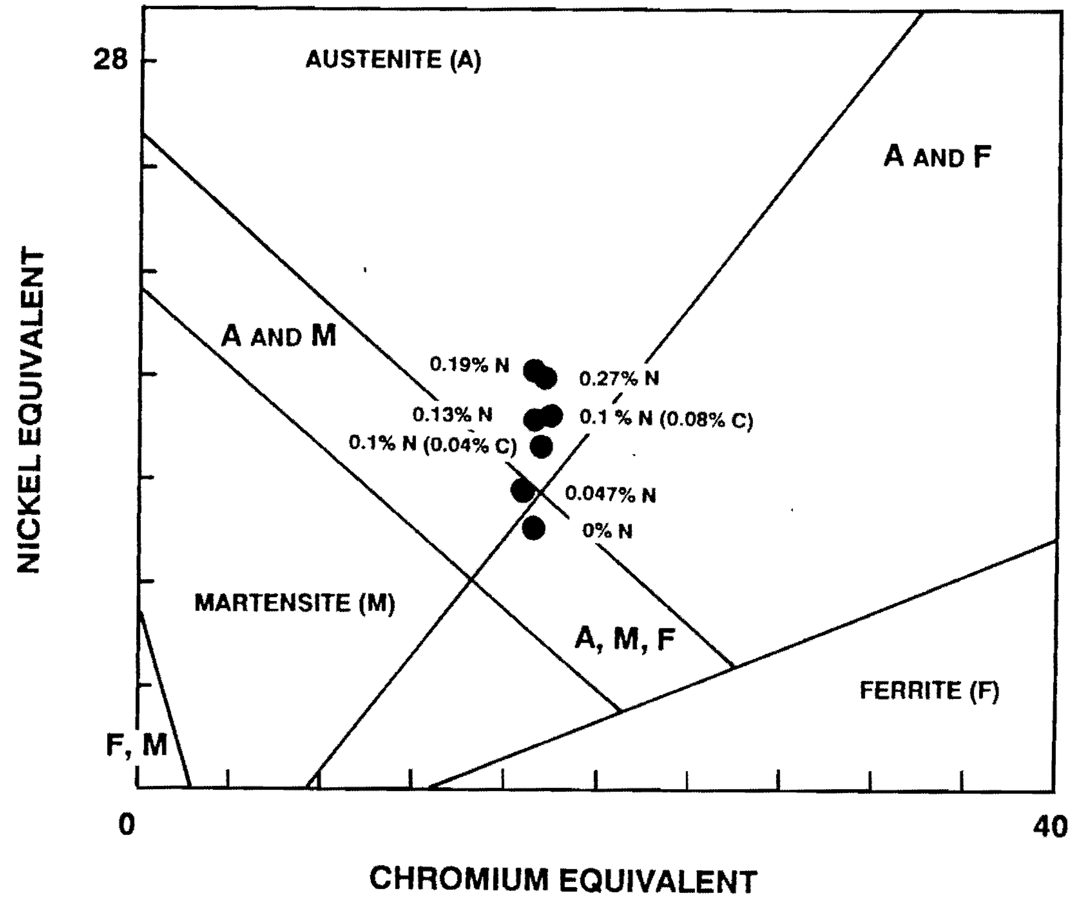

Fig 17: Schaeffler Diagram illustrating calculated phase fields for each alloy at room temperature

4.1.2 Metallography and X-Ray diffraction (XRD)

The microstructures of all the alloys were examined. The alloys containing 0.1 wt% and higher nitrogen have fully austenitic microstructures which is consistent with the Schaeffler Diagram predictions (Fig 17). A typical example of this microstructure is shown in Fig 18.

The 0.047 wt% nitrogen alloy comprises of a mixture of austenite and δ-ferrite. The possibility that some martensite could also be present cannot be excluded. XRD revealed that the proportion of bcc phase present was about 5 vol%. Point counting established the volume fraction of δ-ferrite at 5 vol%. The microstructure is illustrated in Fig 19, and although it suggests the presence of martensite, this is probably not a significant amount (less than 1 vol%). It has already been mentioned in section 3.4 that optical techniques always give a greater impression of the amount of martensite present.

Fig 18: Fully austenitic microstructure of 0.1 wt% N alloy etched with a mixture of chromic acid, acetic acid and distilled water as described in section 3.4.2.

The steel containing no nitrogen was observed to consist of a mixture of δ-ferrite, martensite and austenite. The δ-ferrite was present in a banded morphology. XRD revealed the volume fraction of austenite to be 75-79 vol%. Point counting of the δ-ferrite phase established the volume fractions of δ-ferrite to be 11 vol%. The amount of martensite present prior to straining is thus about 10-16 vol%. An example of this microstructure is shown in Fig 20.

A grain size of between 50-100 μm was observed for the nitrogen containing alloys and no substantial change of grain size with nitrogen content was observed. In the steel containing no nitrogen, however, a smaller grain size was observed in the region of 20 μm, which is due to grain refinement by the presence of δ-ferrite [36].

Annealing twins are visible in all the austenite phases across this alloy range, which is not unexpected in view of the fact that this alloy range is typically associated with low stacking fault energy.

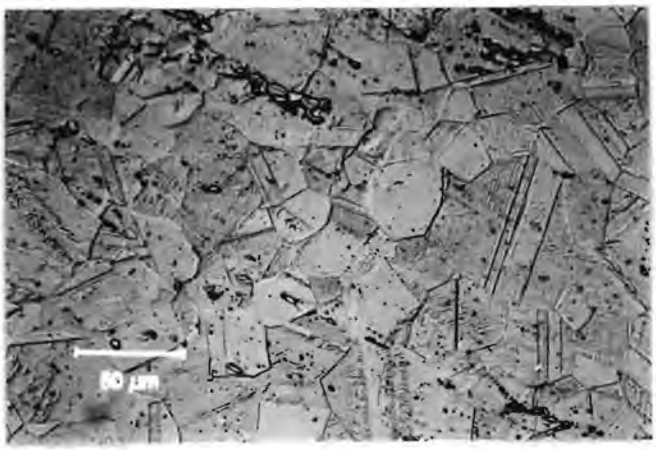

Fig 19: 0.047 wt% N alloy showing austenitic microstructure containing δ-ferrite (etched with acetic acid, chromic acid and distilled water as in section 3.4.2)

Fig 20: 0 wt% N alloy showing austenitic microstructure containing δ-ferrite and martensite (etched with oxalic acid as described in section 3.2.1)

4.1.3 A consideration of the austenite stability

The M_S and M_{d30} temperatures based on equations (3) and (4) respectively, page 46, have been calculated for all the alloys and are shown in Table 4. The tabulated M_S values suggest that the steel containing no nitrogen, is the only steel that should contain thermally induced martensite. A variety of M_S temperatures have been formulated, and utilising an equation by Lenel et al [16] to estimate the M_S temperatures suggests that all of the steels should form thermally induced martensite, whereas the M_S temperatures calculated by the equation proposed by Harris [14] suggests that none of the steels should form thermally induced martensite. These very diverse opinions reflect the composition dependence of these empirical equations. A plot of calculated M_{d30} temperatures versus nitrogen content (Fig 21) illustrates that the alloys with low nitrogen content are probably extremely unstable. It is anticipated that these alloys will undergo a transformation from austenite to martensite upon straining.

ALLOY	VF 689	VF 690	VF 688	VF 703	VF 692	VF 693	VF 679
wt% NITROGEN	0.000	0.047	0.100	0.130	0.190	0.270	0.100
M_S (°C) [18]	43.1	-33.9	-146.2	-185.3	-284.5	-416..8	-230.0
M_d (°C) [18]	66.1	43.6	12.7	1.1	-26.5	-63.25	-10.7

Table 4: Calculated Ms and Md30 temperatures of the alloy range

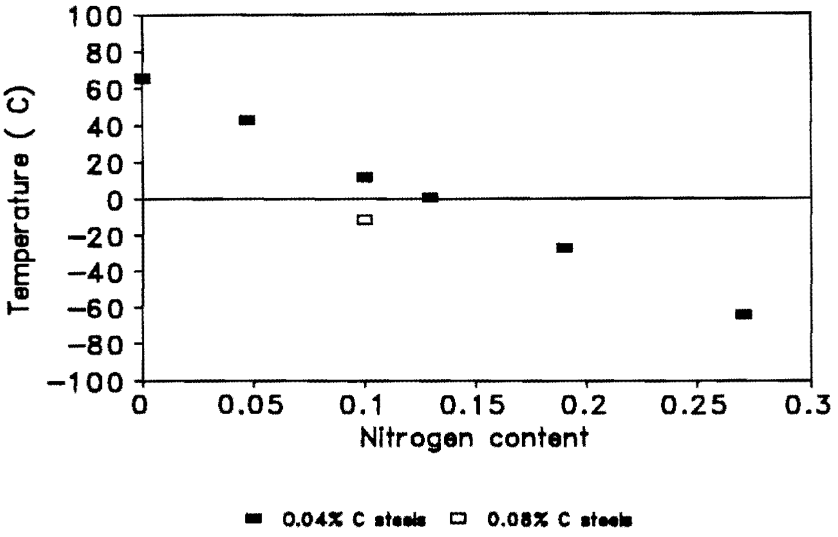

Fig 21: Theoretical M_{d30} [18] temperatures versus nitrogen content

4.2 TENSILE DEFORMATION BEHAVIOUR AT ROOM TEMPERATURE

4.2.1 True stress-true strain curves

The steels containing at least 0.13 wt% nitrogen exhibited true stress-true strain curves which were essentially parabolic in shape, as depicted in Fig 22 for the 0.27 wt% nitrogen steel. The lower nitrogen containing steels displayed true stress-true strain curves which were more sigmoidal in shape which is a consequence of the formation of strain-induced martensite. This is illustrated in Fig 23 where the true stress-true strain curve for the steel containing no nitrogen is shown. As the nitrogen content increases the degree of sigmoidal nature of the true stress / true strain curve diminishes and effectively disappears for nitrogen contents greater than 0.1 wt%.

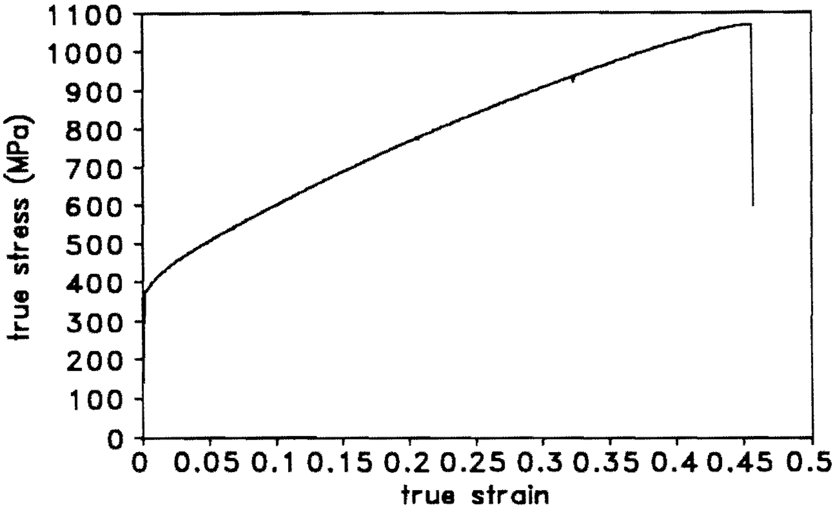

Fig 22: True stress-true strain curve for the 0.27 wt% N steel showing parabolic shape

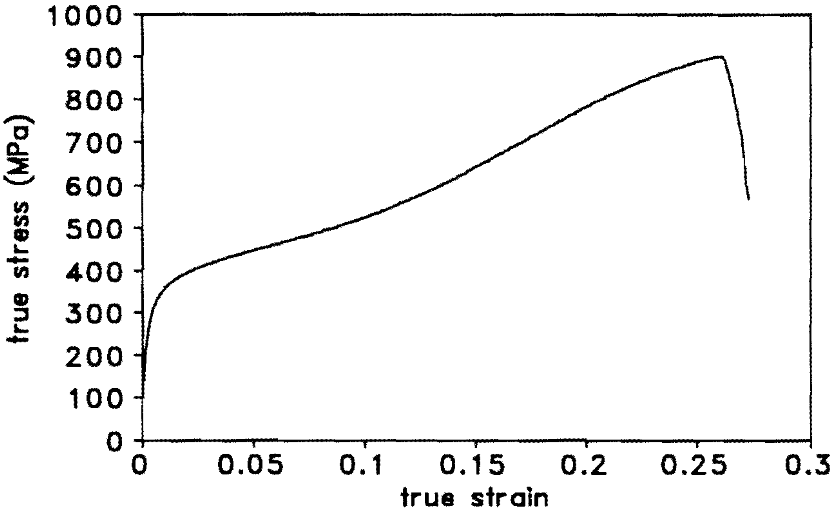

Fig 23: True stress-true strain curve for the 0.0 wt% N steel showing sigmoidal shape

4.2.2 Work hardening Rate Behaviour

The work hardening rate as a function of strain for the 0.27 wt% nitrogen alloy shows a parabolic decline, decreasing in an almost linear fashion with continuing strain as illustrated in Fig 24. The steel containing no nitrogen shows a similar initial parabolic decline at low strains (Fig 25), the work hardening rate actually dropping to a lower value than the higher nitrogen containing steel. At more acute strains, the WHR of this steel rapidly rises to a peak and then subsequently diminishes with continuing strain. A transition between these extreme modes in behaviour (Figs 24 and 25) occurs as the nitrogen content increases from 0 to 0.27 wt%. An increase in carbon content has an analogous influence to nitrogen on the WHR behaviour. The minimum in WHR was only observed in the 0 wt% and 0.047 wt% nitrogen steels, at a true strain of about 0.075. The WHR peak in these steels (Figs 25 and 26) are at 0.19 and 0.20 true strain respectively. The WHR peaks for 0.1 wt% nitrogen steel (0.04 wt% carbon) and 0.13 wt% nitrogen steel (Figs 27 and 28) are at about 0.30 true strain and 0.34 true strain respectively. As the nitrogen content of the alloys increases, the WHR peak height diminishes, until at 0.19 wt% N, the WHR at more acute strains appears to be constant as a function of strain (fig 29), as opposed to 0.27 wt% N where it actually decreases (Fig 24). The 0.08 wt% carbon, 0.1 wt% nitrogen steel exhibits WHR behaviour which is very similar to the 0.04 wt% carbon, 0.13 wt% nitrogen steel and is indicated by comparing Figs 30 and 28. Thus carbon can be considered to influence the WHR behaviour in a similar manner to nitrogen.

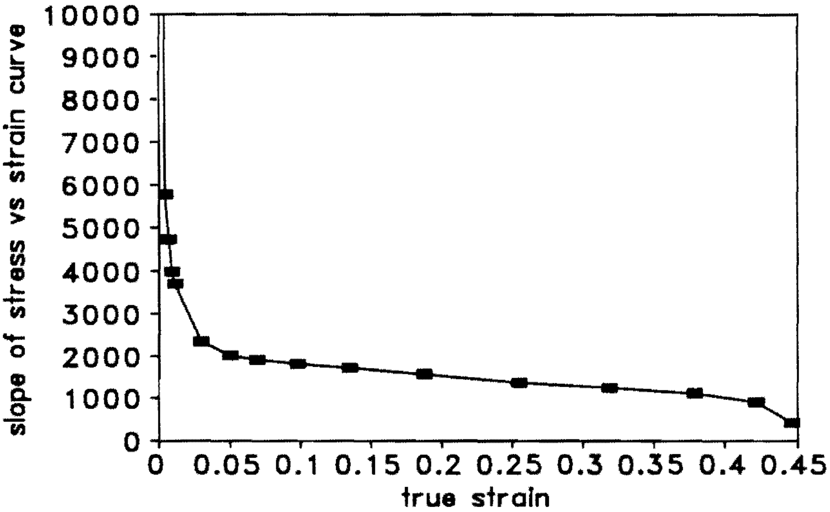

Fig 24: Work hardening Rate Behaviour of 0.27 wt% N and 0.04 wt% C steel at room temperature

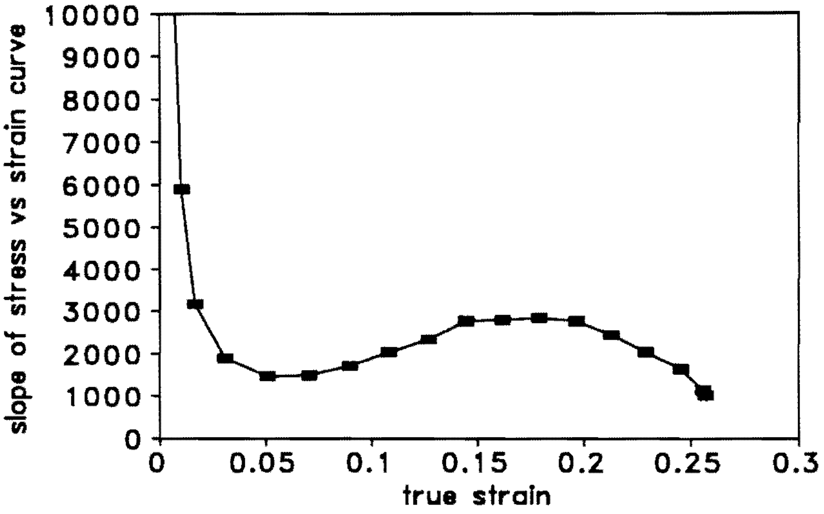

Fig 25: Work hardening Rate Behaviour of 0.0 wt% N and 0.04 wt% C steel at room temperature

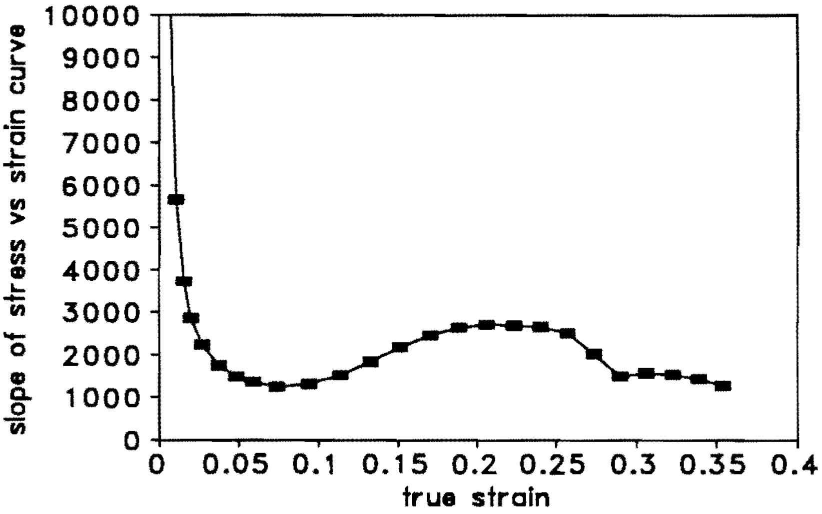

Fig 26: Work hardening Rate Behaviour of 0.047 wt% N and 0.04 wt% C steel at room temperature

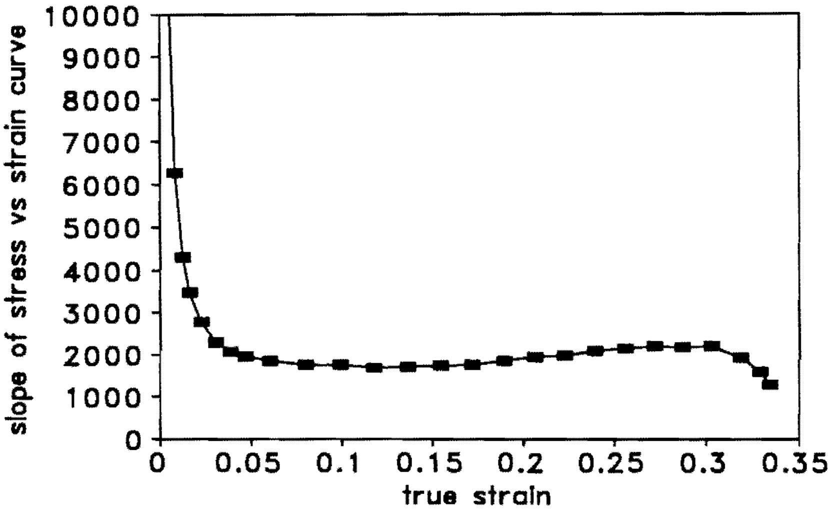

Fig 27: Work hardening Rate Behaviour of 0.10 wt% N and 0.04 wt% C at room temperature

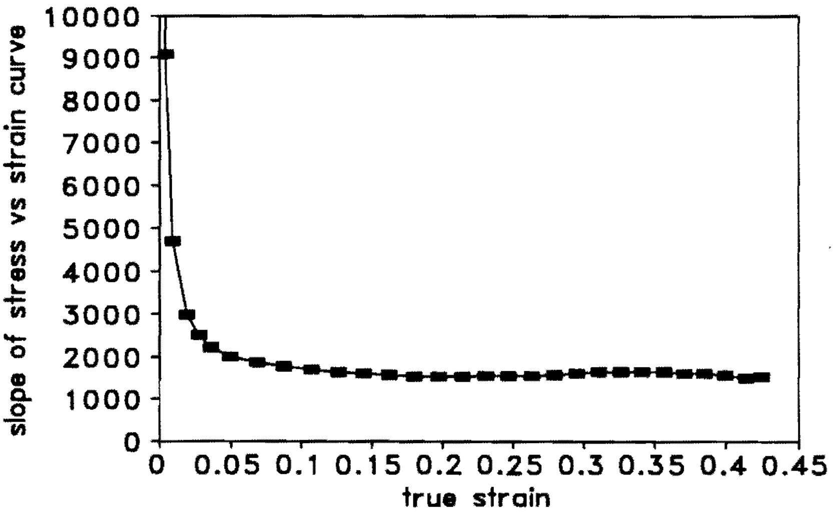

Fig 28: Work hardening Rate Behaviour of 0.13 wt% N and 0.04 wt% C steel at room temperature

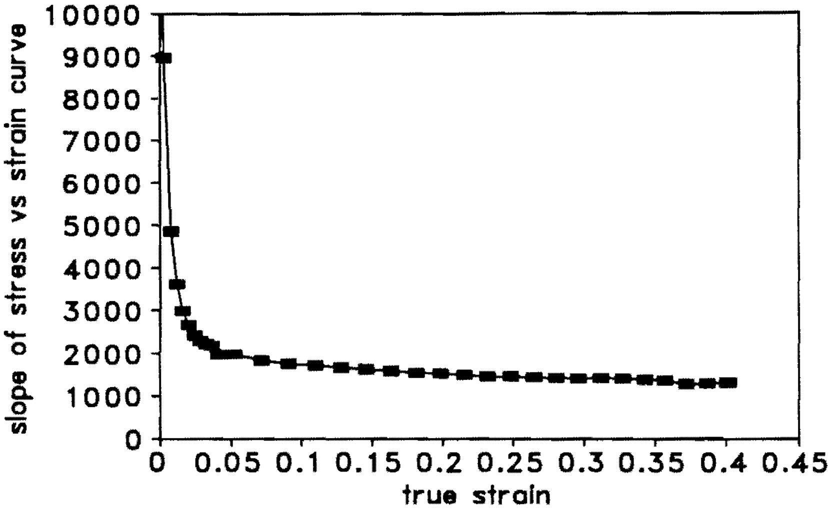

Fig 29: Work hardening Rate Behaviour of 0.19 wt% N and 0.04 wt% C steel at room temperature

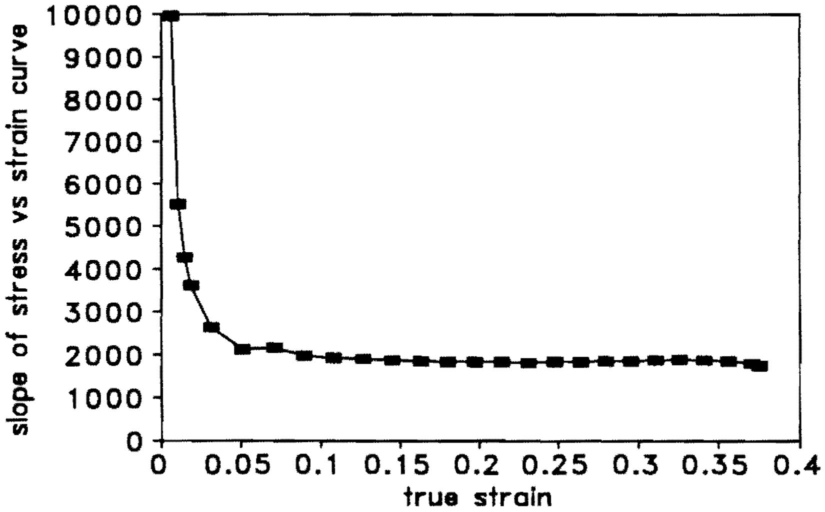

Fig 30: Work hardening Rate Behaviour of 0.10 wt% N and 0.08 wt% C steel at room temperature

4.2.3 Deformation-induced martensite

Examination of the strained microstructures (Fig 31) show the existence of slip bands within the austenite grains. In the low nitrogen steels the slip bands are thickened and this is associated with strain-induced martensite. The existence of strain-induced martensite has been confirmed by X-ray Diffraction (XRD).

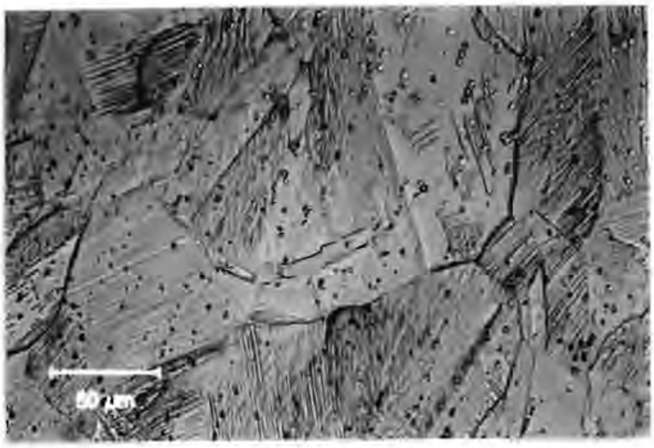

▲ 50 μm ▲

Fig 31: Deformed microstructure of 0.1 wt% N, 0.04 wt% C alloy after 0.30 true strain, showing slip bands and suggesting the presence of martensite, (etched with etchant 1)

The amount of retained austenite present in each alloy after 0.07, 0.20 and 0.30 true strain, has been calculated using XRD and is shown in Table 5. The amount of retained austenite present in the alloys as a function of nitrogen content, and strain, is depicted graphically in Fig 32 and Fig 33 respectively. The 0.27 wt% nitrogen alloy was magnetic at fracture, suggesting that at this strain level, a transformation from austenite to martensite had initiated. In the steels containing less than 0.13 wt% nitrogen, ϵ-martensite is present in small volumes at minor strains (0.07), but disappears at higher strains. In this alloy range the amount of strain-induced martensite increases with increasing strain and decreasing nitrogen. Fig 33 shows that the relationship between the amount of martensite against elongation is linear at low nitrogen values and sigmoidal at higher values.

wt% N	wt% C	0 STRAIN	0.07 STRAIN	0.20 STRAIN	0.30 STRAIN
0.000	0.04	77.0	64.27	26.22	-
0.047	0.04	95.0	88.04	50.42	21.60
0.100	0.04	100.0	100.0	88.93	55.56
0.130	0.04	100.0	100.0	96.67	82.40
0.190	0.04	100.0	100.0	100.0	95.36
0.270	0.04	100.0	100.0	100.0	100.0
0.100	0.08	100.0	100.0	94.30	79.10

Table 5: Amount of retained austenite (%) at a particular strain

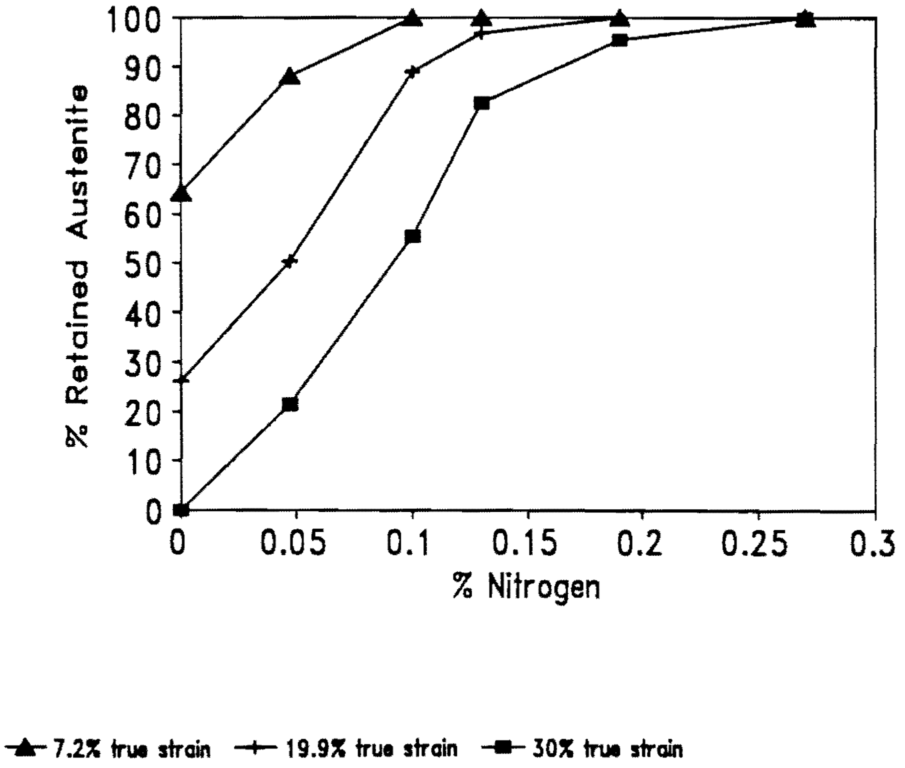

Fig 32: The amount of retained austenite as a function of nitrogen content

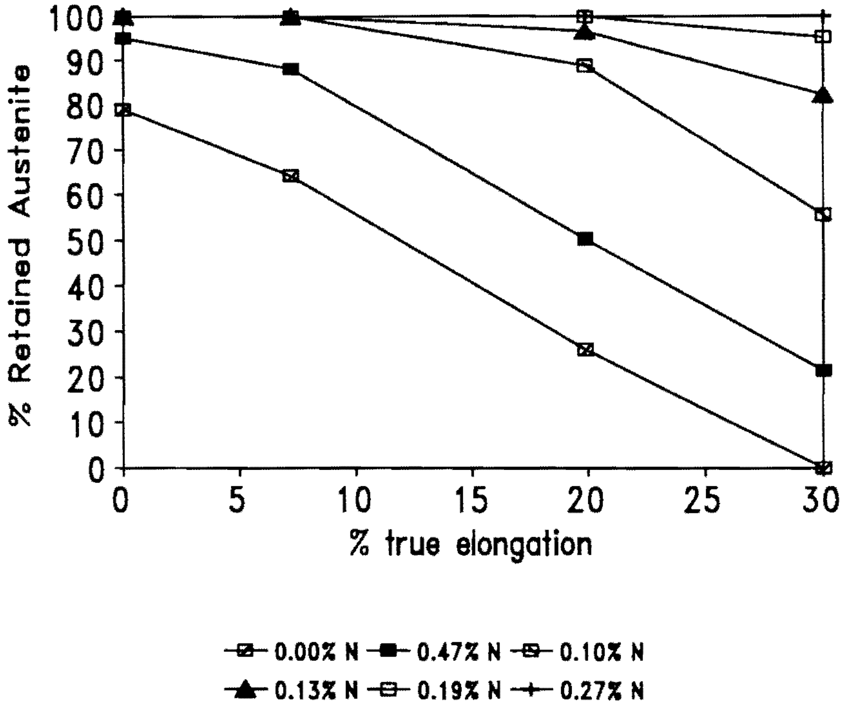

Fig 33: The amount of retained austenite as a function of elongation for a range of nitrogen alloyed steels

4.2.4 Mechanical Properties

In the graphs that follow each symbol represents the result from an individual tensile test.

a) Ultimate tensile strength (UTS)

The variation of tensile strength with nitrogen content has been illustrated in Fig 34. Nitrogen does not appear to exert an influence on the tensile strength, in the high nitrogen containing steels. It is worth noting that the 0.047 wt% N steel has a much higher UTS than any other alloy of equivalent carbon content. Increasing the carbon content from 0.04 wt% to 0.08 wt%, results in a higher UTS, for a nitrogen content of 0.1 wt%.

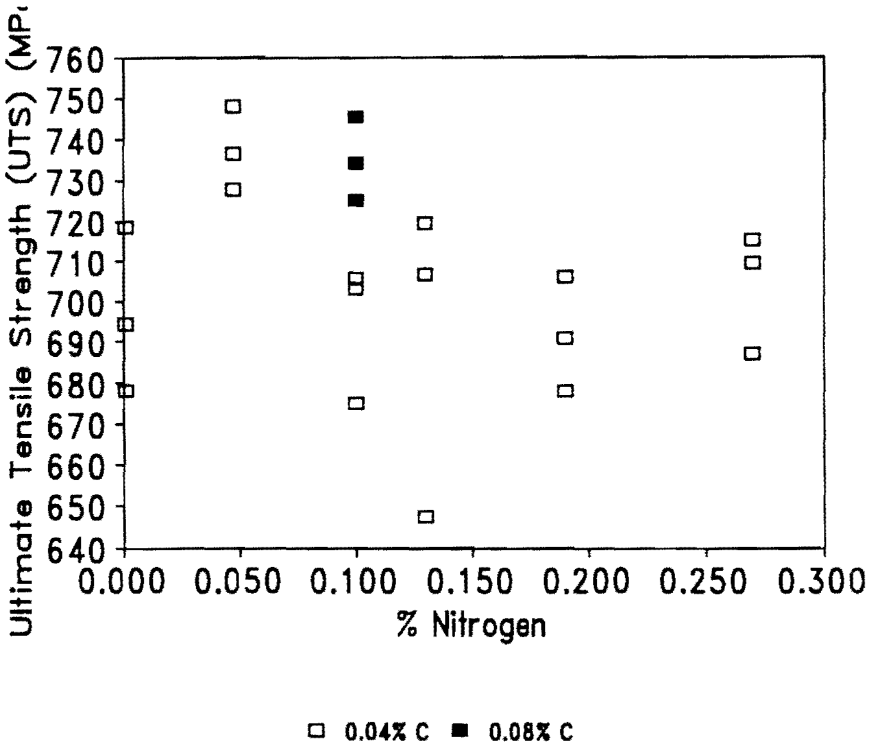

Fig 34: Tensile strength, at room temperature, versus nitrogen content

b) Yield Strength

As the nitrogen content is raised, the yield strength initially decreases reaching a minimum at 0.1 wt% nitrogen content, after which it rapidly rises with increasing nitrogen content (Fig 35). Increasing the carbon content of the 0.1 wt% N alloy produces a higher yield strength.

c) Maximum uniform elongation (MUE)

The steel containing no nitrogen exhibits a maximum uniform elongation (MUE) considerably lower than any of the other alloys. The 0.1 wt% nitrogen containing steel exhibits the next lowest MUE, whilst the 0.13 wt% nitrogen containing alloy, undergoes the optimum MUE. These results are shown in Fig 36. Increasing the carbon content in the 0.1 wt% alloy produces a slight increase in MUE.

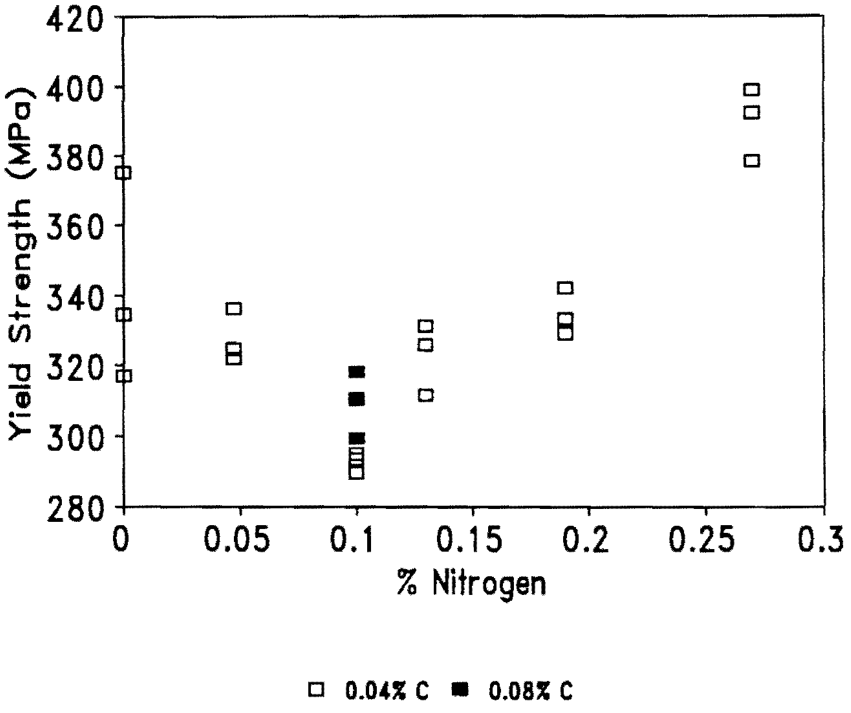

Fig 35: Yield Strength at room temperature, versus nitrogen content

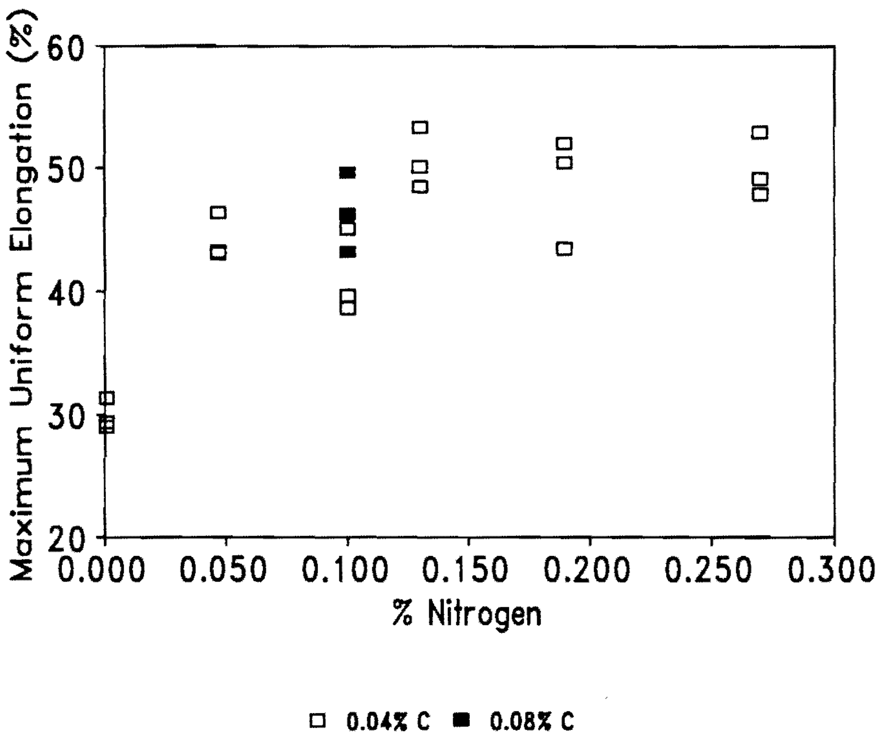

Fig 36: Maximum Uniform Elongation, at room temperature, versus nitrogen content

4.2.5 Bulk Hardness of solution treated alloys

As the nitrogen content increases the bulk hardness decreases until a nitrogen content of 0.13 wt% is reached, after which the bulk hardness increases with further increases in nitrogen content. The error bars depicted in the graph of hardness against nitrogen content (Fig 37) represent the statistical deviation on at least five tests. An increases in the carbon content of the 0.1 wt% nitrogen alloy resulted in an increase in bulk hardness.

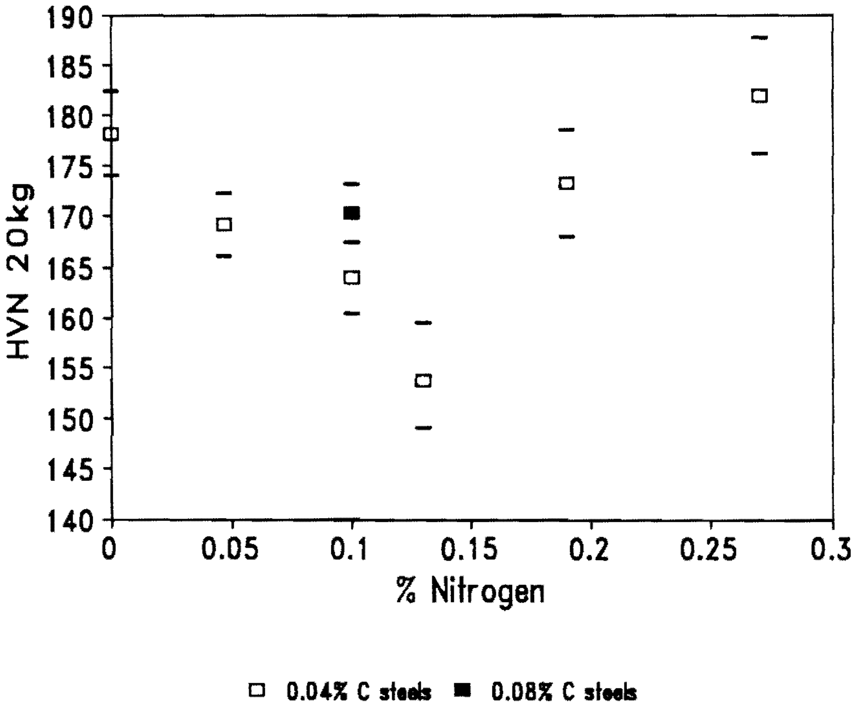

Fig 37: Bulk Hardness, at room temperature, versus nitrogen content

4.2.6 Microhardness as a function of Cold Work

The variation of microhardness with cold work was calculated for all the alloys. These variations are shown below in Fig 38, Fig 39 and Fig 40 for three of the alloys.. As the amount of cold work increases the microhardness, which is an indication of flow stress, increases. At high and low nitrogen values the increase in microhardness is linear with deformation, whereas for intermediate nitrogen contents the increase is parabolic in shape. In these intermediate nitrogen regions, the hardening occurs at a greater rate at lower deformation levels.

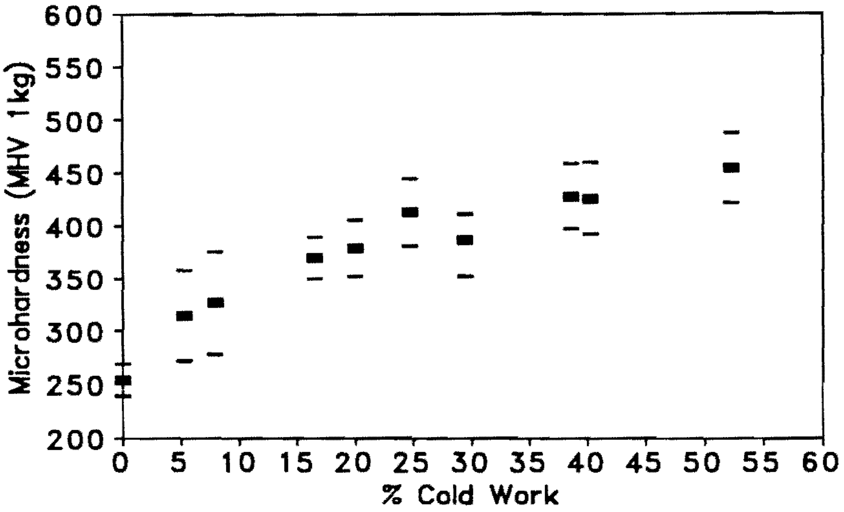

Fig 38: The Effect of Cold Work on the Microhardness for the 0.047 wt% nitrogen alloy

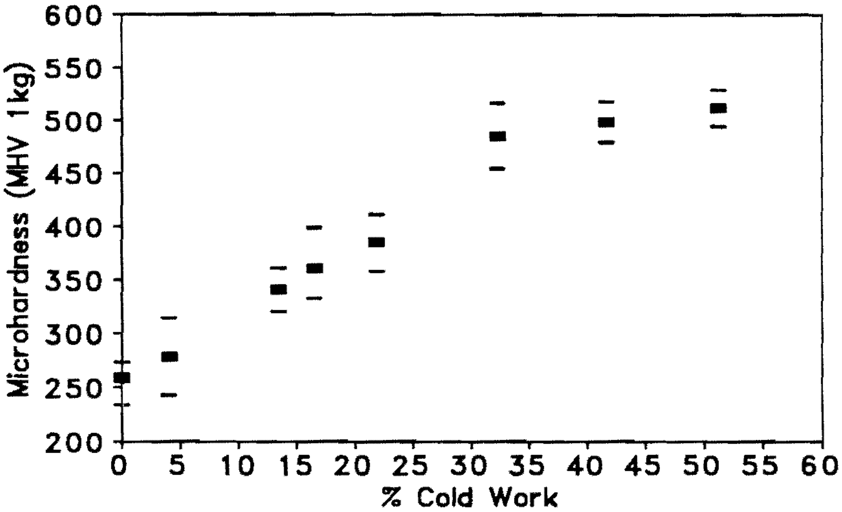

Fig 39: The Effect of Cold Work on the Microhardness for the 0.13 wt% nitrogen alloy

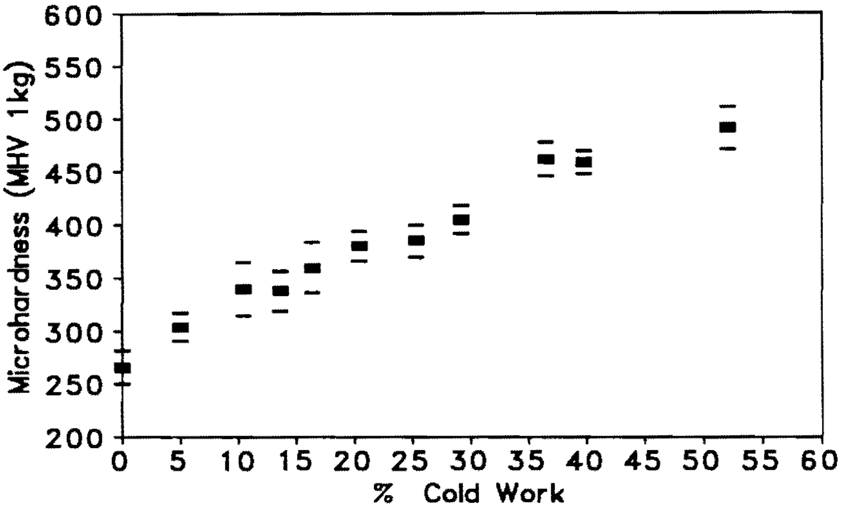

Fig 40: The Effect of Cold Work on the Microhardness for the 0.27 wt% nitrogen alloy

The slopes of the microhardness versus cold work curves were calculated using a linear regression analysis and are shown below in Fig 41.

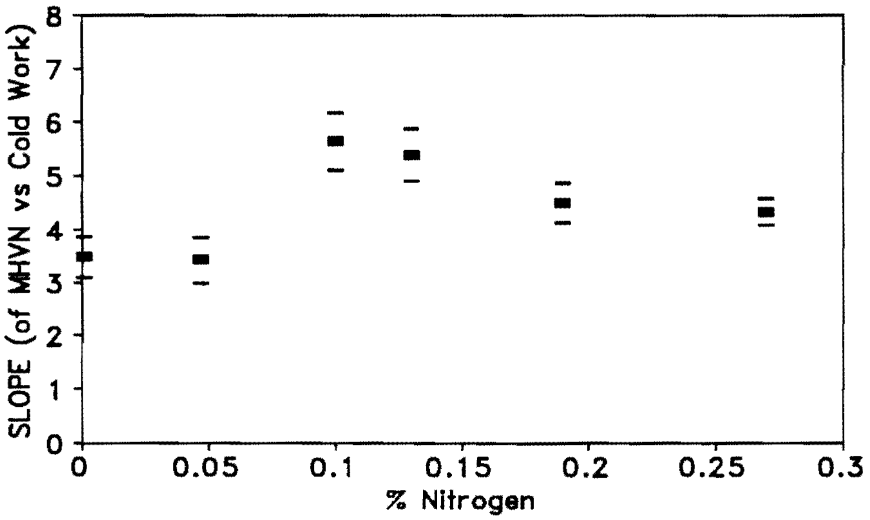

Fig 41: The rate of change of microhardness with cold work, for varying nitrogen alloys

Although the intermediate nitrogen alloys show a parabolic relationship, a linear regression has been applied. The initial slopes in these intermediate nitrogen alloys would in fact be higher if the slope was calculated as a function of cold work. The slope is an indication of the microhardness sensitivity to the amount of cold work experienced. The rate of hardening (slope) increases as the nitrogen content increases to 0.1 wt% after which it steadily decreases.

4.2.7 Formability Behaviour

An indication of the formability of the alloys was measured by performing Erichsen cupping tests. The depth of indentation versus nitrogen content is plotted in Fig 42. The alloy containing no nitrogen exhibited the least formability and increasing the nitrogen content up to 0.1 wt% resulted in an increase in formability after which the behaviour tends to level off with further increases in nitrogen content. Increasing the carbon content to 0.08 wt% in the 0.1 wt% nitrogen alloy does not alter the formability significantly.

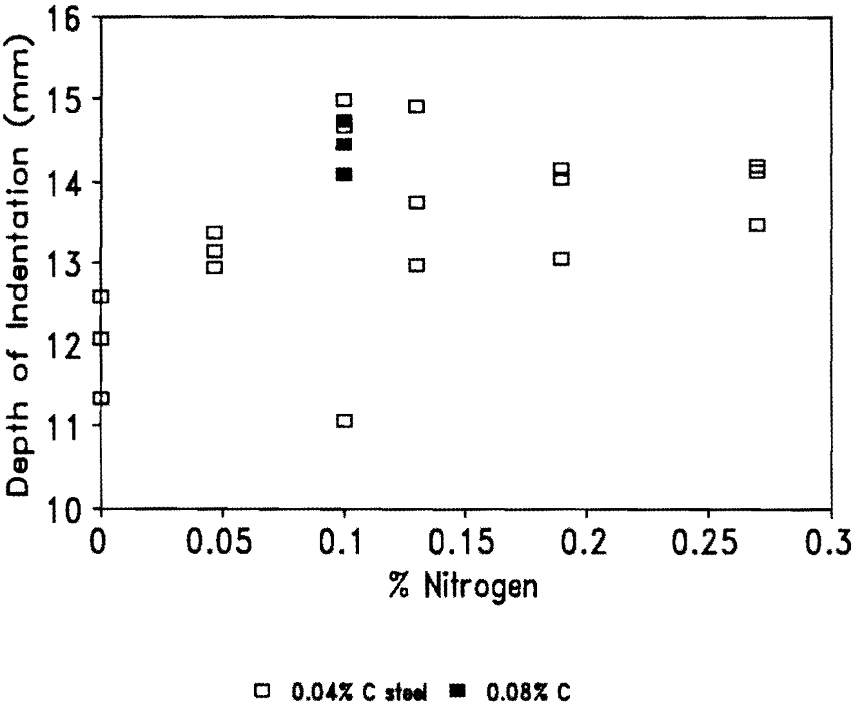

Fig 42: Formability versus nitrogen content

4.3 TENSILE DEFORMATION BEHAVIOUR AT ELEVATED TEMPERATURE (120 °C)

The aims of elevated temperature tensile testing were to observe the variation of mechanical behaviour with nitrogen content in the absence of a strain-induced transformation to martensite, thus simplifying the factors contributing to the strengthening behaviour of the alloys and to provide evidence of solid solutiion strengthening. A temperature of 120°C was selected as likely to be above the actual M_d of the alloys.

4.3.1 True stress-true strain curves

Unlike the room temperature tests, all the true stress-true strain curves are parabolic in shape which advocates the idea that no strain-induced martensite is being formed. The curve for the alloy containing no nitrogen is illustrated in Fig 43 and can be contrasted with the curve obtained for the same alloy, at room temperature, as depicted in Fig 23, page 48.

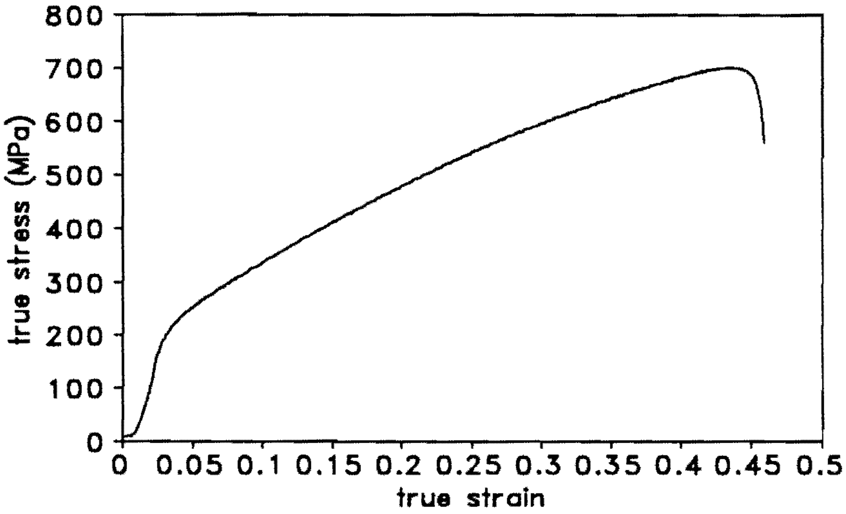

Fig 43: True stress-true strain curve, at 120°C, for alloy containing no nitrogen

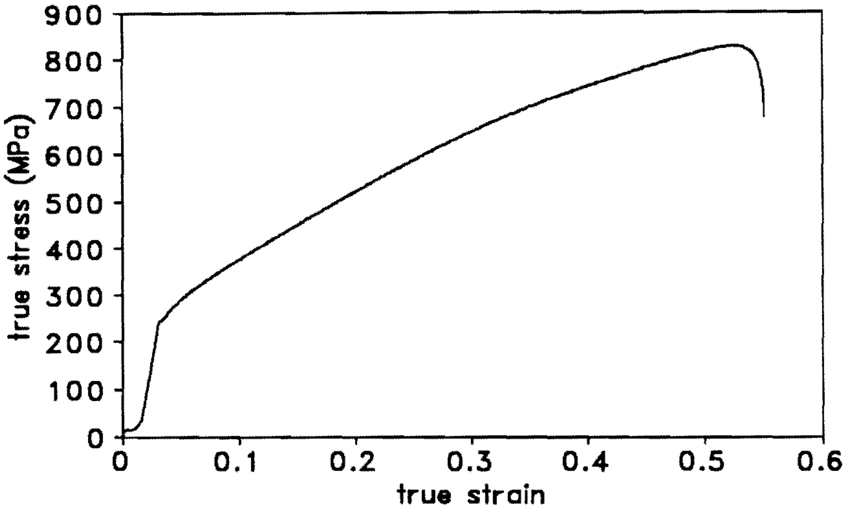

Fig 44: True stress-true strain curve, at 120°C, for alloy containing 0.27 wt% nitrogen

4.3.2 Work hardening Rate Behaviour

The work hardening rate behaviour of these steels showed no change in behaviour as a function of nitrogen content at 120°C. There were no changes that could be attributed to the formation of strain-induced martensite. The work hardening behaviour is illustrated for a low and high nitrogen alloy in Fig 45 and Fig 46 respectively.

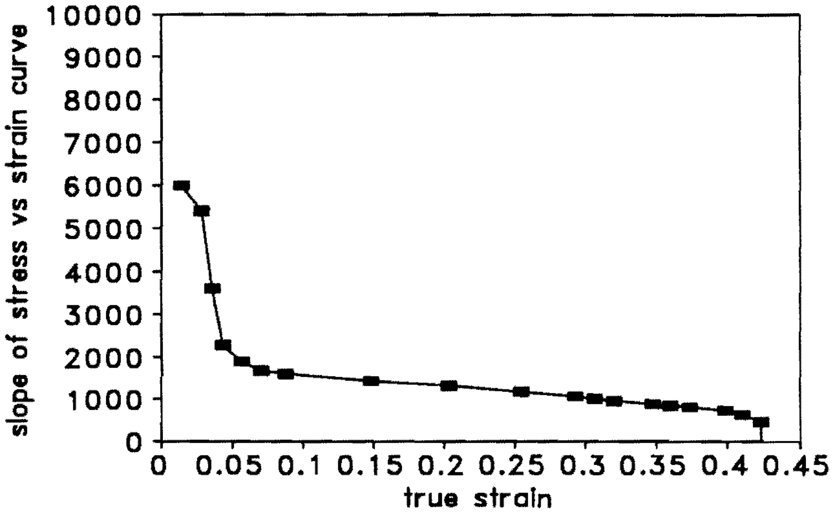

Fig 45: Work hardening Rate Behaviour of 0.0 wt% N steel at 120 °C

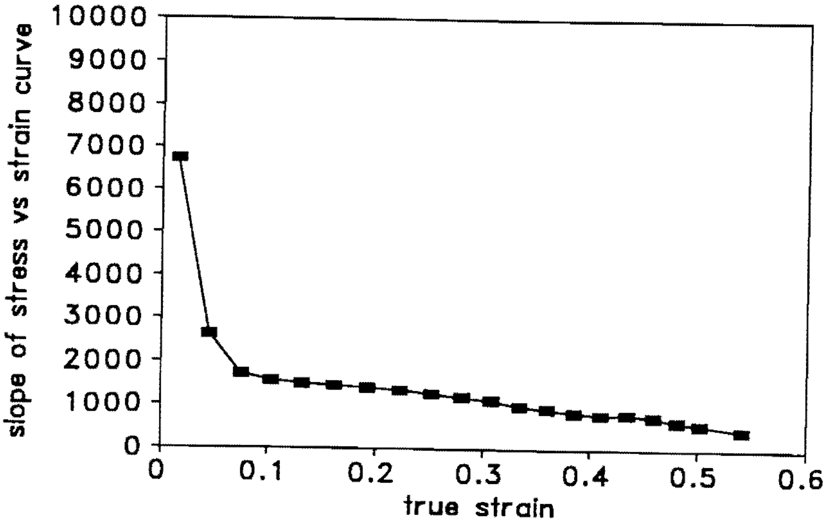

Fig 46: Work hardening Rate Behaviour of 0.27 wt% N steel at 120 °C

4.3.3 Mechanical Properties

Again, each symbol on the following graphs, represents an individual tensile test result.

a) Ultimate tensile strength (UTS)

At 120°C, as the nitrogen content is raised, an increase in tensile strength is measured, which becomes more pronounced at higher nitrogen values. Increasing the carbon content in the 0.1 wt% nitrogen alloy, however, results in an elevated UTS. This is depicted in Fig 47 below.

b) Yield Strength

Nitrogen exerts a similar influence on the yield strength (Fig 48) to that which it exerts on the UTS. The strengthening due to nitrogen can be seen to be more effective at higher nitrogen contents. The 0.08 wt% carbon alloy was tested twice (data points are superimposed) and found to have a higher yield strength than the 0.04 wt% carbon alloy.

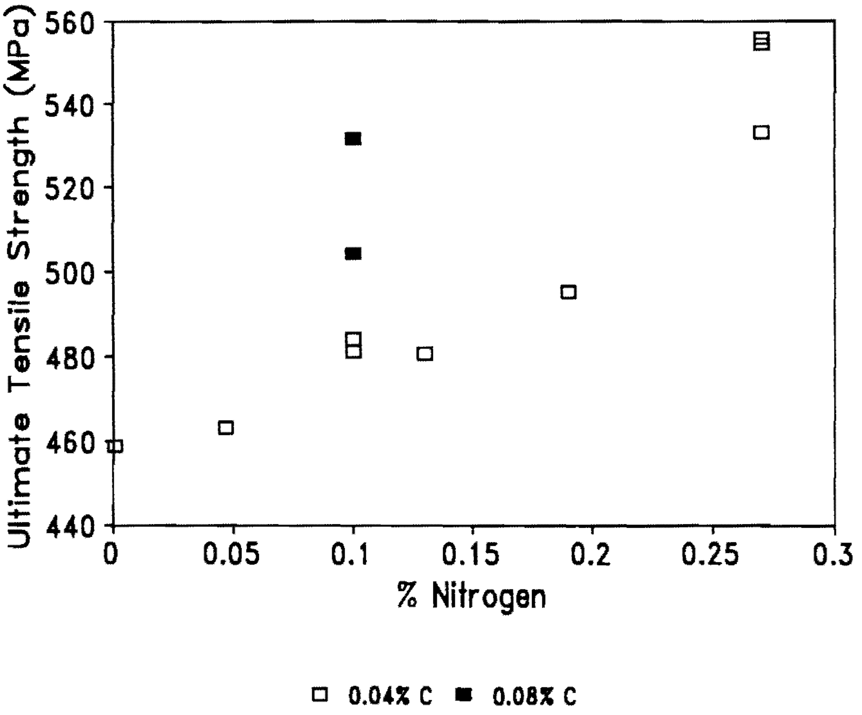

Fig 47: Tensile strength at 120°C, versus nitrogen content

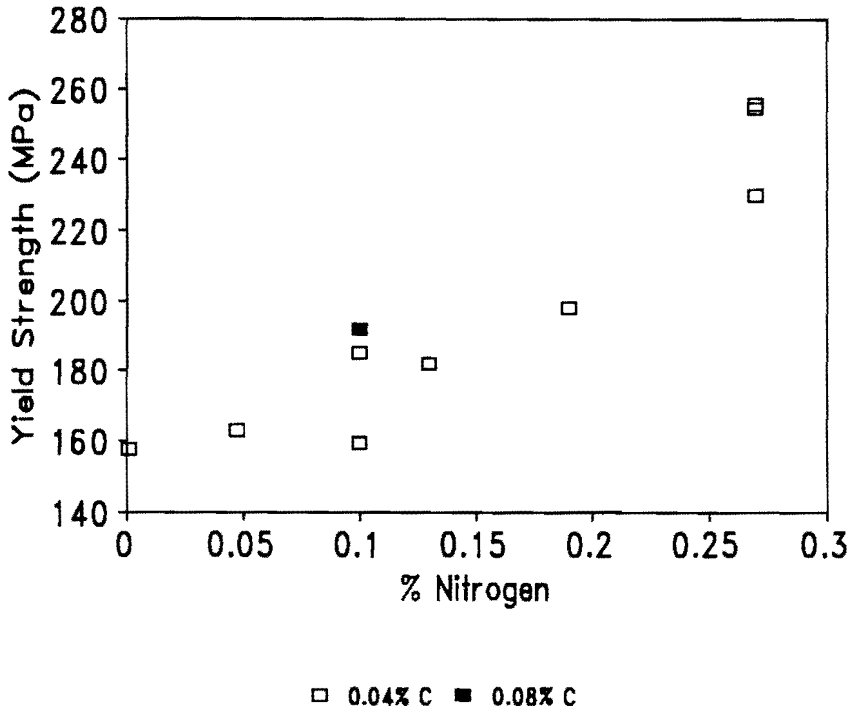

Fig 48: Yield strength at 120°C, versus nitrogen content

c) Maximum uniform elongation (MUE)

The maximum uniform elongation of the 0.1 wt% nitrogen alloys are slightly higher than any other alloys. The elongations of the other steels were similar, in the region of 40%. However, there is a large scatter in MUE at 0.27 wt% nitrogen which could be due to experimental errors. If the results for the 0.27 wt% nitrogen alloy are valid, this implies that the MUE's for the 0.1 wt% nitrogen alloys are not significantly different to the other alloys. Increasing the carbon content does not appear to have an effect on the MUE. This behaviour is shown in Fig 49.

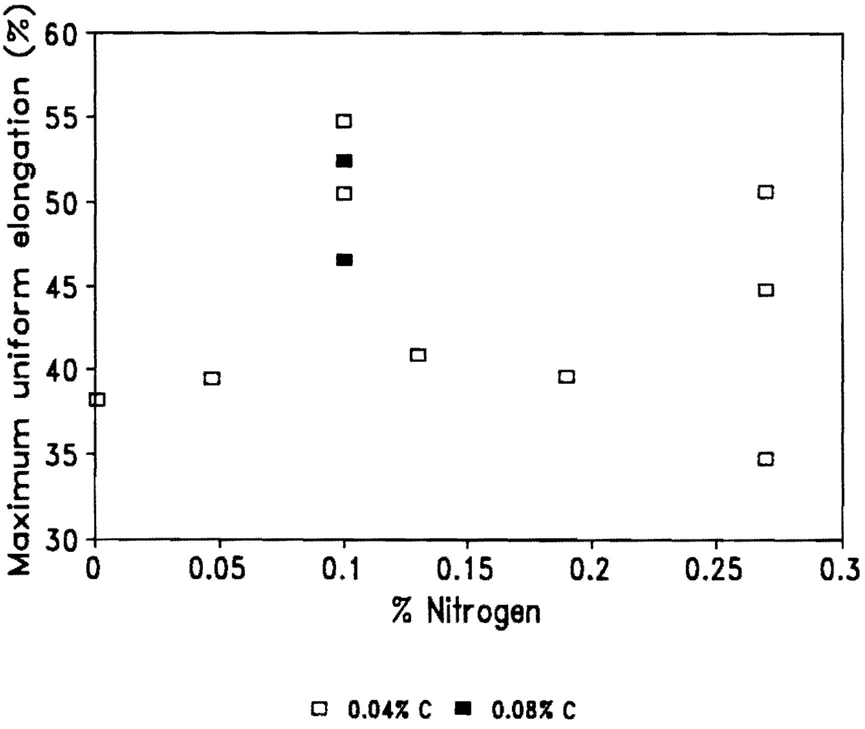

Fig 49: Maximum Uniform Elongation, at 120°C, versus nitrogen content

4.4 MICROSTRUCTURAL CHANGES WITH NITROGEN CONTENT AND DEFORMATION:

4.4.1 Annealed state:

a) General Observations

All the alloys were subjected to cold rolling before they were annealed. Transmission electron microscopy of the materials in the annealed state revealed an essentially strain-free microstructure containing numerous stacking faults, annealing twins and discrete dislocations. The presence of stacking faults and annealing twins is a consequence of the low stacking fault energy of this alloy range. A typical field of view is shown in fig 50 where stacking faults and dislocations are evident within two adjacent grains of the 0.19 wt% nitrogen alloy. The stacking faults are adjacent to the grain boundary. Selected area zone-axis electron diffraction patterns provide evidence of martensite (α' and ϵ) in the 0 wt% nitrogen alloy in the annealed state.

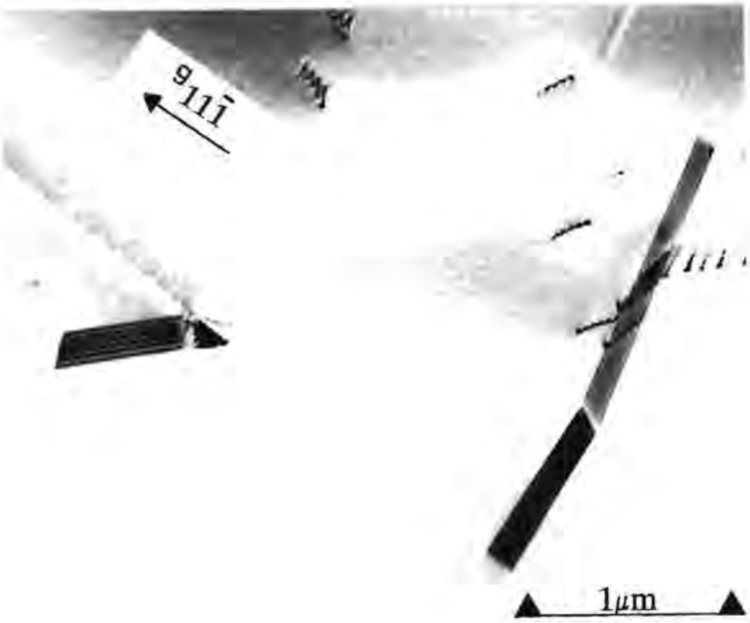

Fig 50: Stacking faults against a grain boundary in the 0.19 wt% nitrogen steel in the annealed state

b) Variation of Stacking Fault Energy with Nitrogen Content

Qualitative examinations of all the alloys in the annealed state suggest that as the nitrogen content increases the stacking fault density decreases. This implies that as the nitrogen content increases, the stacking fault energy (SFE) increases. Fig 51 shows overlapping stacking faults as well as dislocations in the 0.047 wt% nitrogen steel.

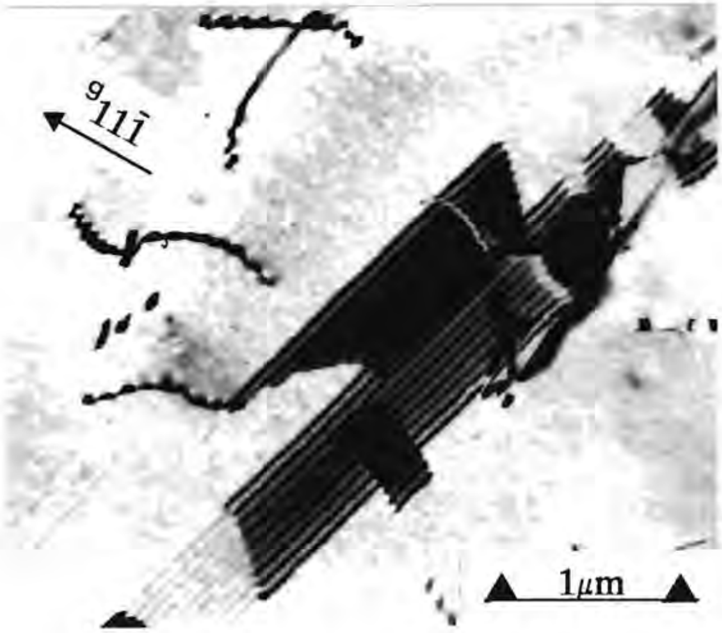

Fig 51: Overlapping of stacking faults in the 0.047 wt% nitrogen containing steel in the annealed state

4.4.2 Deformed Specimens

Specimens, which had been tensile strained 0.07, 0.20 and 0.30 true strain, were examined. As the strain increased, the density of dislocations and stacking faults was observed to increase. The plastic deformation of the steels occurs by a combination of planar glide and mechanical twinning.

a) Observations of twins

Deformation twins became more noticeable with increasing strain and decreasing nitrogen content. An annealing twin containing deformation twins, is shown in Fig 52 and deformation twins are shown for the low and high nitrogen alloys in Figs 53 and 54. The presence of twinning is confirmed by examination of the electron diffraction patterns which reveal additional reflections. In order to determine which microstructural features in Fig 53 give rise to produce the additional reflections observed in a selected area diffraction pattern, dark field images were recorded with the objective aperture placed over the additional reflections.

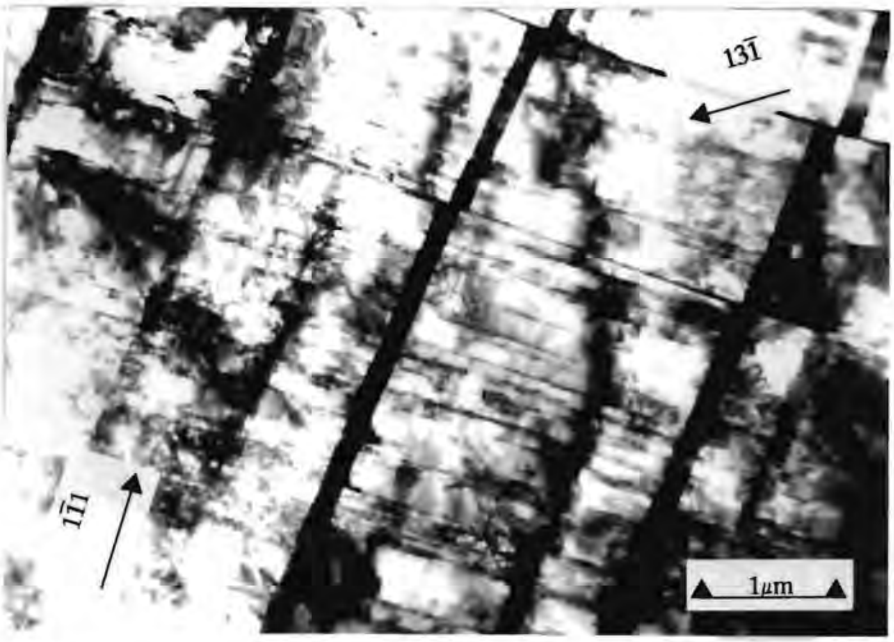

Fig 52: Bright field TEM showing annealing twin containing deformation twins in the 0.27 wt% nitrogen alloy at 0.07 strain, imaged in an [112] austenite zone axis

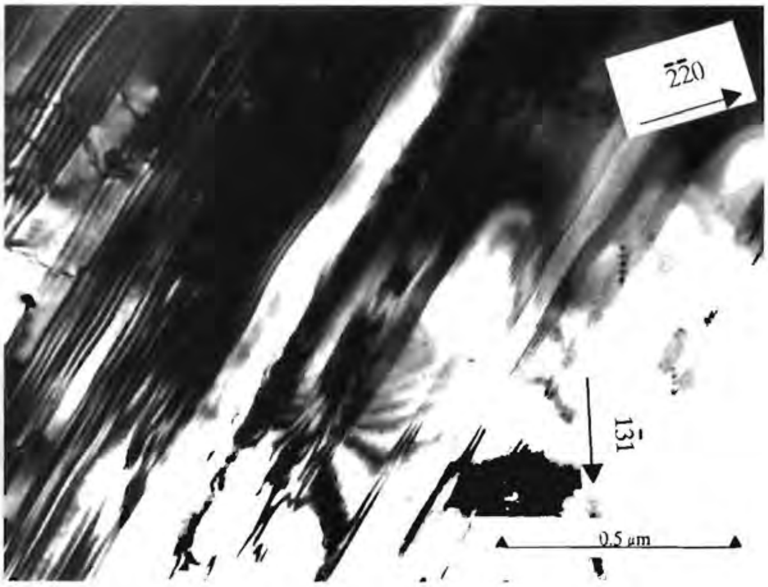

Fig 53: Bright field TEM showing deformation twins in a 0 wt% nitrogen alloy deformed to a true strain of 0.07, imaged in an [114] austenite zone axis

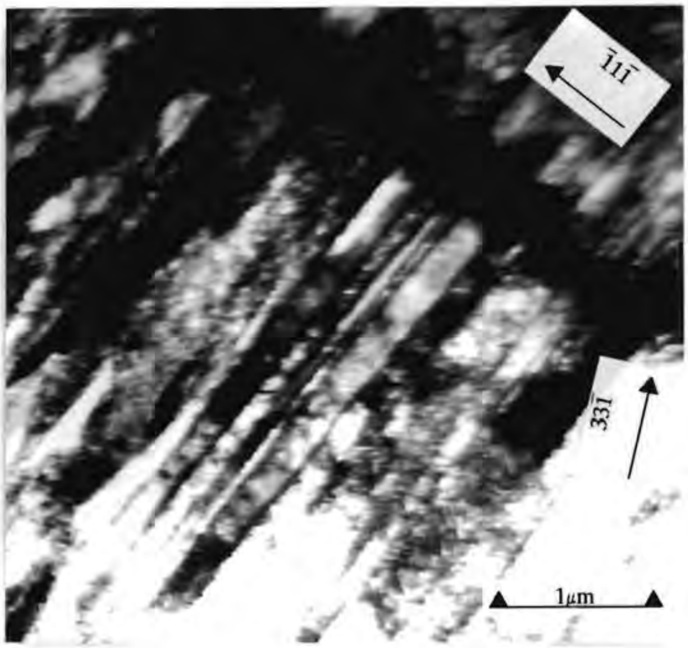

Fig 54: Bright field TEM showing deformation twins imaged in an [112] austenite zone axis of the 0.27 wt% nitrogen alloy deformed to a true strain of 0.20

b) Observations of martensite

Although ε-martensite is similar in appearance to deformation twins, the selected area diffraction patterns for ε-martensite and twins in the $[1\bar{1}0]$ zone axis are shown in Figs 55a and 56 respectively where it can be clearly seen that additional reflections due to each feature are distinctive. This point is further illustrated in the schematic zone axis diffraction patterns shown in Fig 55b and 57.

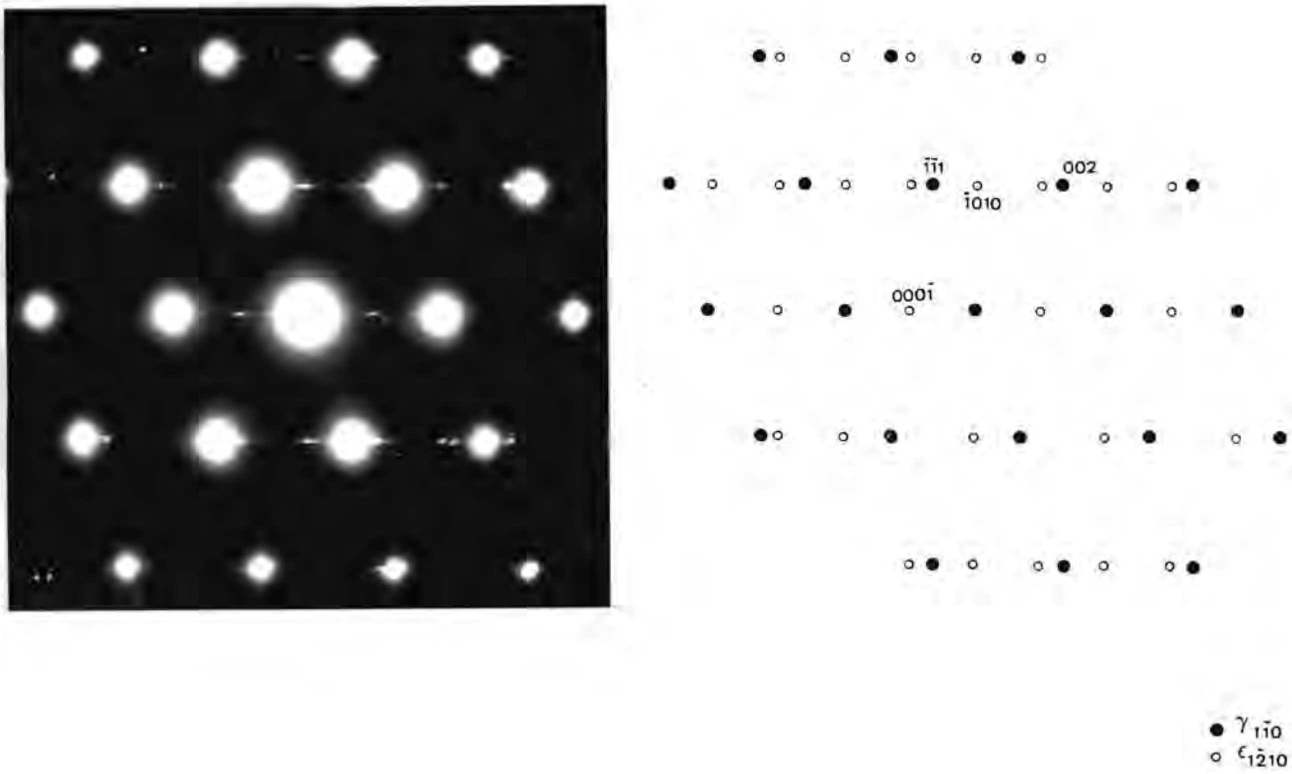

a) b)

Fig 55: a) The selected area diffraction pattern associated with ε-martensite in an austenite matrix shown in Fig 58 showing the $[1\bar{1}0]_\gamma$ and $[1\bar{2}10]_\varepsilon$ zone axes
b) The schematic for a)

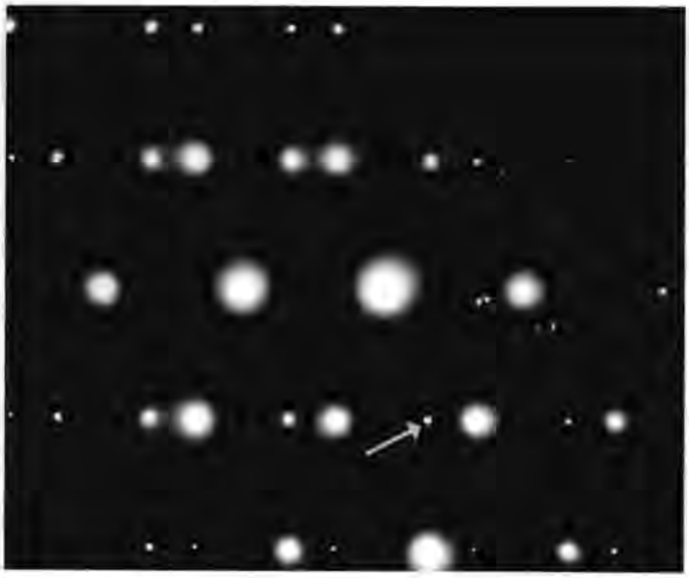

Fig 56: The selected area diffraction pattern associated with twins in an austenite matrix showing the $[1\bar{1}0]_\gamma$ zone axis

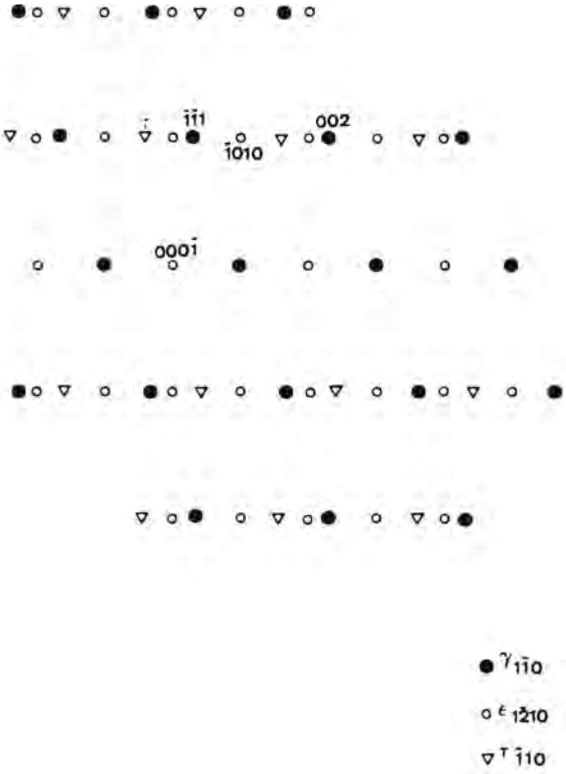

Fig 57: A Schematic showing the positions of the reflections for ϵ-martensite and twins in the same $[1\bar{1}0]_\gamma$ zone axis

Electron diffraction patterns revealed the presence of ϵ-martensite at low strains in the low nitrogen steels. ϵ-martensite was usually observed at the intersections of stacking faults and this is clearly depicted in Fig 58. The ϵ-martensite had an orientation relationship of $[\bar{1}2\bar{1}0]$ with the $[\bar{1}10]$ austenite zone axis.

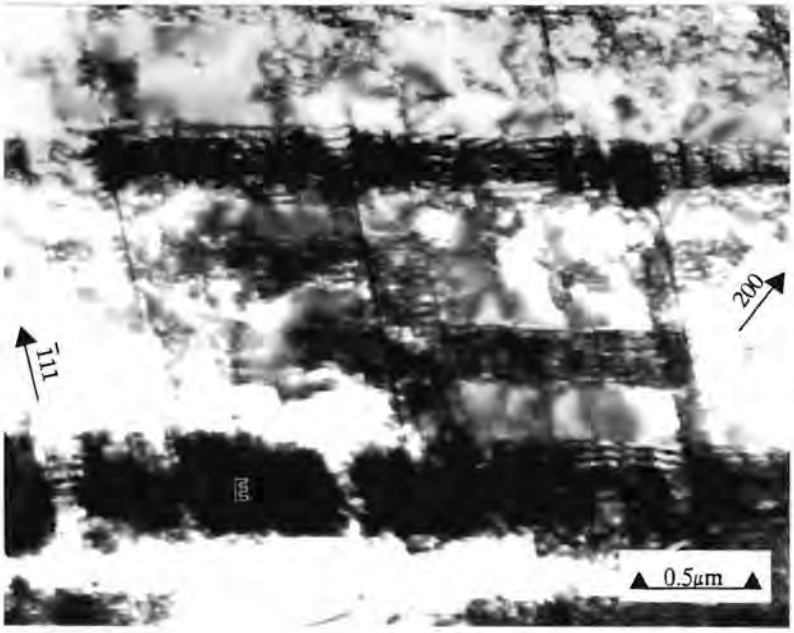

Fig 58: Bright field TEM micrograph showing ϵ-martensite in an austenite matrix of the 0 wt% nitrogen alloy at 0.07 true strain

At higher strains, the presence of α'-martensite was revealed. α'-martensite was often observed in conjunction with ε-martensite, strongly suggesting that α'-martensite nucleates from the ε-martensite. This is illustrated in Fig 60 and selected area electron diffraction analysis (Fig 59) suggests that the austenite and α'-martensite have a Kurdjumov-Sachs (K-S) orientation relationship. A dark field image with the aperture placed over the ε-martensite reflection labelled in Fig 59 was obtained (Fig 61) and reveals that the thin bands are associated with ε-martensite. It can be seen in Fig 60 that the ε-martensite is aligned with stacking faults.

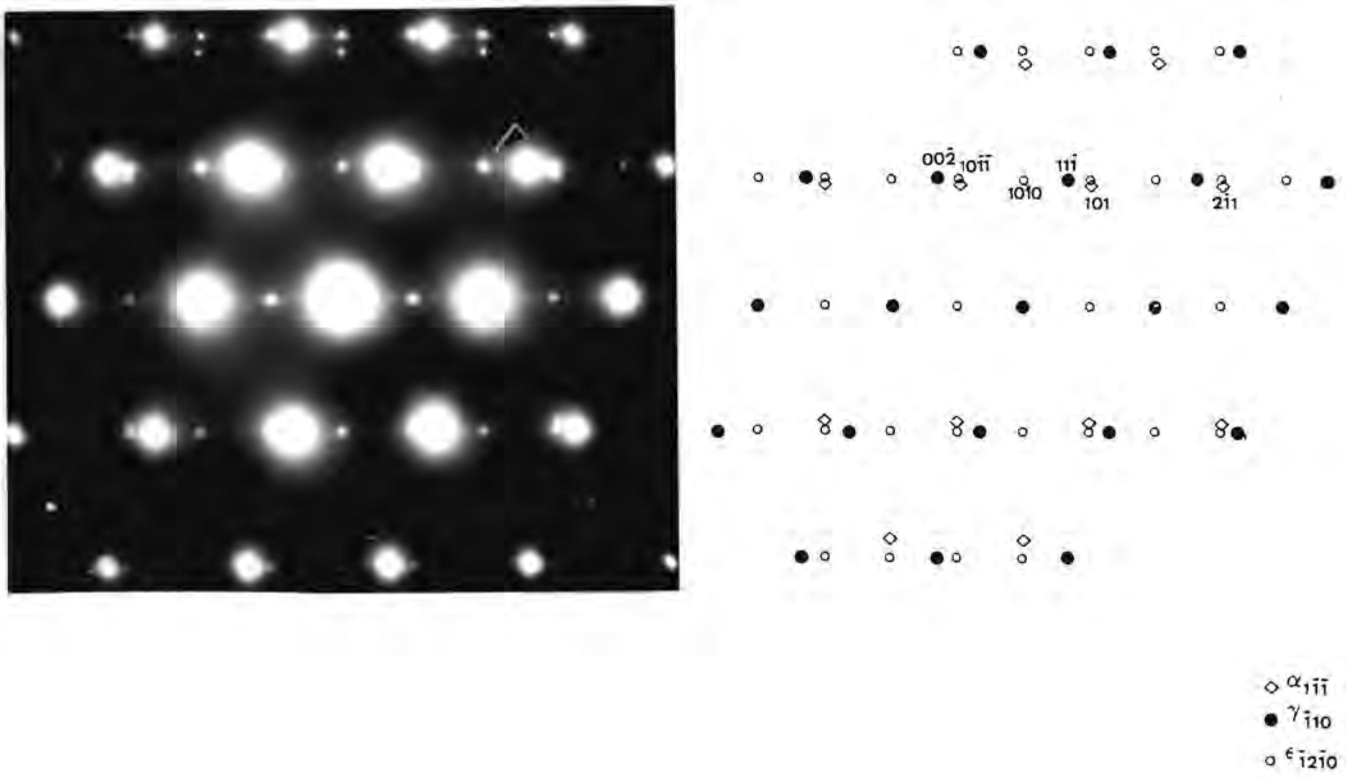

a) b)

Fig 59: a) The selected area diffraction pattern associated with ε-martensite and α'-martensite in an austenite matrix shown in Fig 60 showing the $[\bar{1}10]_\gamma$, $[\bar{1}2\bar{1}0]_\varepsilon$ and $[1\bar{1}\bar{1}]_{\alpha'}$ zone axes

b) The Schematic associated with a)

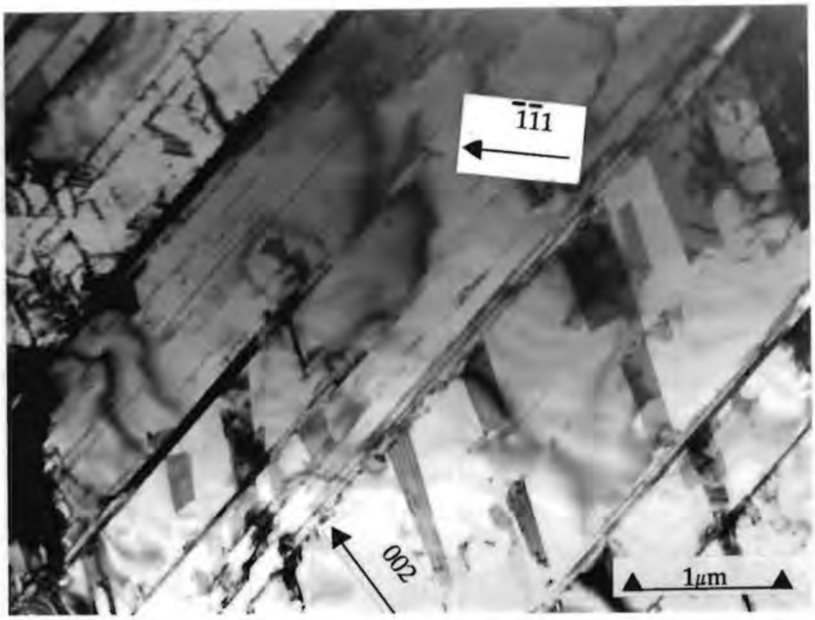

Fig 60: Bright field TEM micrograph of 0 wt% N alloy at 0.07 strain showing ϵ-martensite and α'-martensite in an austenite matrix

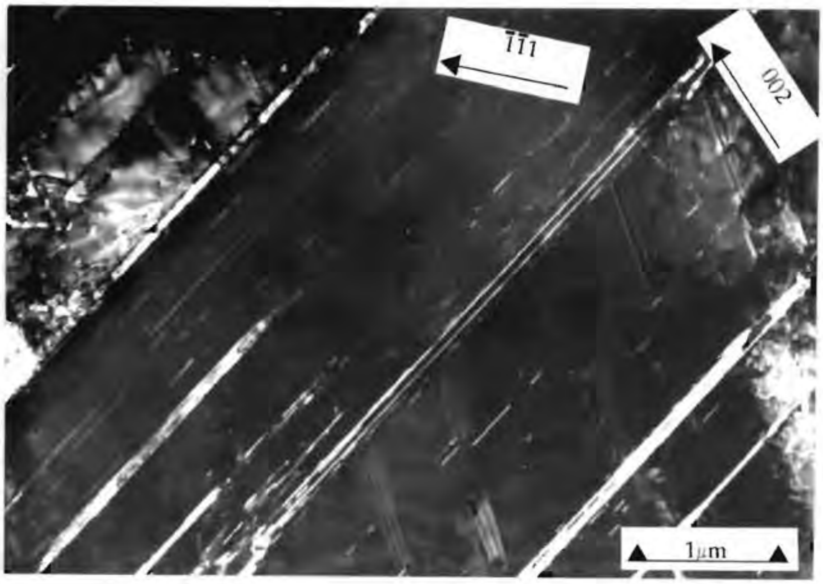

Fig 61: Dark field TEM micrograph of an ϵ-martensite reflection labelled in Fig 59 for a 0 wt% N alloy at 0.07 true strain showing ϵ-martensite in an austenite matrix

Selected area electron diffraction analysis of the undeformed alloy containing thermally induced martensite, also revealed the presence of two α'-martensite austenite orientation relationships as well as the presence of ϵ-martensite within the same selected area. This very complex electron diffraction pattern showing both the Kurdjumov-Sachs (K-S) and N-W orientation relationships is shown in Fig 62. The associated bright-field image in Fig 63 shows two laths of martensite within an austenite matrix.

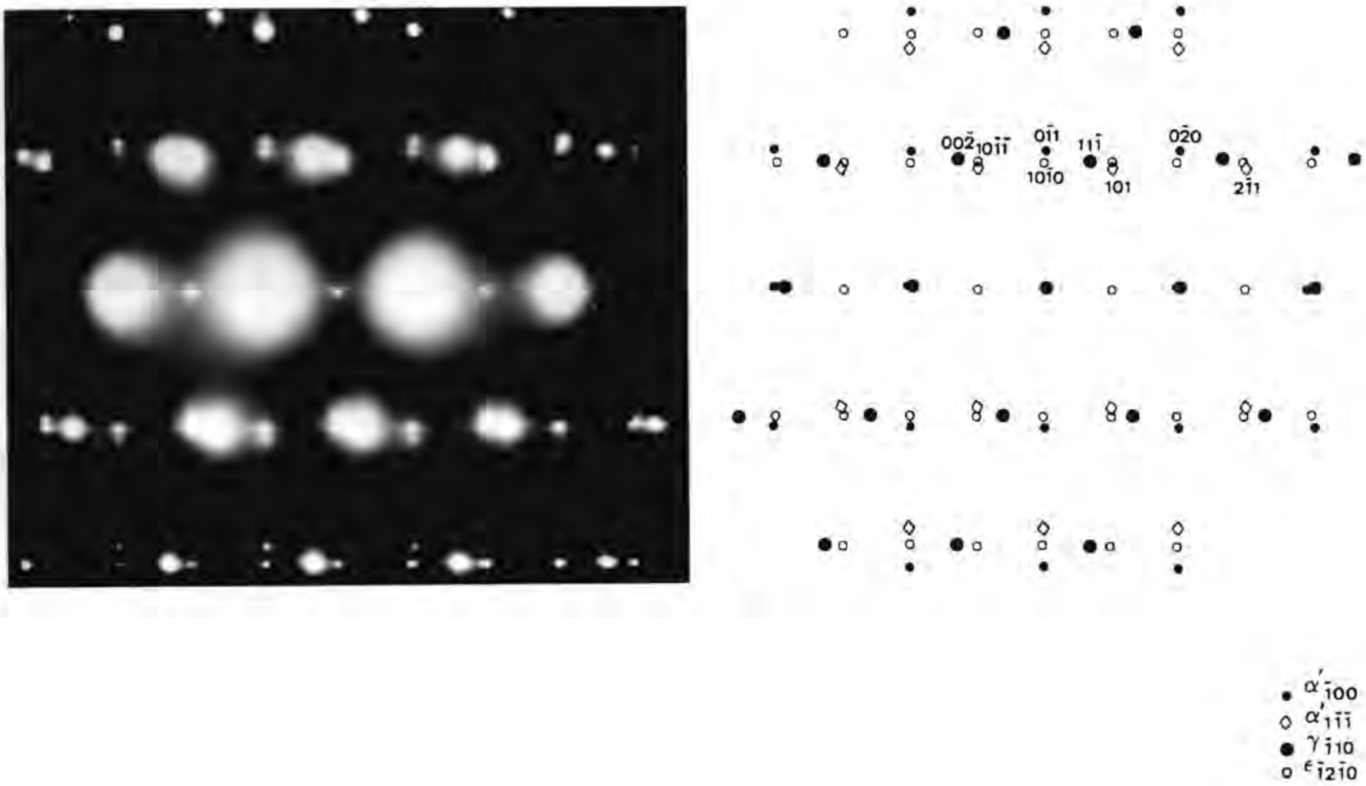

a)

b)

Fig 62: a) The selected area diffraction pattern associated with ϵ-martensite in an austenite matrix shown in fig 63 showing the $[\bar{1}10]_\gamma$, $[\bar{1}2\bar{1}0]_\epsilon$, $[\bar{1}00]_{\alpha'}$ and $[1\bar{1}\bar{1}]_{\alpha'}$ zone axes

b) The schematic for a)

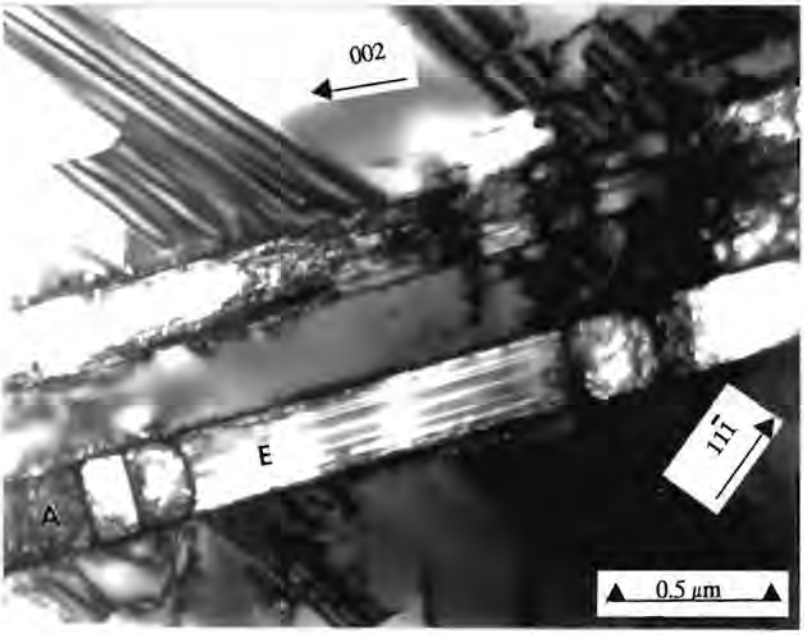

Fig 63: Bright field TEM micrograph of an annealed 0 wt% N alloy showing ϵ-martensite and α'-martensite in an austenite matrix

The α'-martensite reflections were more difficult to image in dark field in view of the fact that they are always closely associated with a ϵ-martensite reflection, but dark field techniques suggest that the top lath predominantly obeys the K-S orientation relationship while the bottom lath is generally associated with the N-W relationship. Thermally- and strain-induced martensite were observed to be indistinguishable in this alloy system.

Fig 64 shows what appears to be the formation of α'-martensite at the intersection of shear bands. This observation is consistent with the nucleation hypothesis of strain-induced martensite proposed by Olsen and Cohen [27,28].

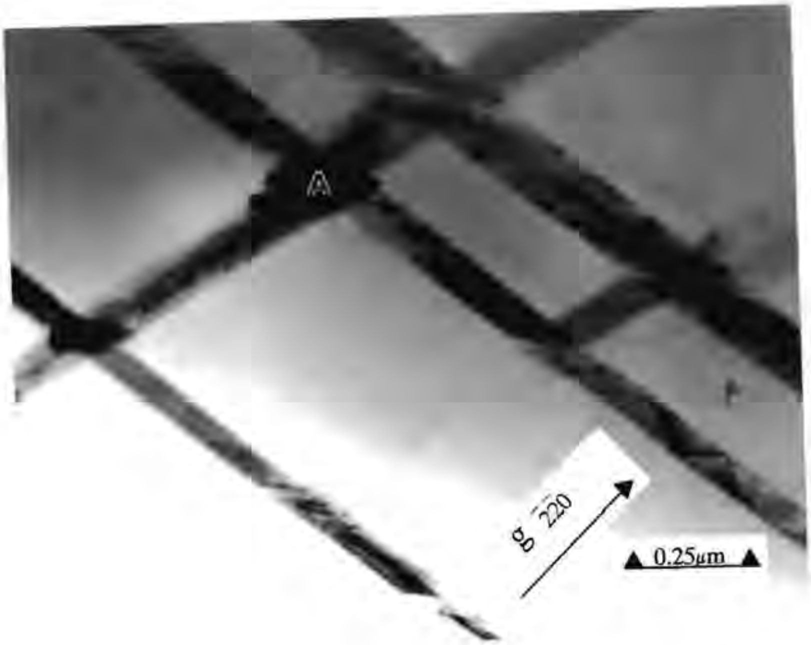

Fig 64: Bright field TEM micrograph of 0 wt% N alloy at 0.07 true strain showing nucleation of martensite at shear band intersections in an austenite matrix

c) The evolution of microstructure with deformation

In the undeformed alloys, the microstructures are essentially strain-free but contain stacking faults and dislocations as illustrated in Figs 50 and 51. As the strain increases the densities of stacking faults and dislocations multiply (Fig 65). The dislocations exhibit a planar glide mode. Twinning occurs with greater frequency at larger strains and the microstructures become more dense (Figs 66 a and b). Planar glide is the dominant mechanism at low strains while mechanical twinning becomes more important at high strains. ϵ-martensite was observed at low strains, disappearing at higher strains whereas α'-martensite increased with strain level. As the nitrogen content increases, the strains at which α'- and ϵ-martensites were initially observed became greater. From the microstructure of the 0.27 wt% nitrogen alloy at 0.30 strain (Fig 67), it is evident from selected area diffraction pattern analysis, that although a dense dislocation network can be observed, no martensite is apparent in this particular field of view. In contrast Fig 68 shows a 0 wt% nitrogen alloy at about 0.28 true strain which has undergone a strain-induced transformation of austenite to martensite and the microstructure shows a heavily dislocated martensite lath. The entire microstructure became too densely dislocated to observe much detail at very high strains. It was difficult to obtain clear diffraction patterns from the highly strained specimens because foil regions which were sufficiently thin exhibited local bending due to the high dislocation density and strain-induced martensite.

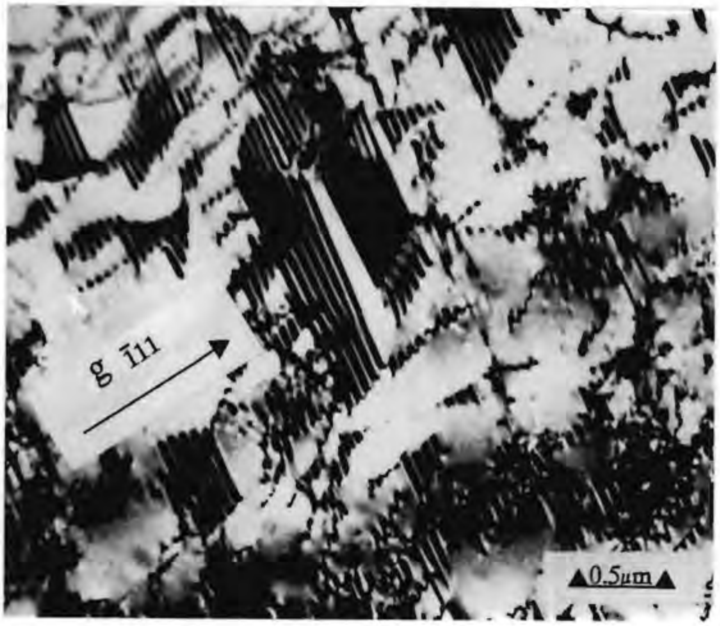

Fig 65: Bright field TEM showing high density of dislocations and stacking faults in the 0 wt% nitrogen steel at about 0.07 true strain

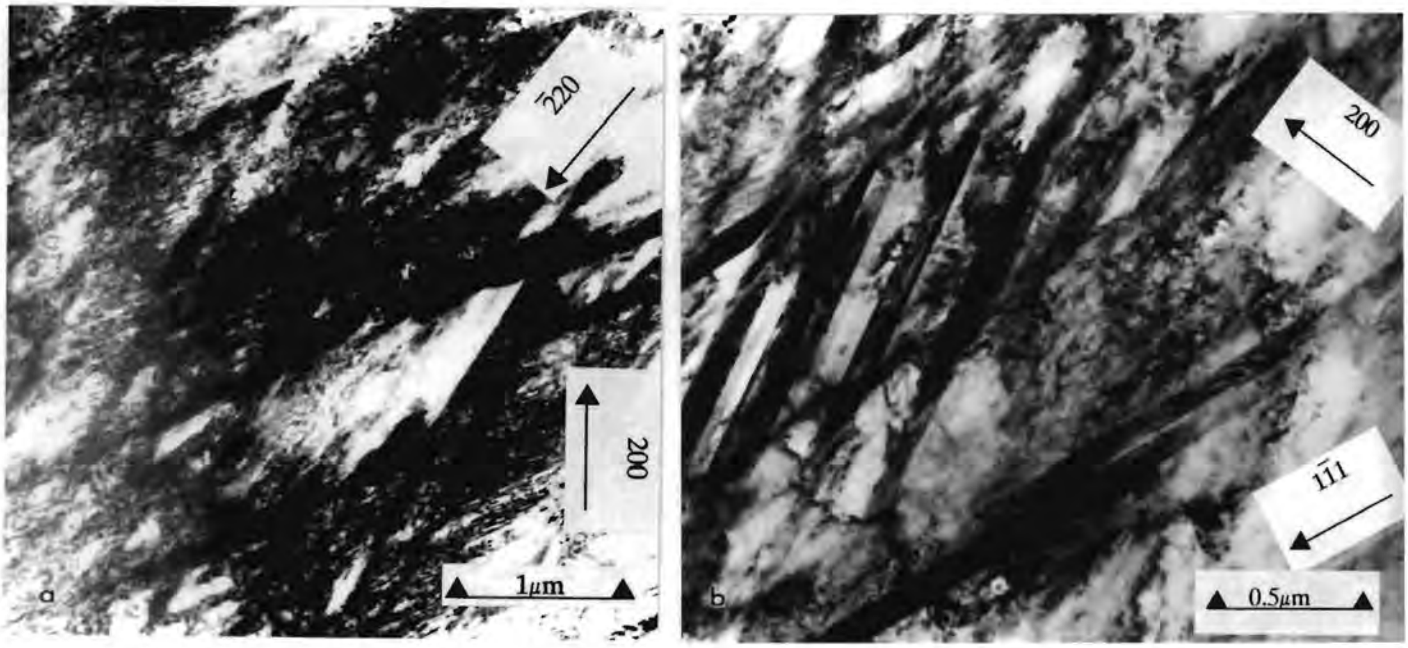

Fig 66 a) and b): Bright field TEM showing high density of dislocations, stacking faults and twins in the 0.27 wt% nitrogen steel at about 0.20 true strain

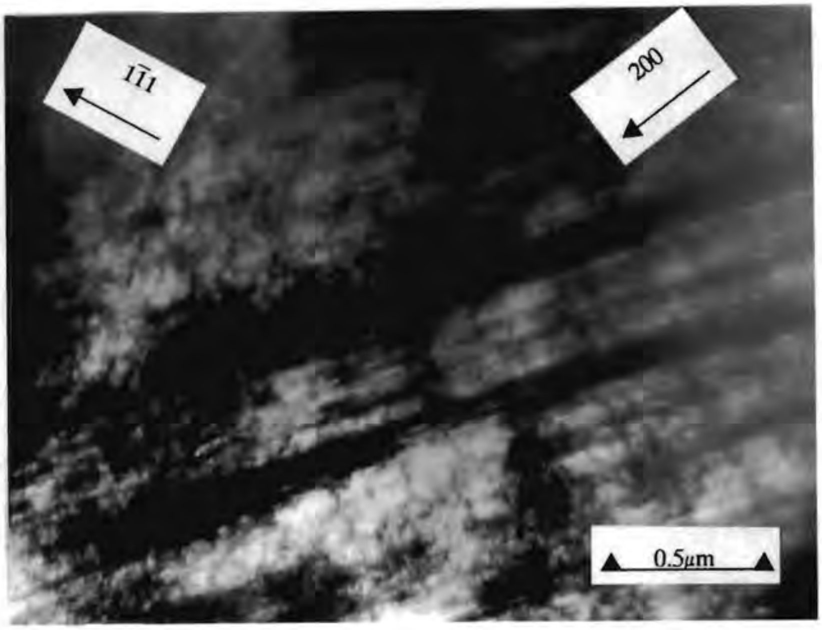

Fig 67: Bright field TEM showing very dense microstructure in the 0.27 wt% nitrogen steel at about 0.30 true strain

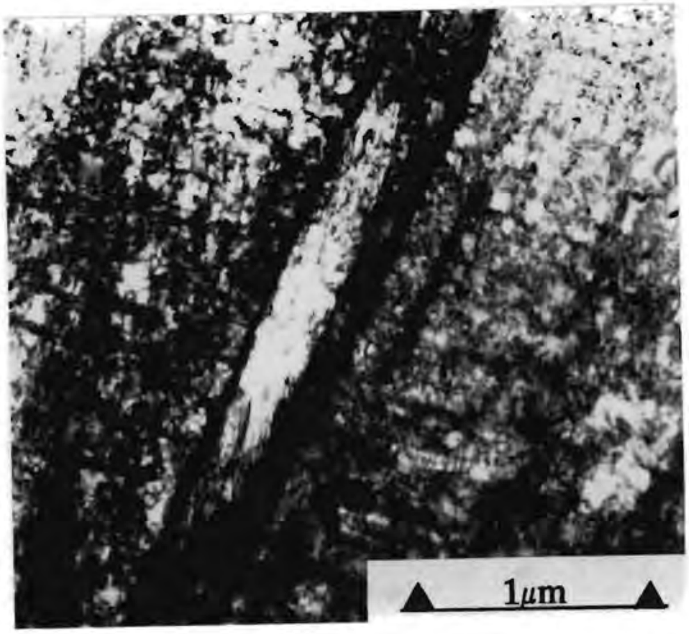

Fig 68: Bright field TEM showing α'-martensite lath in highly dislocated region in the 0 wt% nitrogen steel at about 0.28 true strain

d) The Effect of Nitrogen on the Planarity of Glide.

A qualitative assessment of the microstructures at 0.07 true strain suggests that as the nitrogen content increases, the planarity of the glide decreases. This result is confirmed by examinations of the microstructures at 0.20 and 0.30 true strain. The spacing between the crisscrossing active planes tended to increase as the nitrogen content increased, implying that the sharpness of planarity decreases. Two images from each of the 0 wt%, 0.13 wt% and 0.27 wt% nitrogen alloys at 0.07 true strain are shown in Figs 69, 70 and 71, respectively which supports this observation although obviously a much larger field of view has been examined.

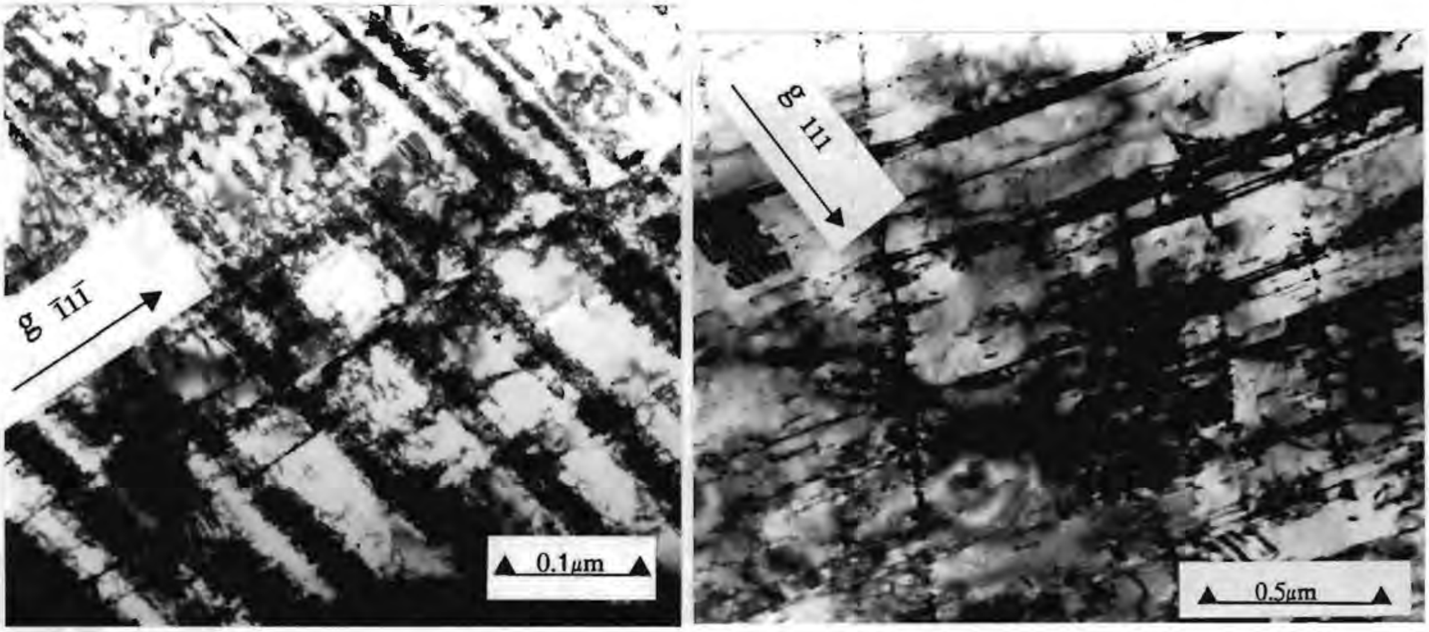

Fig 69: Bright field TEM's showing a planar dislocation glide mode in the 0.wt% nitrogen alloy after 0.07 true strain in an austenite matrix

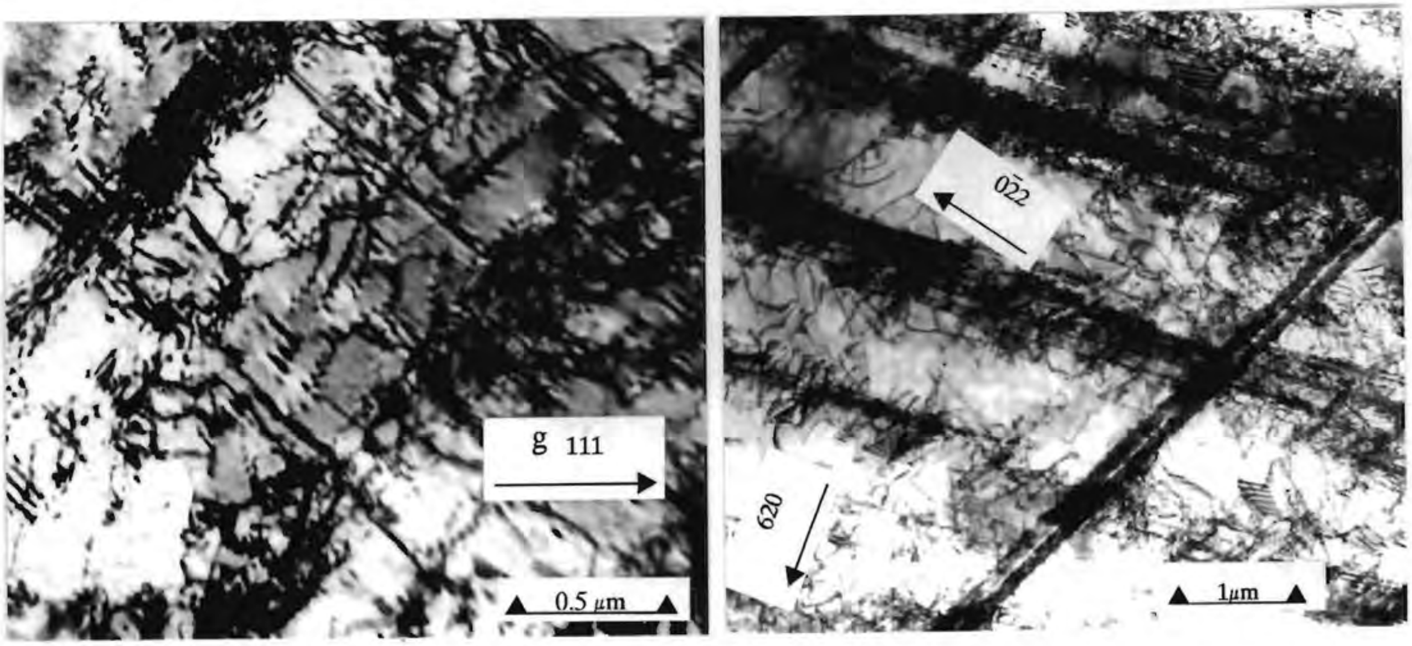

Fig 70: Bright field TEM's showing a planar dislocation glide mode in the 0.13 wt% nitrogen alloy after 0.07 true strain in an austenite matrix

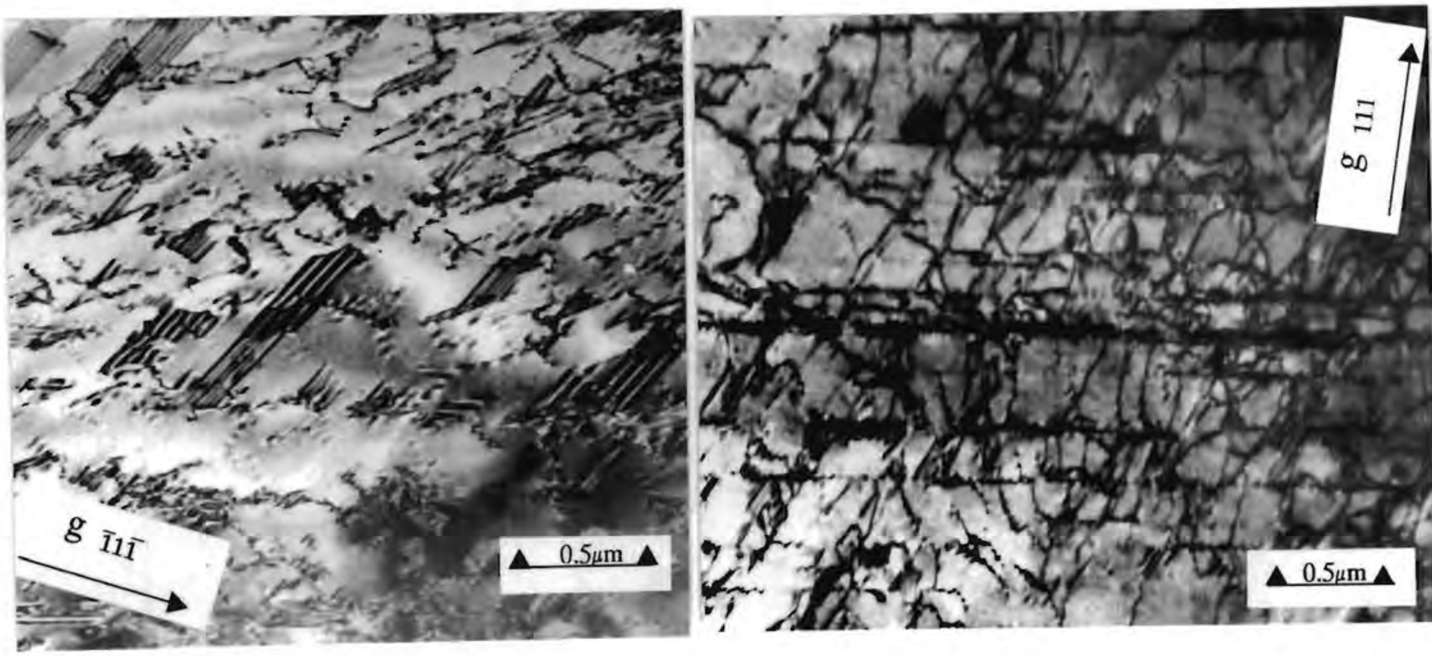

Fig 71: Bright field TEM's showing a diminished planar dislocation glide mode in the 0.27 wt% nitrogen alloy after 0.07 true strain in an austenite matrix

4.4.3 The presence of carbides or nitrides

Transmission electron microscopy examinations did not reveal the presence of additional reflections in the selected area electron diffraction patterns, due to the presence of carbides or nitrides. It is therefore concluded that the nitrogen and carbon contents of this alloy range are sufficiently low, to prevent the formation of either carbides or nitrides after solution treatment.

CHAPTER 5

DISCUSSION

5.1 CHARACTERISTICS OF THE ANNEALED MICROSTRUCTURES

Austenite stability is predominantly affected by composition and temperature. Although the experimental alloys investigated are predominantly austenitic in the annealed condition, the 0 wt% nitrogen steel contains about 11 vol% δ-ferrite and the 0.047 wt% nitrogen steel contains about 5 vol% δ-ferrite. As the nitrogen content increases, the austenite forming potential increases, and the propensity for the formation of δ-ferrite at the annealing temperature decreases. The annealed steels containing at least 0.1 wt% nitrogen thus consist of predominantly austenitic microstructures with less than 1 wt% δ-ferrite present. A small amount of δ-ferrite can be beneficial as it dissolves impurities thus lowering the concentration of impurities. Undissolved impurities create additional interfacial area and lead to intergranular cracking [87]. However, δ-ferrite is generally undesirable because it is reported to have an adverse effect on the hot workability of alloys [24]. An increase in nitrogen content, also produces an increase in austenite stability. The lack of nitrogen in the 0 wt% nitrogen alloy produces such a low austenite stability, that a transformation from austenite to martensite is invoked upon quenching this alloy to room temperature. This 0 wt% nitrogen steel thus contains 10-16 vol% martensite, in addition to δ-ferrite, after quenching to room temperature. The presence of these second phases leads to additional strengthening processes, such as compositional strengthening.

The extensive presence of annealing twins in the undeformed microstructure, is a consequence of the low SFE of this alloy range. A qualitative transmission electron microscopy (TEM) investigation of stacking fault densities in the undeformed structures, suggests that the SFE increases with increasing nitrogen content. Although additions of nitrogen have been reported by other workers [56,57] to cause a decrease in SFE, these changes were observed in fully stable steels. The observed increase in SFE with nitrogen content for the experimental alloys is not unexpected, if the results of Fujikura et al [53] are considered, where it has been shown that for low nitrogen regions, increasing nitrogen content causes an increase in SFE, even though in high nitrogen regions, increasing the nitrogen content results in a decrease in SFE. These trends are a consequence of the variation of austenite stability with nitrogen content and in this particular alloy range, the austenite has not been sufficiently stabilised and hence an increase in SFE with nitrogen content is observed.

Transmission electron microscopy (TEM) examinations of annealed microstructures revealed that there are no nitrides present throughout this alloy range. Nitrides are undesirable as they increase the corrosion potential. The absence of nitrides in these manganese containing steels, after a solution treatment at 1050 °C, is not unexpected since manganese promotes nitrogen solubility.

5.2 THE DEFORMATION BEHAVIOUR OF THESE STEELS

5.2.1 The Variation in Yield and Ultimate Tensile Strengths

At nitrogen contents greater than 0.1 wt% the yield strength at room temperature increases with nitrogen content (Fig 35) and the dominant strengthening mechanisms would appear to be solid solution strengthening and Cottrell interactions. As the nitrogen content increases from 0 wt% to 0.1 wt% the yield strength decreases. As mentioned in the previous section, the 0.047 wt% nitrogen alloy contains about 5 vol% δ-ferrite and the 0 wt% nitrogen alloy contains 11 vol% δ-ferrite and 10-16 vol% martensite. These additional phases cause secondary phase hardening and since the presence of secondary phases diminishes with increasing nitrogen, the yield strength of the 0 wt% nitrogen alloy is expected to be higher than that of the 0.047 wt% nitrogen alloy. Although the increment in strength in the 0 wt% nitrogen alloy may also be accounted for by the presence of martensite as well as δ-ferrite prior to straining, it has been reported, see section 2.2.4, that the presence of 10-16 vol% martensite prior to straining can in fact decrease the yield strength. The presence of 11 vol% δ-ferrite in the 0 wt% nitrogen alloy has caused grain refinement and the smaller grain size of the 0% nitrogen alloy could also account for the increased yield strength of this alloy.

The influence of nitrogen on ultimate tensile strength (UTS) is very complex, as is apparent from Fig 34. It is anticipated, from the yield strength variations that solid solution strengthening and the Cottrell interaction play dominant roles in the strengthening behaviour of these steels. As discussed earlier, the presence of secondary phases prior to deformation (δ-ferrite and martensite) also promotes an increase in strength. In addition, the smaller grain size of the 0 wt% nitrogen alloy could also contribute to an increased strength in this alloy. The variation in UTS with nitrogen content does not show these trends; in fact, there appears to be no distinct trend in UTS with nitrogen, other than the 0.047 wt% nitrogen alloy exhibiting a higher UTS than any other alloy. To gain a more intuitive understanding of the UTS variations, the work hardening behaviour and evolution of microstructure of the alloys were examined.

The true stress / true strain curves observed at room temperature suggest that the low nitrogen alloys (less than 0.1 wt% nitrogen) undergo a deformation-induced transformation of austenite to martensite which provides considerable work hardening, as evidenced by the upward curvature in the tensile curves. The sigmoidal nature of the true stress / true strain curves and corresponding strengthening effect diminish as the nitrogen content increases and the austenite stability improves.

Examination of the evolved microstructures at various strain levels, utilising light microscopy, TEM and XRD, revealed that throughout this alloy range a deformation-induced phase transformation from austenite to martensite occurs. In the 0 wt% nitrogen alloy an extensive deformation-induced transformation occurs whereas the 0.27 wt% nitrogen steel only initiates a transformation between 0.30 true strain and the fracture strain. Thus, as the nitrogen content increases the amount of transformation-induced martensite decreases (Fig 32 and 33) and the strain at which it initially forms increases. This is a reflection of the pronounced effect of nitrogen on the austenite stability within this alloy range. TEM investigations and XRD reveal the extensive presence of ε-martensite at low strains in the low nitrogen steels (0 to 0.1 wt%). The ε-martensite (hcp) was usually aligned with stacking faults. This is not unexpected as the passage of two Schockley partials on every second close packed plane of an fcc matrix creates a stacking fault between the two partials, which consists of an hcp crystal structure. α'-Martensite was observed in TEM investigations to be closely associated with ε-martensite. The disappearance of ε-martensite at higher strains, where the volume fraction of α'-martensite increases monotonically with strain (Fig 33), suggests that the kinetics are similar to that shown in Fig 8 (page 16) and that ε-martensite is an intermediate in the formation of α'-martensite in this alloy range. As the nitrogen content increased, ε-martensite was observed to a lesser degree. It is postulated that this could be a consequence of the increasing SFE or that insufficient intermediate strain-levels were examined in the higher nitrogen alloys. The presence of ε-martensite in this alloy range is not unusual as the alloys generally have a low SFE.

The orientation relationship between austenite and ε-martensite was found to be $[110]_{fcc}//[1210]_{hcp}$ and is the same as that observed by other workers [88]. The orientation relationship between austenite and α'-martensite is not singular in this alloy range as both the Nishiyama-Wasserman (N-W) and Kurdjumov-Sachs (K-S) relationships were observed in the annealed 0 wt% nitrogen alloy, within adjacent laths in the same martensite packet. The observation that a single relationship does not always exist within an alloy, has been reported by other investigators [3] in other steel systems. Rama Rao et al [3] account for this as increasing the variants available during the nucleation stages and thus allowing greater flexibility. The orientation relationships are composition dependent, and increasing the manganese and nickel contents promotes the N-W relationship. The 0 wt% nitrogen alloy clearly has an intermediate concentration of elements where neither the N-W nor K-S orientation relationship is dominant. The thermally- and strain-induced martensite phases in the 0 wt% nitrogen steel were indistinguishable, which is also a consequence of the alloy chemistry. Caution must be exercised as the possibility does exist that these low angle zone axes are in fact not parallel, but a few degrees apart. The implications of the formation of strain-induced martensite on the strengthening and work hardening of steels are extremely important.

For a stable austenitic steel the work hardening rate (WHR) decreases parabolically with increasing strain , as is the case at 0.27 wt% nitrogen (Fig 24). Analysis of the work hardening rate behaviour shows that as the nitrogen content of this alloy range decreases, the WHR deviates increasingly from that observed for a stable steel. In the extreme case at 0 wt% nitrogen (Fig 25), at low strains the WHR decreases to below that of the stable steel. Further increases in strain produce an increase in WHR which reaches a peak (Fig 25), after which WHR diminishes with ensuing strain. This minimum in WHR at low strain values is associated with the strain-induced formation of 13 vol% martensite in the 0 wt% nitrogen steel and 7 vol% martensite in the 0.047 wt% nitrogen steel. There is reduction in WHR to below that of a stable steel because the formation of martensite operates as a deformation mechanism. The deformation arises from a strain contribution which is generated by the volume changes that manifest when austenite transforms to martensite. This additional strain contribution causes dynamic "transformation softening". The minimum in WHR was not observed in the higher nitrogen steels where the rate of transformation is probably insufficient to enable the transformation to operate as a deformation mechanism. The subsequent increase in WHR after the minimum, can be associated with the "static hardening" of the deformation-induced martensite. In the 0 wt% nitrogen steel, the volume fraction of strain-induced martensite that has formed just after the WHR peak is 51 vol% (the total volume fraction of martensite at this strain, is about 64 vol%), whereas for the 0.047 wt% nitrogen alloy, 45 vol% strain-induced martensite has formed just before the peak. Peak heights diminish, while the strain at which the peak is observed increases, as the nitrogen content is raised. The peaks become less pronounced as the nitrogen content increases, although the WHR is nevertheless still greater than that of a stable steel. As the martensite content reaches about 50 vol% in these steels, the WHR declines, due to the fact that the bulk of the deformation is taken on by the martensite phase. As the nitrogen content increases, a diminished contribution to the strength, can be expected from the formation of deformation-induced martensite, and this is illustrated in the work hardening rate (WHR) curves (Fig 24 to 30). Work hardening can also occur as a consequence of the inhibition of cross-slip which is attributed to a low stacking fault energy (SFE). The microstructures have to be examined at different levels of deformation to establish whether SFE is contributing to the work hardening of the steels.

Investigations of deformed microstructures, utilising transmission electron microscopy (TEM), revealed that as deformation increased, the dislocation and stacking fault density increased. TEM investigations indicated that the dominant deformation mechanisms are planar glide and deformation twinning. Once again this is not surprising in view of the low stacking fault energy (SFE) of these alloys. TEM observations suggest that the planarity of glide becomes more dominant and sharper as the nitrogen content decreases. These changes lead to additional strengthening effects as the nitrogen content decreases, since more dislocations have to be activated; more dislocation barriers are formed and the efficiency of the barriers is enhanced. The changes in planarity are a reflection of the changes in SFE with nitrogen content, predicted from the TEM observations of stacking faults in the undeformed alloys. These planarity changes validate the fact that the increase in SFE with nitrogen content is influencing the deformation behaviour thereby causing a decreased contribution to work hardening as the nitrogen content increases. The increase in SFE with nitrogen content also reduces the ease of nucleation of martensite. At larger strains and lower nitrogen contents deformation twinning was observed to a greater degree and also contributed to the work hardening of the alloys.

The inhibition of cross-slip (due to the low SFE) and the formation of strain-induced martensite are both major contributors to the work hardening behaviour of these alloys at room temperature, and it has been shown that there is ample experimental evidence to support that these strengthening mechanisms are contributing to the deformation behaviour of this alloy range. Although an increased strengthening with increased nitrogen contents, on the basis of solid solution strengthening, is anticipated and the room temperature yield strength variations for higher nitrogen contents (greater than 0.1 wt% nitrogen) do appear to suggest this, there is no direct evidence that solid solution strengthening and the Cottrell interaction are operating to a greater degree with increased nitrogen content in this alloy range. Elevated temperature tensile tests were conducted to establish whether nitrogen was generating a substantial contribution to solid solution strengthening.

Tensile tests were conducted at 120°C which simplifies the factors contributing to the strengthening behaviour. In this alloy range, at 120° C, the likelihood of martensite forming during tensile testing is minimal as this testing temperature was selected to be above the M_d temperatures of the alloys. The tensile tests and work hardening rate (WHR) results established that no strain-induced martensite formed at this temperature. SFE has been reported to be temperature dependent and examination of Fig 10 shows that it is highly probable that the SFE at 120°C (393K) is considerably higher than that at 20°C (293K). When the SFE of an alloy is high, dislocations will not split readily into partials and cross-slip will not be significantly inhibited. Thus for alloys with high SFE, any changes in SFE with nitrogen content will not alter the work hardening behaviour considerably since SFE is not contributing significantly to the work hardening processes. The effects of grain size are also diminished at higher temperatures and although the 0 wt% nitrogen alloy has been noted as having a much smaller grain size than the nitrogen alloys, an associated strengthening contribution on the basis of grain size, may not necessarily be observed in this alloy. The major mechanisms which should dominate at this temperature are solid solution strengthening, Cottrell interactions and the presence of second phases (δ-ferrite and martensite) prior to straining. A schematic illustrating the interaction of mechanisms is shown in Fig 72.

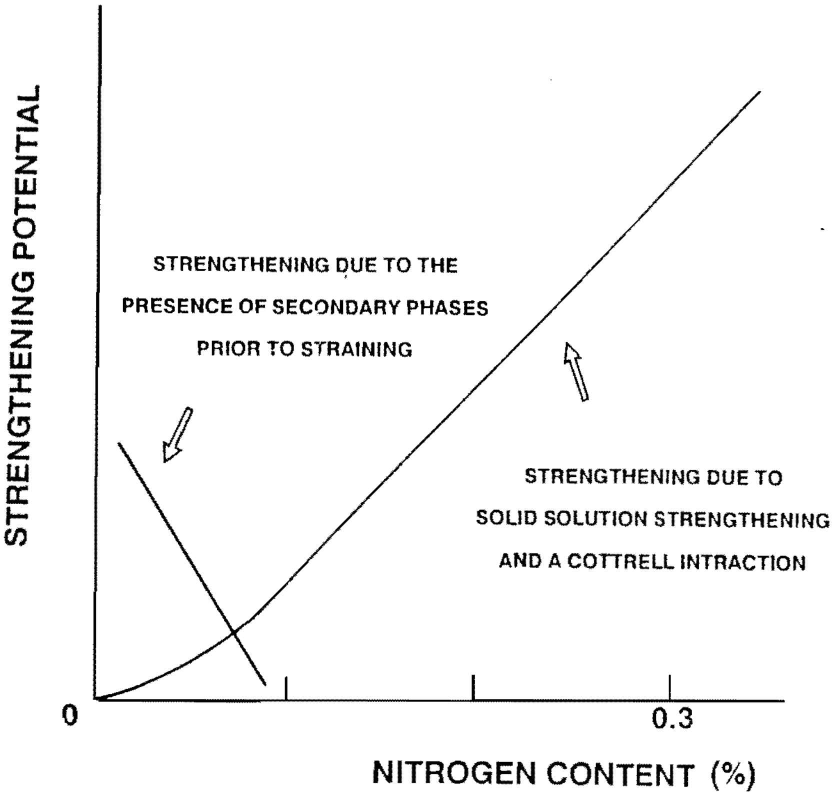

Fig 72: Schematic diagram showing strengthening mechanisms operating at 120°C

Examination of the changes in yield strength with nitrogen content, demonstrate that as the nitrogen content increases, the yield strength increases. This result can be attributed to solid solution strengthening and a Cottrell interaction (Fig 72). Although the 0 wt% nitrogen alloy contains martensite and δ-ferrite whilst the 0.047 wt% nitrogen steel contains δ-ferrite in the annealed state, these secondary phases do not appear to be contributing to the strength of the steels. A strengthening contribution from the presence of secondary phases would be anticipated as secondary phases have been noted as contributing to the room temperature yield strength. However, since the elevated temperature test results are only on the basis of one test in most instances, the presence of secondary phases may still be contributing to the deformation behaviour, but the trends are not clear.

Unlike yield strength, the tensile strength is a reflection of the work hardening processes that are occurring within the alloy. At the elevated temperature (120°C) it is assumed that the main contribution to strengthening is from solid solution strengthening and a Cottrell interaction. TEM has qualitatively established that SFE increases with increasing nitrogen content in this alloy range. SFE however, increases with temperature, and cross-slip is less likely to be inhibited, even for the low nitrogen alloys at 120°C, as the SFE is too high. If SFE was contributing significantly to the work hardening process, the strengthening effects would be diminishing with increasing nitrogen content. The true stress / true strain curves of all the alloys at high temperature (120°C) are parabolic in shape, suggesting that there is no increased strengthening due to a strain-induced phase transformation to martensite. All the alloys show a gradual decline in WHR with increasing strain, typical of the deformation of austenite. There is no apparent change in WHR behaviour with nitrogen content at elevated temperatures. The absence of deformation-induced martensite during straining at 120°C eliminates any strengthening contributions from this phenomena. The results show that the UTS is increasing with nitrogen content and do not suggest that SFE is playing a dominant role at this temperature. The elevated temperature results thus provide evidence that the additions of nitrogen are generating solid solution strengthening and Cottrell interactions across this alloy system.

At low nitrogen contents (0 wt% to 0.13 wt%) the dominant strengthening mechanisms at room temperature have been shown to be the formation of strain-induced martensite and the restriction of cross-slip due to a decreased SFE as is illustrated in Fig 73. As the nitrogen content is increased, the SFE increases and cross-slip becomes less inhibited. The increase in SFE also reduces the propensity for the nucleation of martensite. At high nitrogen values (0.13 wt% to 0.27 wt%) however, contributions from solid solution strengthening and the Cottrell interaction have been shown to dominate and these strengthening contributions increase as the nitrogen content is raised (Fig 73). As the nitrogen content changes there is thus a play-off between these mechanisms and no distinct trend with nitrogen content is observed, as the competing mechanisms mask each other which is illustrated schematically in Fig 73. The 0.047 wt% nitrogen steel has a higher UTS, probably due to the fact that it is not the amount of martensite present but the strength of it that is crucial. Although less martensite forms in the 0.047 wt% nitrogen steel, the martensite is interstitially hardened (by the nitrogen) to a greater extent and this alloy is thus stronger than the 0 wt% nitrogen alloy. At higher nitrogen contents there is inadequate formation of martensite and therefore even though the martensite is stronger, it does not significantly contribute to the strengthening behaviour.

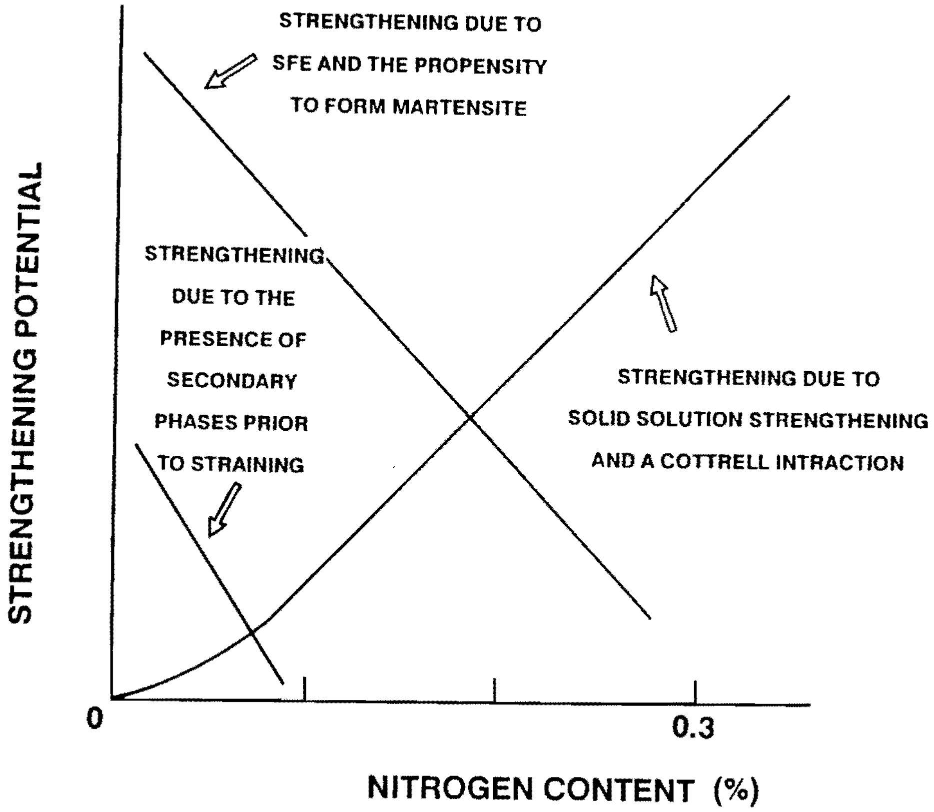

Fig 73: Schematic diagram showing the strengthening mechanisms operating at room temperature (20°C)

5.2.2 Ductility

There is ample evidence that the alloys are undergoing a transformation to martensite during straining. This strain-induced transformation can cause an increase in strength and elongation simultaneously, if martensite forms in the regions of incipient necking, preventing necking and thus enhancing elongation. The room temperature results do not show a pronounced TRIP (Transformation Induced Plasticity) effect. If intermediate nitrogen contents were tested where the rate of formation of martensite was optimal, a significantly enhanced elongation accompanying a high strength level may be observed. On the other hand, the rate of increase of martensite formation with deformation should be sigmoidal in shape to facilitate TRIP, in that the formation of martensite should be gradual initially until incipient necking occurs, where the rate of transformation should be more rapid. It is postulated that since the volume fraction of martensite forming as a function of strain is virtually linear in this system (Fig 33), the kinetics of the martensite transformation within this alloy range do not facilitate TRIP. The 0 wt% nitrogen steel has a significantly lower maximum uniform elongation (MUE) than the other alloys and this can be easily understood, since during room temperature testing the 0 wt% nitrogen steel has undergone a substantial transformation from austenite to martensite before the strain level at which the MUE is measured. Martensite, although stronger than austenite, is less ductile and the overall observed ductility is that of a more brittle martensite phase.

At 120°C, the tensile results indicate an increase in maximum uniform elongation (MUE) with nitrogen content up to 0.1 wt% nitrogen after which nitrogen does not appear to be having an effect. Since the scatter at 0.27 wt% nitrogen (where three tests were conducted) is almost within the same deviation as the difference between the 0.1 wt% nitrogen steel and the other alloys, it is probable that nitrogen is having little effect on the MUE values of the alloys at 120°C.

5.3 VARIATIONS IN HARDNESS WITH NITROGEN CONTENT AND DEFORMATION

5.3.1 The Effect of Nitrogen on Hardness and Microhardness

As the nitrogen content increases, the amount of martensite decreases and since the hardness and microhardness of the martensite phase is significantly greater than that of the austenite phase, a large decrease in hardness is observed as the nitrogen content is increased from 0 wt% to 0.13 wt%. The decrease in hardness with increasing nitrogen, can also be accounted for by the observed increase in stacking fault energy and thus diminishing inhibition of cross-slip. In the higher nitrogen steels (greater than 0.13 wt% nitrogen) solid solution strengthening dominates and prompts an increase in hardness and microhardness with increasing nitrogen content.

5.3.2 The Variation of Hardness with Cold Work

Cold working resulted in increased strengths in all of the alloys. The propensity to form martensite during deformation is lower for a compressional load than a tensile load [50,51]. This restricts a direct comparison between tensile results and cold working behaviour (since cold working applies a compressional load). The fact that the transformation is prolonged should enhance the effects of the transformation at higher levels of cold work. Regardless of the change in the slope (of the microhardness versus cold work graphs) with nitrogen content (Fig 41), the variation of microhardness with cold work is not being significantly affected by nitrogen content. Although it was anticipated that the influence of nitrogen on the variation of microhardness with cold work, would imitate the changes in the true stress / true strain curves as the nitrogen content was altered, this is not observed. The surfaces of the specimens contained a scale which had to be removed electrochemically and this resulted in a less even surface than might have been obtained through mechanical polishing. The latter polishing technique could not be used because it would have induced a transformation to martensite. The sensitivity of the microhardness measurements may have been impaired by surface finish as well as the fact that any variance in microhardness is limited to the narrow range consisting of the difference in microhardness between austenite and martensite, and this could account for the fact that no distinctive behaviour was observed.

5.4 THE EFFECT OF NITROGEN ON FORMABILITY (ERICHSEN CUPPING TEST)

The formability was investigated by an Erichsen cupping test which measured the depth of indentation and is an indication of stretchability. Since, as has been stated in section 2.6, the stretch forming capabilities of metastable austenitic steels are reported to be superior to stable steels [75,24], it was anticipated that a variation in indentation depth with nitrogen would be observed. The indentation depth increases as the nitrogen is raised to 0.047 wt% after which no significant variation with nitrogen content is observed. The Erichsen test applies biaxial stresses which promote the transformation to martensite to a larger degree in comparison to uniaxial stresses. Nitrogen has been observed to have no distinct influence on UTS although nitrogen is changing the work hardening behaviour. As the effect of strengthening mechanisms such as deformation-induced martensite and the inhibition of cross-slip (due to a low SFE) diminishes, solid solution strengthening and the Cottrell interaction dominate and so the overall effects of nitrogen are masked. In the 0 wt% nitrogen alloy, a substantial transformation to martensite has occurred and the ductility is much lower than the rest of the alloys. This accounts for the lower formability of the 0 wt% alloy. The ductility of the nitrogen containing alloys does not vary significantly with increases in nitrogen content and it is therefore not unexpected on the basis of ductility variations, that the formability of the nitrogen containing alloys is not significantly altered. A direct comparison between strength and ductility on the basis of tensile tests usually gives the best indication of the formability of the steels.

5.5 EFFECT OF CARBON ON TENSILE PROPERTIES

As the carbon content was increased to 0.08 wt% a suppression of the deformation-induced transformation to martensite is observed. The effect of increasing the carbon content on the deformation-induced transformation, is qualitatively closely similar to increasing the nitrogen content. It is therefore not unexpected that the effect on work hardening behaviour of elevating the carbon content is observed to be analogous to increasing the nitrogen content of the alloys. The elevation in carbon content is observed to generate an increase in UTS, yield strength and ductility (MUE) at room temperature. The UTS and yield strength at 120°C, was observed to increase as the carbon content was raised, however carbon content showed no apparent influence on the ductility (MUE) of these steels at this elevated temperature. If as it appears the effects of carbon are analogous to nitrogen, then it is postulated that increasing the carbon content from 0.04 wt% to 0.08 wt% in the 0.1 wt% nitrogen alloy should produce an increase in SFE and an increased contribution from solid solution strengthening. As the carbon content is raised increases in microhardness and hardness at room temperature occur although no change in formability with carbon content, is apparent.

Increasing the carbon content is qualitatively equivalent to increasing the nitrogen content in terms of the influence carbon showed on the tensile properties. Carbon has the same effect as nitrogen in promoting austenite stability as carbon is also an austenite former and stabiliser. Thus, by altering the austenite stability by either changing the carbon or nitrogen contents, the operating strengthening mechanisms are adjusted and this produces corresponding changes in the deformation behaviour of the alloys.

5.6 SUMMARY

Light microscopy and XRD of the annealed microstructures revealed that the 0.047 wt% nitrogen alloy contains δ-ferrite and that the 0 wt% nitrogen alloy contains δ-ferrite and martensite. The presence of these secondary phases as well as the diminished grain size in the 0 wt% nitrogen alloy contribute to additional strengthening in these alloys. The UTS and yield strength variations at an elevated temperature (120°) support the fact that solid solution strengthening is occurring as the nitrogen content is increased. TEM investigations have shown that the SFE increases with increasing nitrogen content and there is thus a decreased contribution to work hardening with increasing nitrogen contents. XRD, light microscopy and TEM have quantified the formation of deformation-induced martensite which diminishes as the nitrogen content increases. The corresponding increment in strength thus decreases as the nitrogen content increases. The true stress / true strain curves and WHR curves support the postulation that there is a diminishing contribution to work hardening as the nitrogen content increases. As the nitrogen content is altered different strengthening processes have been shown to be activated to varying degrees resulting in no overall trend of UTS with nitrogen content. The variations in ductility and Erichsen cupping tests with nitrogen content support these observations.

CONCLUSIONS

1) The austenite forming and stabilising potential increases with nitrogen content in this alloy range. These steels containing 0.1 wt% or more nitrogen have austenitic microstructures. The amount of δ-ferrite present diminishes as the nitrogen content increases. The steels containing 0.047 wt% and 0 wt% nitrogen contain about 5 vol% and 11 vol% δ-ferrite respectively. In addition, the 0 wt% nitrogen steel contains 10-16 vol% martensite in the annealed state.

2) The steels are metastable at room temperature and exhibit a strain-induced transformation from austenite to martensite. This is observed to initiate at higher strains and to a decreasing degree, as the nitrogen content increases. This transformation occurs with ε-martensite as an intermediate stage and the orientation relationship is $[110]_{fcc}//[1210]_{hcp}$. The α'-martensite generally exhibits a Kurdjumov-Sachs (K-S) orientation relationship with the austenite in these alloys. Within the 0 wt% nitrogen alloy a single orientation relationship between austenite and α'-martensite was not observed. Both the Kurdjumov-Sachs (K-S) and Nishiyama-Wasserman (N-W) orientation relationships were observed in this steel within adjacent laths of martensite. Examinations of the evolving microstructure, a consideration of the true stress / true strain and work hardening rate curves suggest that strain-induced martensite is contributing to the work-hardening processes at room temperature deformation. These contributions decrease with increasing nitrogen content. During tensile testing at 120°C no strain-induced martensite forms and thus does not contribute to the strengthening processes.

3) A qualitative assessment of the annealed states suggests that stacking fault energy (SFE) increases with nitrogen content. TEM examinations of the evolving microstructures suggest that the planarity of glide decreases and becomes less sharp with an increase in nitrogen content. This results in a decreased restriction of cross-slip and decreased contribution of stacking fault energy to work hardening with increasing nitrogen content. During tensile testing at 120°C there is no observed strengthening contribution from the restriction of cross-slip to work hardening. SFE variations with nitrogen content are not

significant at 120°C and this is not unexpected as SFE is elevated at this temperature.

4) The effects of solid solution strengthening are more pronounced with increasing nitrogen content. The tensile and yield strengths at 120°C, show an increase in strengths with increasing nitrogen content which can be attributed to solid solution strengthening and the Cottrell interaction. For nitrogen contents of 0.1 wt% and greater the room temperature yield strength variations increase with nitrogen content and this can be attributed to solid solution strengthening and the Cottrell interaction. At room temperature the effect of solid solution strengthening on tensile strength is masked by competing strengthening mechanisms such as the strain-induced transformation to martensite and SFE.

5) Due to the competition between the above mentioned strengthening mechanisms, nitrogen is not observed to have any distinctive effects on the tensile strength at room temperature.

6) Cold working increases the strength of the alloys. The cold working behaviour of this alloy range does not appear to be significantly influenced by nitrogen content.

7) Within this alloy range nitrogen does not have a dominant influence on ductility or formability.

REFERENCES

1. HODGSON,P.D. AND JACKSON,R.,*Metals Forum,* **4(4)**, 192 (1981)
2. STANKO,J.S. AND WELLBELOVED,D., *"Manganese in Corrosion Resistant Steels", Samancor*, Private Bag 8186, Johannesburg 2000, S.A. (Jun)(1991)
3. RAMA RAO,P. AND KUTUMBARAO,V.V.,*Int.Mat.Rev.,* **34(2)**, 69, (1989)
4. WAYMAN,C.M. *in Physical Metallurgy* (eds R.W.Cahn and P.Haasen), *"Phase Transformations, non-diffusive"*, 1031, North-Holland, Amsterdam (1983)
5. SCHLENKER,B.R.,*"Introduction to Materials Science"*, John Wiley & Sons, Brisbane, 130 (1981)
6. HODGSON,P.D. AND JACKSON,R.,*Metals Forum,* **4(4)**, 192 (1981)
7. HONEYCOMBE,R.W.K., *"Steels-microstructure and properties"*,Edward Arnold Publishers. ed E.Arnold, London (1981)
8. MARSHALL, P.,*"Austenitic stainless steels-microstructure and mechanical properties"*, Elsevier Applied Science Publishers, London & New York, 27 (1984)
9. ROWLANDS,D.P.,*Sasda (The Southern Africa Stainless Steel Development Association)*, P.O. Box 3737, Randburg, 2125, S.A.
10. ESPY,R.H.,*Welding J.,"Weldability of nitrogen-strengthened stainless steels"*,Welding Research Supplement, 149s (May) (1982)
11. RAO, B.V.N., *Metall.Trans.,* **10A**, 645 (May) (1979)
12. EDINGTON,J.W.,*Monographs in Practical Electron Microscopy in Materials Science,* **4**, Philips Technical Library, Cambridge
13. JAHN,M.T.,FAN,C.M. AND WAN,C.M.,*J.Mater.Sci.,* **20**, 2757 (1985)
14. HARRIES,D.R., *Int.Conf.Mech.Behaviour and Nuclear Applications of Stainless Steels at Elevated Temperatures, Varese*, Metals Soc., London (May)(1981)
15. HOFFMAN,J.P. AND VICTOR,A.B.,*FWP Journal, (SA Inst.Weld.),* 5 (Nov) (1989)
16. LENEL,U.R. AND KNOTT,B.R.,*Metall.Trans.,* **18A**, 767, (May) (1987)
17. FANG,X.F. AND DAHL,W.,*Mater.Sci.& Eng.,* **A141**, 189 (1991)
18. ANGEL,T.,*J.Iron and Steel Inst.,* 165 (May) (1954)
19. PICKERING,F.B.,*"Physical Metallurgy and the Design of Steels"*,Applied Science Publishers, (1978)
20. OLSON,G.B. AND COHEN,M.,*J.Less-Common Met.,* **28**, 107 (1972)
21. ONODERA,H. AND TAMURA,I.,*Proc.US.Jap.Symp.,* Rensselaer Polytechnic Inst., Troy, NY, 24 (1979)

---

22. Olson,G.B. and Cohen,M.,*Metall.Trans.,* **7A**, 1915 (1976)
23. Maxwell,P.C.,Goldberg,A. and Shyne,J.C.,*Metall.Trans.,* **5**, 1305 (Jun) (1974)
24. Pickering,F.B.,*Int.Met.Rev.,"Metallurgical Evolution of Stainless Steel",* (Dec) (1976)
25. Fukase,Y.Ebato,K.,Okubo,N. and Murao,S.,*Trans.ISIJ,* **8**, 311 (1968)
26. Dash,J. and Otte,H.M.,*Acta Metall.,* **11**, 1169 (1963)
27. Olson,G.B. and Cohen,M.,*Metall.Trans.,* **7A**, 1897 (1976)
28. Olson,G.B. and Cohen,M.,*Metall.Trans.,* **7A**, 1905 (1976)
29. Lecroisey,F. and Pineau,A.,*Metall.Trans.,* **3**, 387 (Feb) (1972)
30. Nemirovsky,M.,Nemirovsky,Y.R. and Rudakov,A.A.,*Phys.Met.Metall.,* **52(5)**, 150 (1981)
31. Murr,L.E.,Staudhammer,K.P. and Hecker,S.S.,*Metall.Trans.,* **13A**, 627 (Apr) (1982)
32. Mangonon,P.L. and Thomas,G.,*Metall.Trans.,* **1**, 1577 (Jun) (1970)
33. Brooks,J.W.,Loretto,M.H. and Smallman,R.E.,*Acta metall.,* **27**, 1829 (1979)
34. Rickerby,D.G. and Piatti,G.,*Materials Sci.& Tech.,* **7**, 71 (Jan) (1991)
35. Werner,E.,*Mat.Sci.& Eng.,* **101A**, 93 (1988)
36. Irvine,K.J.,Gladman,T. and Pickering,F.B.,*J.Iron & Steel Inst.,* 379 (Jul) (1969)
37. Sandstrom,R. and Berqvist,H,*Scand.J.Metallurgy,* **6**, 156 (1977)
38. Huang,G.L.,Matlock,D.K. and Krauss,G.,*Metall.Trans,* **20A**,1239 (Jul) (1989)
39. Bressanelli,J.P. and Moskowitz,A.,*Trans.ASM,* **159**, 223 (1966)
40. Zackay,V.,Parker,E.R.,Fahr,D. and Busch,R.,*Trans.Amer.Soc.Met.,* 150 (1967)
41. Livitsanos,C.P. and Thomson,P.F.,*Mater.Sci & Eng.,* **30**, 93 (1977)
42. Rosen,A.,Kjer,T. and Jago,R.,*J.Mater.Sci.,* **7**, 870 (1972)
43. Sakuma,Y. , Matlock,D.K. and Krauss,G,*Metall.Trans.,* **23A**, 1233 (Apr) (1992)
44. Tomota,Y.,Strum,M. and Morris,J.W.,Jr,*Metall.Trans.,* **17A**, 537 (1986)
45. Olson,G.B. and Azrin,M.,*Met.Trans.,* **9A**, 713 (May) (1978)
46. Adler,p.H.,Olson,G.B. and Owen,W.S.,*Metall.Trans.,* **17A**, 1725 (Oct) (1986)
47. Guimaraes, J.R.C. and De Angelis,R.J., *Mater.Sci. & Eng.,* **13**, 109 (1974)
48. Lagneborg,R.,*Acta Metall.,* **12**, 823 (Jul) (1964)
49. Goodchild,D.,Roberts,W.T., and Wilson,D.V.,*Acta Metall.,* **18**, 1137 (Nov) (1970)
50. Goldberg,A. and Hoge,K.G.,*Mater.Sci.& Eng.,* **13**, 211 (1974)
51. Cina,B.,*J.Iron & Steel Inst.,* 406 (Aug) (1954)
52. Hecker,S.S.,Stout,M.G.,Staudhammer,K.P. amd Smith,J.L.,*Metall.Trans.,* **13A**, 619 (Apr) (1982)
53. Fujikura,M.,Takada,K. and Ishida,K.,*Trans.ISIJ,* **15**, 465 (1975)
54. Fawley,R.,Quader,M.A. and Dodd,R.A.,*Trans.Met.Soc.,AIME,* **242**, 771 (1968)
55. Douglass,D.L.,Thomas,G. and Roser,W.R.,*Corrosion*, **20**, 15t (1964)

56. Stolz,R.E. and Vander Stande,B.,*Metall.Trans.,* **11A**, 1033 (Jun) (1980)
57. Schramm,R.E. and Reed,R.P.,*Metall.Trans.,* **6A**, 1345 (Jul) (1975)
58. Neef,H.J.C.,*Roestevast staal,* **2**, 35 (Apr) (1989)
59. Neef,H.J.C.,*Roestevast staal,* **3**, 45 (Jun) (1989)
60. Speidel,M.O.,*Proc.HiNit.Steels,Inst.Metals,Lille,France,* **92** (May) (1988)
61. Luwigson,D.C. and Berger,J.A.,*J.Iron & Steel Inst.,* 413 (Jan) (1969)
62. Tamura,I.,Maki,T. and Hato,H.,*Trans.ISIJ,* **10** 163 (1970)
63. Chanani , G.R.,Zackay,V.F. and Parker,E.R.,*Metall.Trans.,* **2**, 133 (Jan) (1971)
64. Fahr,D.,*Metall.Trans.,* **2**,1883 (Jul) (1971)
65. barclay , W.F.,*American Soc.Test.Metals-Spec.Tech.Pub.,* **369**, 26 (1965)
66. Hall,J.A.,Zackay,V.F. and Parker,E.R.,*Trans.ASM,* **62**, 965 (1969)
67. Kelly,P.M. and Nutting,J.,*J.Iron & Steel Inst.,* **184**, 199 (1961)
68. Mullner,P.,Solenthaler,C.,Uggowitzer,P. and Speidel,M.O.,*Pre-print of Proc.Intern.Conf.Fundamental Aspects Dislocation Interactions, LEDS III,* Ascona (Sep) (1992)
69. Fawley,R.,Quader,M.A. and Dodd,R.A.,*Trans.Met.Soc.AIME,* **242**, 771 (1968)
70. Singh,J.,*J.Mater.Sci.,* **20**, 3157 (1985)
71. Krivobok,V.N. and Lincoln,R.A., *Trans.Amer.Soc.Metals, Austenitic Stainless Steels*, 58 (1937)
72. Dastur,Y.N. and Leslie,W.C.,*Metall.Trans.,* **12A**, 749 (1981)
73. Zuidema,B.K.,Subramanyam,D.K. and Leslie,W.C.,*Metall.Trans.,* **18A**, 1629 (1987)
74. Rama Rao,P. and Kutumbarao,V.V.,*Int.Mat.Rev.,* **34(2)**, 69 (1989)
75. Jackson,R, *The 9th Biennial Congress of the International Deep Drawing Research Group, ASM,* Ann Arbor, USA, 264, (Oct)(1975)
76. Jahn,M.T.,Fan,C.M. and Wan,C.M., *J.Mat.Sci.,* **21**, 2866 (1986)
77. Bowkett,M.W.,Keown,S.R. and Harries,D.R.,*Metal Sci.,* **16**, 499 (Nov)(1982)
78. Bampton,C.C.,Jones,I.P.and Loretta,M.H.,*Acta Metall.,* **26**, 39, (1978)
79. Hirsch,P.B.,Howie,A.,Nicholson,R.B. , Pashley,D.W. and Whelan,M.J.,*Electron Microscopy of Thin Crystals,Butterworths,London,* 312 (1965)
80. Sandvik,B.P.J. and Wayman,C.M., *Metall.Trans,* **14A**, 809 (May) (1983)
81. Livitsanos,C.P. and Thomson,P.F.,*J.Mater.Sci.,* **12**, 2209 (1977)
82. Kumar,A. and Singhal,L.K.,*Metall.Trans.,* **19A**, 1021 (Apr) (1988)
83. Ayres,R.A.,*Metall.Trans.,* **16A**, 37 (Jan) (1985)
84. Jatczak,C.F.,Larson,J.A. and Shin,S.W.,*"Retained Austenite and its Measurement by X-ray Diffraction",* Information ManualSP-453 prepared by X-Ray Division of SAE

Fatigue Design and Evaluation Committee, Society of Automotive Engineers,Inc. Warrendale, 9 (1980)

85. DICKSON,M.J.,*J.Applied Crystallography*, **2**, 176 (1969)
86. SCHAEFFLER, A., *Metal Progress Data Sheet*, **Nov**, 680B, (1949)
87. PICKERING,F.B.,*High Nitrogen Steels,The Institute of Metals, eds* J.Foct and A.Hendry, Lille, France, 10 (1989)
88. TJONG,S.C.,HUNG,C.C. AND HO,N.J.,*J.Mat.Sci.,* **24**, 1257 (1989)
89. JENKINS,R. AND DE VRIES, J.L, *X-Ray Powder Diffractometry*, Phillips Gloeilampenfabrieken, Holland